Hierarchically Porous Silica, Carbon and Metal Oxide Monoliths – Synthesis and Characterization

Jan-Henrik Smått

Department of Physical Chemistry
Faculty of Mathematics and Natural Sciences
Åbo Akademi University
Turku, Finland
2006

From:
Department of Physical Chemistry
Åbo Akademi University,
Åbo, Finland

and

Graduate School of Materials Research
Åbo, Finland

Supervised by:
Prof. Jarl B. Rosenholm
Department of Physical Chemistry
Åbo Akademi University,
Åbo, Finland

Advised/co-supervised by:
Dr. Mika Lindén
Department of Physical Chemistry
Åbo Akademi University,
Åbo, Finland

Reviewed by:
Prof. Nicola Hüsing
Inorganic Chemistry I
University of Ulm
Germany

Dr. Anne Galarneau
Laboratoire de Matériaux Catalytiques et Catalyse en Chimie Organique
Ecole Nationale Supérieure de Chimie de Montpellier
France

Opponent:
Prof. Nicola Hüsing
Inorganic Chemistry I
University of Ulm
Germany

ISBN 952-12-1727-8

Åbo Akademis tryckeri – Åbo, Finland 2006

Dedicated to the memory of Mats Smått

Table of Contents

Abstract

Silica monoliths exhibiting a three-modal, hierarchical pore structure have successfully been prepared via sol-gel processing. Monolithic bodies with interconnected macropores in the μm range are a result of phase separation and gelation kinetics both being controlled by the addition of a hydrogen bonding polymer. The textural mesopores in the 10–20 nm range originate from voids between silica particles. Furthermore, the particles exhibit internal mesoporosity with pore diameters in the 2–4 nm range as a result of supramolecular templating by a cationic surfactant.

These silica monoliths have been used as hard templates to prepare nanocast carbon monoliths exhibiting a three or four-modal porosity by one-step impregnation of furfuryl alcohol as carbon precursor. The combined volume and surface templating, together with controlled synthesis of the starting silica monoliths used as the scaffold, enables a flexible means to simultaneously control the pore size on several length scales. The carbon monoliths are positive replicas of the micrometer length scale, while they are negative replicas on the nanometer scale.

In a similar fashion it is possible to prepare cobalt oxide replicas with a bimodal porosity. This approach has to the best of our knowledge never been reported previously. Furthermore, it is shown that the method can be generalized to encompass other metal oxides as well. These include tin and manganese oxides, which are difficult to prepare by direct synthesis.

The different modes of porosity are arranged in a hierarchical structure-within-structure fashion. This arrangement is optimal for materials requiring a high surface area in combination with a low pressure drop, such as catalysts, HPLC columns, and pressure sensors. The nanocasting route makes it possible to tailor the pore structure depending on the requirements for different applications.

List of Publications

The thesis is based on the following publications that are referred to in the text by their corresponding Roman numerals I–VII.

I. **Versatile Double-Templating Synthesis Route to Silica Monoliths Exhibiting a Multimodal Hierarchical Porosity**
Jan-Henrik Smått, Stephan Schunk and Mika Lindén, *Chemistry of Materials*, 15 (2003) 2354-2361.

II. **Chemical Removal of Organic Polymers from Highly Porous Sol-Gel-Derived Silica Monoliths**
Chia-Min Yang, Jan-Henrik Smått, Bodo Zibrowius and Mika Lindén, *New Journal of Chemistry*, 28 (2004) 1520-1525.

III. **Combined Surface and Volume Templating of Highly Porous Nanocast Carbon Monoliths**
An-Hui Lu, Jan-Henrik Smått and Mika Lindén, *Advanced Functional Materials*, 15 (2005) 865-871.

IV. **Carbon Monoliths Possessing a Hierarchical, Fully Interconnected Porosity**
Akira Taguchi, Jan-Henrik Smått and Mika Lindén, *Advanced Materials*, 15 (2003) 1209-1211.

V. **Easy and Flexible Preparation of Nanocasted Carbon Monoliths Exhibiting a Multimodal Hierarchical Porosity**
An-Hui Lu, Jan-Henrik Smått, Stefan Backlund and Mika Lindén, *Microporous and Mesoporous Materials*, 72 (2004) 59-65.

VI. **Hierarchically Porous Nanocrystalline Cobalt Oxide Monoliths through Nanocasting**
Jan-Henrik Smått, Bernd Spliethoff, Jarl B. Rosenholm and Mika Lindén, *Chemical Communications,* 19 (2004) 2188-2189.

VII. **Hierarchically Porous Metal Oxide Monoliths Prepared by the Nanocasting Route**
Jan-Henrik Smått, Claudia Weidenthaler, Jarl B. Rosenholm and Mika Lindén, *Chemistry of Materials*, 18 (2006), 1443-1450.

Supporting papers

Spherical Slica Agglomerates Possessing Hierarchical Porosity Prepared by Spray Drying of MCM-41 and MCM-48 Nanospheres
Anna Lind, Cedric du Fresne von Hohenesche, Jan-Henrik Smått, Mika Lindén and Klaus K. Unger, *Microporous and Mesoporous Materials*, 66 (2003) 219-227.

Synthesis of Carbon Monoliths with a Multi-Modal Pore System by a One Step Impregnation Technique
An-Hui Lu, Jan-Henrik Smått, Mika Lindén and Ferdi Schüth, *New Carbon Materials*, 18 (2003) 265-269.

Template-Free Sol-Gel Synthesis of Hierarchically Macro- and Mesoporous Monolithic TiO_2
Stefan Backlund, Jan-Henrik Smått, Jarl B. Rosenholm and Mika Lindén, *Journal of Dispersion Science and Technology,* in press.

Contribution of the Author

The author is responsible for all the experimental work in this thesis with the following exceptions:

The SEM pictures in paper I were recorded by Mr. Clifford Ekholm, in papers II–VI by Mr. Hans Bongard, and in paper VII by Dr. Sami Areva and MSc. Mikael Järn.

The TEM measurements in papers I, III, and V–VII were conducted by Mr. Bernd Spliethoff and in paper IV by Mr. Axel Dreier.

The mercury porosimetry measurements in papers II, III, and V were carried out by MSc. Stefan Backlund.

The ^{29}Si NMR measurements in paper II were conducted by Dr. Bodo Zibrowius.

The XRD measurements and particle size determinations using the Scherrer equation in paper VII were performed by Dr. Claudia Weidenthaler.

Additional technical assistance in paper I by MSc. Stefan Backlund.

The experimental work in paper II was carried out in collaboration with Dr. Chia-Min Yang.

The experimental work in papers III and V was carried out in collaboration with Dr. An-Hui Lu.

The preparation of the carbon replicas and the nitrogen physisorption measurements in paper IV were performed by Dr. Akira Taguchi.

List of Abbreviations and Symbols

BET	Brunauer-Emmett-Teller theory for surface area determination
BJH	Barrett-Joyner-Halenda method for deriving pore sizes
cmc	Critical micelle concentration
CMK	Carbon mesostructure from Korea Advanced Institute of Science and Technology
CTAB	Cetyltrimethylammonium bromide
CVD	Chemical vapor deposition
d, D	Pore diameter and particle diameter
DFT	Density functional theory
EDS	Energy dispersive spectroscopy
FA	Furfuryl alcohol
FSM	Folded sheet materials
FT-IR	Fourier transform infrared spectroscopy
IEP	Isoelectric point
MAS NMR	Magic angle spinning nuclear magnetic resonance
MCM	Mobil Composition of Matter
ODMCS	Octadecyldimethylchlorosilane
P/P_0	Relative pressure
PEG	Poly(ethylene glycol)
PEO	Poly(ethylene oxide)
PZC	Point of zero charge
r	H_2O/Si molar ratio
SBA	Santa Barbara Amorphous
SEM	Scanning electron microscopy
TEM	Transmission electron microscope
TEOS	Tetraetoxysilane
TG/DTA	Thermo-gravimetric/differential thermal analysis
TMB	1,3,5−trimethylbenzene
TMCS	Trimethylchlorosilane
TMOS	Tetrametoxysilane
XRD	X-ray diffraction

Abstract

Silica monoliths exhibiting a three-modal, hierarchical pore structure have successfully been prepared via sol-gel processing. Monolithic bodies with interconnected macropores in the µm range are a result of phase separation and gelation kinetics both being controlled by the addition of a hydrogen bonding polymer. The textural mesopores in the 10–20 nm range originate from voids between silica particles. Furthermore, the particles exhibit internal mesoporosity with pore diameters in the 2–4 nm range as a result of supramolecular templating by a cationic surfactant.

These silica monoliths have been used as hard templates to prepare nanocast carbon monoliths exhibiting a three or four-modal porosity by one-step impregnation of furfuryl alcohol as carbon precursor. The combined volume and surface templating, together with controlled synthesis of the starting silica monoliths used as the scaffold, enables a flexible means to simultaneously control the pore size on several length scales. The carbon monoliths are positive replicas of the micrometer length scale, while they are negative replicas on the nanometer scale.

In a similar fashion it is possible to prepare cobalt oxide replicas with a bimodal porosity. This approach has to the best of our knowledge never been reported previously. Furthermore, it is shown that the method can be generalized to encompass other metal oxides as well. These include tin and manganese oxides, which are difficult to prepare by direct synthesis.

The different modes of porosity are arranged in a hierarchical structure-within-structure fashion. This arrangement is optimal for materials requiring a high surface area in combination with a low pressure drop, such as catalysts, HPLC columns, and pressure sensors. The nanocasting route makes it possible to tailor the pore structure depending on the requirements for different applications.

List of Publications

The thesis is based on the following publications that are referred to in the text by their corresponding Roman numerals I–VII.

I. **Versatile Double-Templating Synthesis Route to Silica Monoliths Exhibiting a Multimodal Hierarchical Porosity**
Jan-Henrik Smått, Stephan Schunk and Mika Lindén, *Chemistry of Materials*, 15 (2003) 2354-2361.

II. **Chemical Removal of Organic Polymers from Highly Porous Sol-Gel-Derived Silica Monoliths**
Chia-Min Yang, Jan-Henrik Smått, Bodo Zibrowius and Mika Lindén, *New Journal of Chemistry*, 28 (2004) 1520-1525.

III. **Combined Surface and Volume Templating of Highly Porous Nanocast Carbon Monoliths**
An-Hui Lu, Jan-Henrik Smått and Mika Lindén, *Advanced Functional Materials*, 15 (2005) 865-871.

IV. **Carbon Monoliths Possessing a Hierarchical, Fully Interconnected Porosity**
Akira Taguchi, Jan-Henrik Smått and Mika Lindén, *Advanced Materials*, 15 (2003) 1209-1211.

V. **Easy and Flexible Preparation of Nanocasted Carbon Monoliths Exhibiting a Multimodal Hierarchical Porosity**
An-Hui Lu, Jan-Henrik Smått, Stefan Backlund and Mika Lindén, *Microporous and Mesoporous Materials*, 72 (2004) 59-65.

VI. **Hierarchically Porous Nanocrystalline Cobalt Oxide Monoliths through Nanocasting**
Jan-Henrik Smått, Bernd Spliethoff, Jarl B. Rosenholm and Mika Lindén, *Chemical Communications*, 19 (2004) 2188-2189.

VII. **Hierarchically Porous Metal Oxide Monoliths Prepared by the Nanocasting Route**
Jan-Henrik Smått, Claudia Weidenthaler, Jarl B. Rosenholm and Mika Lindén, *Chemistry of Materials*, 18 (2006), 1443-1450.

Supporting papers

Spherical Slica Agglomerates Possessing Hierarchical Porosity Prepared by Spray Drying of MCM-41 and MCM-48 Nanospheres
Anna Lind, Cedric du Fresne von Hohenesche, Jan-Henrik Smått, Mika Lindén and Klaus K. Unger, *Microporous and Mesoporous Materials*, 66 (2003) 219-227.

Synthesis of Carbon Monoliths with a Multi-Modal Pore System by a One Step Impregnation Technique
An-Hui Lu, Jan-Henrik Smått, Mika Lindén and Ferdi Schüth, *New Carbon Materials*, 18 (2003) 265-269.

Template-Free Sol-Gel Synthesis of Hierarchically Macro- and Mesoporous Monolithic TiO_2
Stefan Backlund, Jan-Henrik Smått, Jarl B. Rosenholm and Mika Lindén, *Journal of Dispersion Science and Technology*, in press.

Contribution of the Author

The author is responsible for all the experimental work in this thesis with the following exceptions:

The SEM pictures in paper I were recorded by Mr. Clifford Ekholm, in papers II–VI by Mr. Hans Bongard, and in paper VII by Dr. Sami Areva and MSc. Mikael Järn.

The TEM measurements in papers I, III, and V–VII were conducted by Mr. Bernd Spliethoff and in paper IV by Mr. Axel Dreier.

The mercury porosimetry measurements in papers II, III, and V were carried out by MSc. Stefan Backlund.

The ^{29}Si NMR measurements in paper II were conducted by Dr. Bodo Zibrowius.

The XRD measurements and particle size determinations using the Scherrer equation in paper VII were performed by Dr. Claudia Weidenthaler.

Additional technical assistance in paper I by MSc. Stefan Backlund.

The experimental work in paper II was carried out in collaboration with Dr. Chia-Min Yang.

The experimental work in papers III and V was carried out in collaboration with Dr. An-Hui Lu.

The preparation of the carbon replicas and the nitrogen physisorption measurements in paper IV were performed by Dr. Akira Taguchi.

List of Abbreviations and Symbols

BET	Brunauer-Emmett-Teller theory for surface area determination
BJH	Barrett-Joyner-Halenda method for deriving pore sizes
cmc	Critical micelle concentration
CMK	Carbon mesostructure from Korea Advanced Institute of Science and Technology
CTAB	Cetyltrimethylammonium bromide
CVD	Chemical vapor deposition
d, D	Pore diameter and particle diameter
DFT	Density functional theory
EDS	Energy dispersive spectroscopy
FA	Furfuryl alcohol
FSM	Folded sheet materials
FT-IR	Fourier transform infrared spectroscopy
IEP	Isoelectric point
MAS NMR	Magic angle spinning nuclear magnetic resonance
MCM	Mobil Composition of Matter
ODMCS	Octadecyldimethylchlorosilane
P/P_0	Relative pressure
PEG	Poly(ethylene glycol)
PEO	Poly(ethylene oxide)
PZC	Point of zero charge
r	H_2O/Si molar ratio
SBA	Santa Barbara Amorphous
SEM	Scanning electron microscopy
TEM	Transmission electron microscope
TEOS	Tetraetoxysilane
TG/DTA	Thermo-gravimetric/differential thermal analysis
TMB	1,3,5–trimethylbenzene
TMCS	Trimethylchlorosilane
TMOS	Tetrametoxysilane
XRD	X-ray diffraction

1. Introduction and Outline

The sol-gel processing technique has been widely used to prepare a variety of inorganic nanomaterials, including powders, fibers, thin films, and monoliths, starting from molecular building blocks.[1] However, since the discovery of the M41S family of silica materials by the Mobil Oil group[2,3] and the folded sheet materials (FSM) by the group of Kuroda[4] in the early 1990's, the majority of the work in this field has been focused on ordered mesoporous materials (2 nm < pore diameter: d < 50 nm). Just to give an example, in the "Web of Science" database of scientific papers[5] a search for the word "mesoporous" resulted in 9000 hits, while "MCM–41" (one of the materials in the M41S group) resulted in over 4000 hits. By using surfactants as supramolecular templates in a previously well described sol-gel synthesis, the Mobil Oil group succeeded in preparing silica materials with well arranged mesopores.[2,3] This breakthrough opened up new application possibilities that the already known microporous zeolites[6,7] could not offer (d < 2 nm). For instance, the mesoporous materials enabled the introduction of large guest molecules inside the pores. Moreover, not long after this discovery the method could be expanded to oxides other than silica. However, these materials usually had a slightly less ordered structure and problems occurred with the removal of the template. The preparation of ordered mesoporous non-siliceous oxides has recently been reviewed by F. Schüth.[8] As required in certain applications some of these materials have superior chemical and/or physical properties in comparison to the silica materials, for instance better chemical stability or electrical properties. Another processing strategy that has recently received a lot of attention is the nanocasting technique. Mesoporous silica materials have been used as hard templates in the preparation of mesoporous carbon[9,10] and non-siliceous metal oxides,[11–14] which are complicated to prepare through direct synthesis. Moreover, the nanocast carbon replicas can furthermore be used as templates in a subsequent nanocasting process to prepare metal oxide replicas.[15–18] The silica or carbon material is impregnated with precursor solutions, which are subsequently polymerized and heat treated at elevated temperatures to obtain rigid silica/carbon or silica/metal oxide composites. Finally, the silica portion can be leached out either in alkali metal hydroxide or hydrofluoric acid solutions. The carbon and metal oxide materials are negative replicas of the starting silica on the nanometer scale, which

means that the pores in the template become pore walls in the replica structure and vice versa. Most of the mesoporous materials prepared today are powders. However, in many applications other morphologies, such as thin films, fibers or monoliths, are required. Furthermore, materials with porosities arranged in a hierarchical structure-within-structure fashion have lately attracted a lot of interest, due to their high application potential for instance in the fields of catalysis[19], separation,[20–22] and sensor technology.[23] The advantage of this type of materials is that the large macropores combined with the mesopore structure give the monoliths large transport channels accompanied by a high active surface area. Good examples are the hierarchically macroporous/mesoporous silica monoliths synthesized using a sol-gel method described by Nakanishi *et al.*[24] During the preparation of silica gels it is possible to induce phase separation that takes place at the same instant as the sol-gel transition, which can be done by adding a hydrogen bonding polymer to the sol. After removing the liquid phase a macroporous body is obtained (d > 50 nm). Additional textural mesoporosity from voids between silica particles are also present in the monoliths, which give the material a high specific surface area. However, with a few exceptions[24,25] it has proven to be difficult to generalize the technique to other oxides mainly due to the poor control of the rapid hydrolysis and condensation reactions. In our work we have succeeded to combine two of these different approaches, namely to use the hierarchically porous silica monoliths as molds in the nanocasting process to prepare macroporous/mesoporous carbon and non-siliceous metal oxide monoliths.

The outline of the Doctoral thesis is to first review the chemistry behind sol-gel processing and to focus on the direct synthesis of silica monoliths, which later on can be used in nanocasting process. The "Nanocasting" section will highlight recent developments in the field as well as limitations of the technique. The chapter will also discuss the polymerization reactions and other parameters needed to understand the preparation of the carbon and metal oxide materials. In the "Experimental" part the synthesis methods are generally described together with the exact synthesis parameters for each sample. Moreover, the most central characterization techniques are described in more detail. The "Results" section can roughly be divided into two parts: *Direct synthesis* and *nanocasting*. The first two papers (I–II) deal with the direct synthesis of silica monoliths with either bimodal or trimodal pore structures. The first synthesis route pays attention to the structure directing mechanisms, while

the second is more focused on the template removal and surface structure in the final product. In papers III–V, the nanocasting process from the previously described silica monoliths to carbon replicas is described. Various replica structures can be obtained by altering the synthesis parameters, such as the starting silica monoliths, the concentration of the carbon source and the choice of catalyst. In the last two publications (papers VI–VII) the use of silica monoliths to prepare metal oxides other than silica by a similar technique as for the carbon replicas has been described. In this case, other factors such as the drying and decomposition temperatures also play important roles.

2. Sol-Gel Chemistry of Silicate Species

Sol-gel chemistry is a commonly used method for preparing materials with organized structures on the nanometer scale, i.e. nanomaterials.[1,26] The sol-gel process can be carried out at room temperature and there are a wide range of industrial applications for the materials produced. Optical coatings or fibers, fiber glass, nuclear fuels, and chromatographic columns are just a few examples of typical sol-gel derived materials. Starting from stable sols (colloidal suspensions) inorganic fibers, thin films, powders, and bulk materials (monoliths) containing homogeneous pore structures can easily be prepared. A monolith is defined as a three-dimensional object where the smallest dimension is larger than a few millimeters. Both organic (metal alkoxides) and inorganic (salts or particulate) precursor molecules can be used as building blocks in the sol-gel process. Since silica (SiO_2) is the most simple and most frequently used sol-gel system, we will focus on the sol-gel processing of silicate species. Unlike the transition metals, silicon has a higher electronegativity and has not the possibility to exhibit several coordination states, which results in a lower reactivity. Silica gels are most often synthesized by hydrolyzing monomeric, tetrafunctional alkoxide precursors by addition of a mineral acid or base as a catalyst. The sol-gel process can generally be described by three equilibrium reactions (where R is an alkyl group):

$$\equiv Si - OR + H_2O \underset{\text{esterification}}{\overset{\text{hydrolysis}}{\rightleftarrows}} \equiv Si - OH + ROH \qquad (2.1.)$$

$$\equiv Si - OR + HO - Si \equiv \underset{\text{alcoholysis}}{\overset{\text{alcohol condensation}}{\rightleftarrows}} \equiv Si - O - Si \equiv + ROH \qquad (2.2.)$$

$$\equiv Si - OH + HO - Si \equiv \underset{\text{hydrolysis}}{\overset{\text{water condensation}}{\rightleftarrows}} \equiv Si - O - Si \equiv + H_2O \qquad (2.3.)$$

The hydrolysis reaction (2.1.) replaces alkoxide groups (OR) with hydroxyl groups (OH). The subsequent condensation reactions produce siloxane bonds (Si–O–Si) with alcohol (2.2.) and water (2.3.) as by-products. Under standard synthesis conditions, the condensation reactions start before hydrolysis is complete. Because water and alkoxysilanes are immiscible, a mutual solvent such as alcohol is normally used as a homogenizing agent. However, gels can be prepared from silicon alkoxide-water

mixtures without added co-solvent, since the amount of alcohol produced in the hydrolysis reaction is sufficient to homogenize the initially phase separated system.[27] It should also be highlighted that alcohol is not merely a solvent; it can also participate in the reverse reactions: the esterification (2.1.) and alcoholysis (2.2.) reactions. The relative kinetics of the three equilibrium reactions are determined by several different parameters, including the type of precursor, pH of the sol, H_2O/Si molar ratio (*r* value), temperature, co-solvents, and the solubility of silica. All variations observed in the morphology of the final product can be ascribed to these reactions.

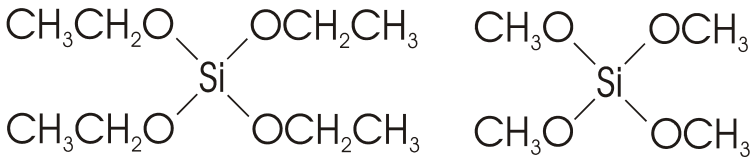

Figure 2.1. Molecular diagrams of TEOS and TMOS.

2.1. Morphology Control

Tetraetoxysilane (TEOS) and tetrametoxysilane (TMOS) are the two most common tetraalkoxysilanes used in sol-gel processing (Figure 2.1.). Besides TEOS and TMOS, more complicated types of precursor molecules can be used as well. As a cause of steric (spatial) effects, any increase in the size of the alkoxy group will give rise to a retardation of the hydrolysis rate,[28] which means that hydrolysis of TMOS will occur faster than hydrolysis of TEOS. The steric effect on hydrolysis is most notable for branched alkoxy groups. The inductive effects are important during the hydrolysis reaction, since hydrolysis (substitution of –OH for –OR) and condensation (substitution of –OSi for –OR or –OH) both decreases the electron density on silicon, which increase the stability on negatively charged transition states. This means that the hydrolysis rate will decrease with each subsequent hydrolysis and condensation step under acidic conditions, but increase under basic conditions due to the increased electron-withdrawing capabilities of –OH compared to –OR groups.

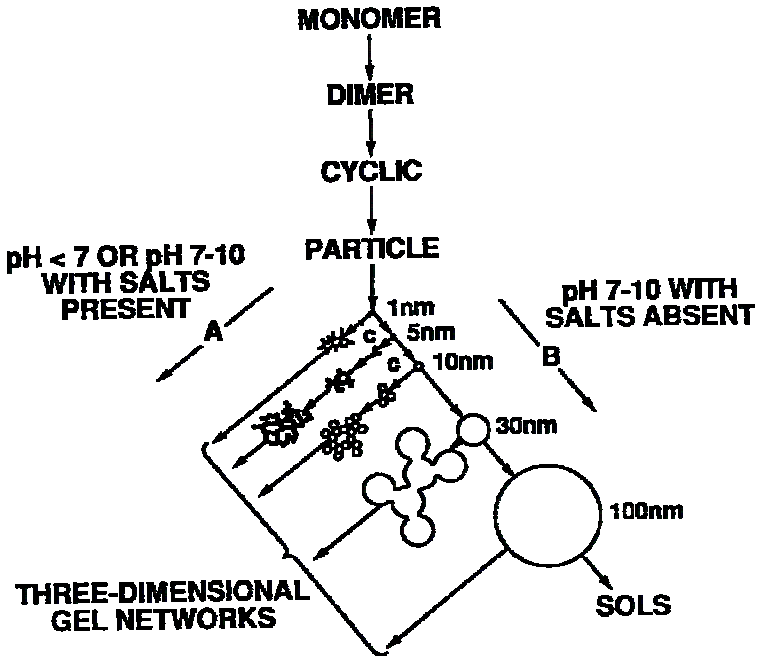

Figure 2.2. Polymerization behavior of aqueous silica. In basic solutions (B) particles grow in size with decrease in number. In acidic solutions or in the presence of flocculating salts (A), particles aggregate into three-dimensional networks and form gels.

Polymerization through condensation of adjacent $Si(OH)_4$ molecules forms coherent oligomers that by time increase in size. According to Iler, the polymerization occurs in three different stages: 1. Polymerization of monomers to form particles, 2. Growth of particles through dissolution/re-precipitation reactions, and 3. Linkage of particles first into branched chains, following by networks that extend throughout the liquid medium and finally thickening to a gel. After the initial step (1), either spherical particles with increasing diameter (2) or aggregates with an increasing number of particles (3) are formed. By altering the synthesis conditions it is possible to control which of the two pathways the polymerization will take. However, both particle growth and aggregation into networks can occur simultaneously. The polymerization of $Si(OH)_4$ from monomers to gels or powders is visualized in Figure 2.2.

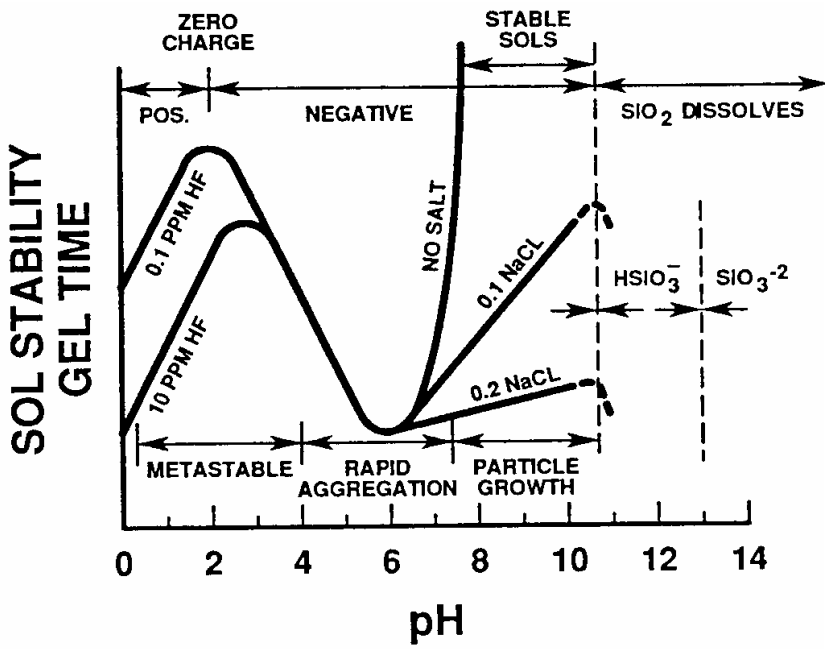

Figure 2.3. Effect of pH on gelation of silica. The stability of the sol is also schematized both with and without the addition of salt.[26]

Polymerization through condensation occurs by an ionic mechanism and is strongly affected by the pH of the sol. At pH > 2, the condensation rate is proportional to the OH^--concentration, while at pH < 2, it is proportional to the H^+-concentration. The minimum rate coincides at pH ~ 2 where both the *point of zero charge* (PZC, where the surface charge is zero) and the *isoelectric point* (IEP, where the electrical mobility of the silica particles is zero) appear. According to the DLVO theory (Derjaugin, Landau, Verwey, and Overbeek), colloidal particles should be least stable at the IEP. However, silica does not conform to the DLVO theory, because it is stabilized by a layer of adsorbed water molecules that prevents coagulation at the IEP. At moderate acidities (pH = 0–2), the solubility of silica is quite low. This means that ripening contributes very little to growth after the particles exceed 2 nm in diameter; instead, the particles aggregate into a gel network. The long gelation times at moderate pH conditions can be shortened by introducing stronger acids (pH < 0) or by adding fluoride ions to the solution. The time of gelation also decreases from pH = 2 to pH = 6 because the gelation is catalyzed by OH^- ions. At pH > 7 no aggregation to gel networks occurs, just particle growth. This phenomenon can be explained by the stabilizing negative charge the silicate particles receive from the OH^- ions after this

pH value. Because of the greater solubility of silica and the greater size dependence of solubility above pH = 7, growth of the primary particle continues by *Ostwald ripening* (dissolution of smaller particles and deposition of soluble silica on larger particles). By adding salt and effectively screening the charge, one can even cause weakly basic sols to gel. The primary building blocks are cyclic trimers and tetramers above pH = 12, where most of the silanols are deprotonated.[29] The effects of pH and salt addition in the colloidal silica-water system are summarized in Figure 2.3. A catalyst is employed to make the hydrolysis and condensation steps as rapid and complete as possible. Although mineral acids or ammonia are the most widely used catalysts in sol-gel processing, other known catalysts are acetic acid, KOH, KF, HF, amines and titanium alkoxides.

Regardless of the type of catalyst, the H_2O/Si molar ratio (r) is of decisive importance in the production of gels with different properties. According to equation 2.1., an increased value of r is expected to promote the hydrolysis reaction. A higher value of r also causes a more complete hydrolysis of the monomers before the condensation reactions start. Generally, the alcohol-producing condensation mechanism is favored with understoichiometric additions of water ($r << 2$), whereas the water-forming condensation is favored when $r \geq 2$.[30] Because water is produced as a by-product of the condensation reaction, an r value of 2 is theoretically sufficient for complete hydrolysis and condensation. However, not even in excess water ($r >> 2$), will the reaction go to completion. In the production of monoliths as well as thin films, a large H_2O/Si molar ratio (typically 10) and a pH value less than 0 or close to 6 is suitable. A low pH value together with a small r value ($r \sim 1$) is used to prepare a viscous, spinnable sol from which silica fibers can be drawn. Base-catalyzed synthesis with a large water to silicon ratio ($r = 20–50$) forms highly condensed, particulate sols which can be dried to a powder. Furthermore, co-solvents can also be added to control the gelation kinetics.

2.2. Gelation and Aging

When silica goes through hydrolysis and condensation the particles will aggregate into clusters. Further condensation makes the clusters grow larger until the clusters collide with each other. Links will form between the clusters, finally forming a single

giant cluster, reaching across the vessel that contains it. This giant spanning cluster is called a gel. The instant in time when gelation takes place is called the *time of gelation, t_{gel}*. At the moment the gel forms, many clusters will be present in the sol phase, entangled but not attached to the spanning cluster. After some time the small clusters will also become connected to the network and the stiffness will increase. This increase in viscosity can be used to determine the gel point. However, the reactions that lead to gelation do not stop at the gel point, since there are still oligomers in the solution that are free to diffuse and react. The fact that liquid is flowing through the gel means that gradual changes in the structure and the properties of the gel will appear. This process is called *aging of the gel*. Aging of gels is the strengthening, stiffening and shrinking of a newly formed gel network which results from the same reactions that led to the forming of the gel. Processes of dissolution and re-precipitation may coarsen the pore structure and separation may occur into mixtures of solid-liquid, liquid-liquid, or solid-solid phases. These changes have a profound effect on the subsequent processes of drying and sintering. The processes of change during aging after gelation are categorized as (1) polymerization, (2) coarsening, and (3) phase transformation. During polymerization new bonds are formed in the silica network by continuous condensation reactions. Studies based on ^{29}Si–NMR[31] and Raman spectroscopy[32,33] indicate that the number of Si–O–Si bonds increase up to several months after gelation. The rate of reaction is dependent on temperature and the concentration and pH of the solution. New bridging bonds stiffen and strengthen the network. *Syneresis* is a form of gel network shrinkage resulting in expulsion of liquid from the pores caused by condensation reactions. Because syneresis requires movement of liquid through the pores, the kinetics of shrinkage and the temperature dependence of the shrinkage rate depend on the mechanical properties and the permeability of the network.

The second type, *coarsening and ripening*, is an aging process of dissolution and re-precipitation (*Ostwald ripening*) driven by differences in solubility, *S*, between surfaces with different radii of curvature, *r*, according to equation 2.4.

$$S = S_0 \exp\left(\frac{2\gamma_{SL}V_m}{RTr}\right) \qquad (2.4.)$$

Here, S_0 is the solubility of a flat plate, γ_{SL} is the solid–liquid interfacial energy, V_m is the molar volume of the solid phase, R is the ideal gas constant, and T is the temperature.

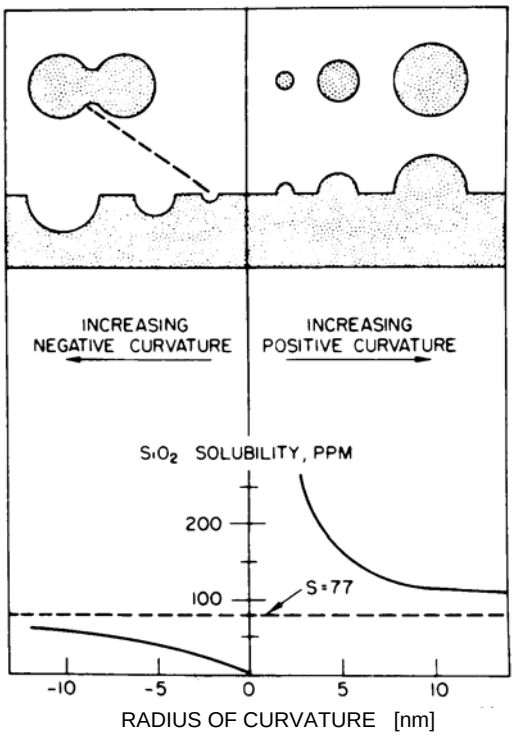

Figure 2.5. Solubility of silica with different curvatures.

As shown in Figure 2.5, precipitation takes place on surfaces with negative curvature, where solubility is low. The result of Ostwald ripening is to reduce the net curvature of the solid phase, meaning that small particles are dissolved and small pores are filled in so that the interfacial area decreases and the average pore size increases. Furthermore, it also results in that the growth of necks adds strength and stiffness to the network. The rate of coarsening is influenced by the factors that affect the solubility, such as temperature, pH, concentration, and type of solvent. Solvent exchange post-treatments can also be carried out to control the pore structure on the nanometer scale.[26,34,35]

Finally, several types of *phase transformations* can also occur during aging. *Micro-syneresis* is a process of phase separation in which the polymers cluster together creating regions of free liquid. The driving force is the greater affinity of the polymer for itself than for the pore liquid. The structural changes that occur during aging have

an important effect on the drying process. The capillary pressure that develops during drying is proportional to the interfacial area in the gel. Since coarsening reduces the interfacial area, the maximum pressure generated during drying is smaller. The stiffer and stronger the gel network becomes, the better it can withstand the capillary pressure. This means that aged gels shrink and crack less.

2.3. Drying

The process of drying of a porous material can be divided into three stages. In the beginning, the gel shrinks by an amount equal to the volume of liquid that evaporates with the remaining liquid vapor interface at the exterior surface of the gel. This first stage of drying is called the *constant rate period* (CRP) because the rate is independent of time. However, the drying rate may differ slightly depending on the texture of the surface. For alkoxide-derived gels the vapor pressure must be kept high to avoid rapid drying, since it can lead to cracking of the gel, due to capillary forces inside the pores. When the gel has become stiff and the tension in the liquid cannot overcome the stiffening of the network, the shrinkage stops. This is called the critical point, which marks the end of the CRP, where cracking is most likely to occur. Evaporation after the critical point is called the *first falling rate period* and creates unsaturated pores. The saturated body is translucent or transparent because of the similarity in refractive index of the liquid and solid. However, the lower index of air causes scattering of light, making the gels opaque. Further evaporation also drives the meniscus into the body, as described in Figure 2.6a. Even as air invades the pores, a continuous liquid film supports flow to the exterior, so evaporation continues to occur from the surface of the gel. In the first falling rate period, the rate of evaporation decreases and it is sensitive to the ambient temperature and the vapor pressure, since the temperature of the surface rises. As the meniscus recedes into the body, the liquid gets isolated in pockets inside the gel. At this stage, the *second falling rate period*, the liquid can only be removed by diffusion of its vapor, as visualized in Figure 2.6b. The temperature of the surface approaches the ambient temperature and the rate of evaporation becomes less sensitive to external conditions, such as temperature, humidity, and draft rate. Since the temperature is higher at the surface, there is a driving force for diffusion into the gel.

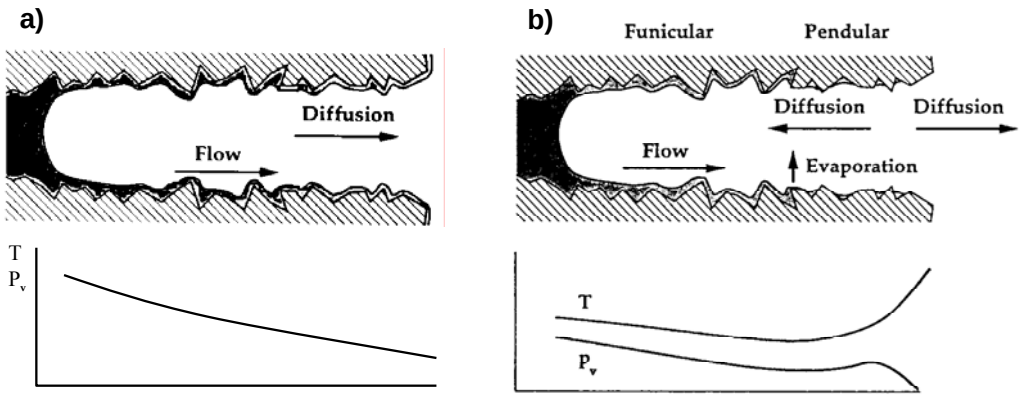

Figure 2.6. a) After the critical point, the liquid-vapor meniscus retreats into the pores of the body (the first falling rate period). b) Schematic illustration of the transport phenomena during the second falling rate period.

3. Direct Synthesis of Porous Silica Sol-Gel Materials

The previously discussed sol-gel techniques can be applied to prepare materials with porosities on different length scales. The International Union of Pure and Applied Chemistry (IUPAC) has recommended a specific nomenclature for porous materials based on pore diameter (d): microporous ($d < 2$ nm), mesoporous (2 nm $< d <$ 50 nm), and macroporous ($d >$ 50 nm).[36] Depending on the material, the pore sizes may vary from micropores to macropores, as can be seen in Figure 3.1.

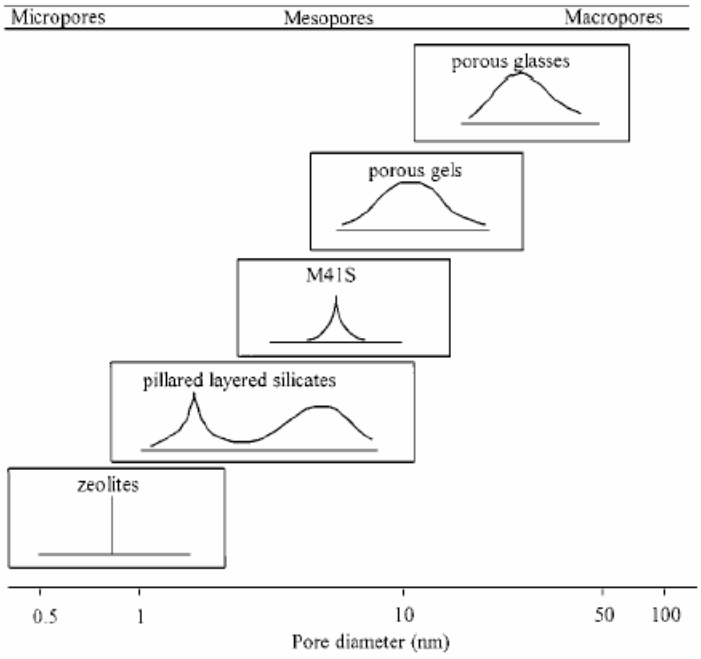

Figure 3.1. Definition of pore sizes, adapted from Behrens.[37]

Liquids and gases have been found to exhibit a characteristic transport behavior in each type of porous material, including: 1. viscous flow and diffusion in macroporous materials, 2. surface diffusion and capillary transport in mesoporous materials, and 3. activated transport in microporous materials.[38] Materials with two or more separated pore size regions arranged in the same material are said to have a hierarchical pore structure. This could for instance be combinations of micro- and mesopores, micro- and macropores, or meso- and macropores.

3.1. Methods to Control the Pore Structure

So far, there have been a great number of publications concerning sol-gel materials with pores arranged in a hierarchical fashion and the preparation methods varies over a wide range, from simple to complex. However, most of these synthesis strategies involve the addition of a *structure directing agent*, which is defined as a chemical that either chemically (thermodynamically) or physically (soft or hard templating) directs the molecular building blocks to form porous structures. In this chapter, the usage of a thermodynamic pathway combined with soft templating techniques to prepare macro/mesoporous silica monoliths will be discussed. A more thorough description of hard templating techniques (nanocasting) will be presented in Chapter 4. In the case of templating it is also necessary to remove the templates to obtain a porous structure, which can be done either by chemical or thermal means.

3.1.1. Phase Separation Induced Macroporosity

In a series of papers, Nakanishi *et al.* have described a concept of preparing silica monoliths containing both macropores and mesopores.[24,39–44] The concept is based on inducing a microscopic phase separation that takes place simultaneously as the sol-gel transition. Several different structure directing agents can be added to induce this phase separation, including formamide,[24,39] strongly or weakly hydrogen bonding polymers,[24,40–42] and surfactants.[43,44] The mechanism is believed to be a type of *spinodal decomposition* that induces a transition structure with a silica-rich phase and a solvent-rich phase. Moreover, this intermediate structure is locked in due to the "freezing" of the structure during the sol-gel transition. The relative kinetics of the competing processes is of great importance to the final product. The liquid phase is removed by evaporation to obtain the final macroporous structure. Similar approaches have been used to directly prepare macroporous polymer monoliths,[45] as well as macroporous titania (TiO_2) monoliths.[46–48] However, when preparing transition metal oxide materials the large shrinkage during the drying step is still a drawback. Furthermore, by using similar sols as used when preparing macroporous monoliths, macroporous thick films of SiO_2[49] and TiO_2[50] have been prepared via a sol-gel dip-

coating technique. Here, the evaporation of the solvent is an additional processing parameter.

The term spinodal decomposition is defined as a clustering reaction in a homogeneous, supersaturated solution (solid or liquid) which is unstable against infinitesimal fluctuations in density or composition.[51] The solution therefore separates spontaneously into two phases, starting with small fluctuations and proceeding with a decrease in the Gibbs energy without a nucleation barrier. This decrease of the free energy of mixing, ΔG, can be expressed by the Flory-Huggins formulation:[52–54]

$$\Delta G \propto RT\left[\left(\phi_1 / P_1\right)\ln\phi_1 + \left(\phi_2 / P_2\right)\ln\phi_2 + \chi_{12}\phi_1\phi_2\right] \tag{3.1}$$

Here, the ϕ_i's and P_i's denote the volume fraction and the degree of polymerization of each component (1 and 2), and χ_{12} is the interaction parameter. The former two terms in the bracket express the ideal entropic contribution while the last term defines the enthalpic contribution. Since the decrease in absolute values of the negative entropic terms makes the system unstable, it is evident that an increase of the degree of polymerization of either component makes the mixture less compatible. When the sign of ΔG changes from negative to positive a driving force of phase separation arises. This means that an initially single-phase solution containing a polymerizable component (like TEOS) becomes less stable with an increase of the molecular weight of the component and finally results in the separation into two different phases. The similar thing will also occur if the positive enthalpic contribution increases in the proceeding of the polymerization. A polycondensation reaction in a polar solvent, which alters the polarity of the polymer, for example silica oligomers attaching to an organic polymer, is a possible explanation for substantial changes in the enthalpic term observed during the polymerization.[24,45]

Another way to describe the phase separation system is visualized in Figure 3.2. Here, the starting composition and temperature is initially located in the single-phase region, but finally ends up in the two-phase region inside the binodal line. In contrast to physical cooling, which is the usual way of changing the compatibility of a mixture, the polymerization reaction can be regarded as the "chemical cooling" of the system. An increase in the number of chemical bonds is equivalent to an increase in the attractive interaction among constituents. There actually exists a clear similarity

between chemically and physically cooled binary mixtures, both having two-phase regions around the respective gel- and glass-transition temperatures.

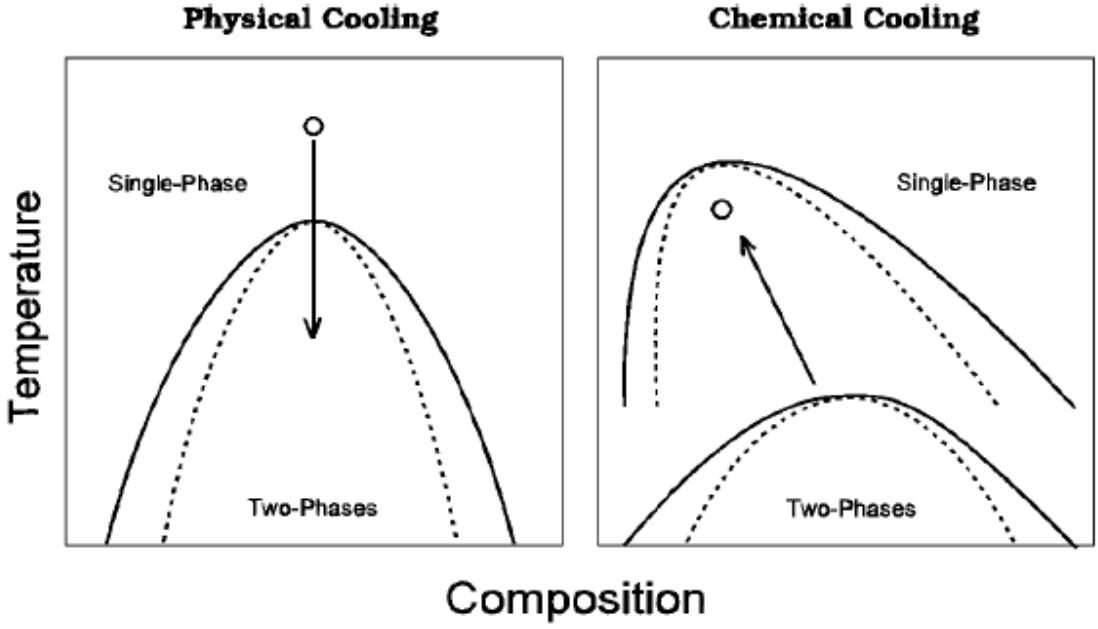

Figure 3.2. Comparison between physical and chemical cooling. The solid and broken lines respectively denote the binodal and spinodal lines, respectively.

In our system, the phase separation and the sol-gel transition take place simultaneously and are closely interlinked. For clarity, the two will be discussed separately. In the binary composition-temperature diagram in Figure 3.2, the two-phase region is surrounded by a binodal line where the first derivative of Gibbs free energy of the system with respect to the composition becomes zero. Between the binodal line and the spinodal line (where the second derivative becomes zero) exists a metastable region, while inside the spinodal line an unstable region is present. Depending on in which region the phase separation is initiated, two modes of phase separation have been observed. In the metastable region a nucleation-growth process takes place, while spinodal decomposition takes place in the unstable region inside the spinodal line. The spinodal decomposition starts with an infinitesimal composition fluctuation, marked by a characteristic wavelength with an amplitude that continuously grows which increases the separation between the phase domains. Subsequently, while the composition difference between the domains increases, the domain size also starts to increase (intermediate stage). Finally, the domains reach

respective equilibrium compositions while their sizes continue to increase (late stage) driven by the surface energy. From the morphological point of view, the intermediate and late stages are regarded as the coarsening stage where the domains grow in size, as shown in Figure 3.3. It is not possible to determine which of the two mechanisms has occurred by only characterizing the final product. However, in situ light scattering can be applied for this purpose.[24,45] The sol-gel transition stages were explained in detail in Chapter 2.1.

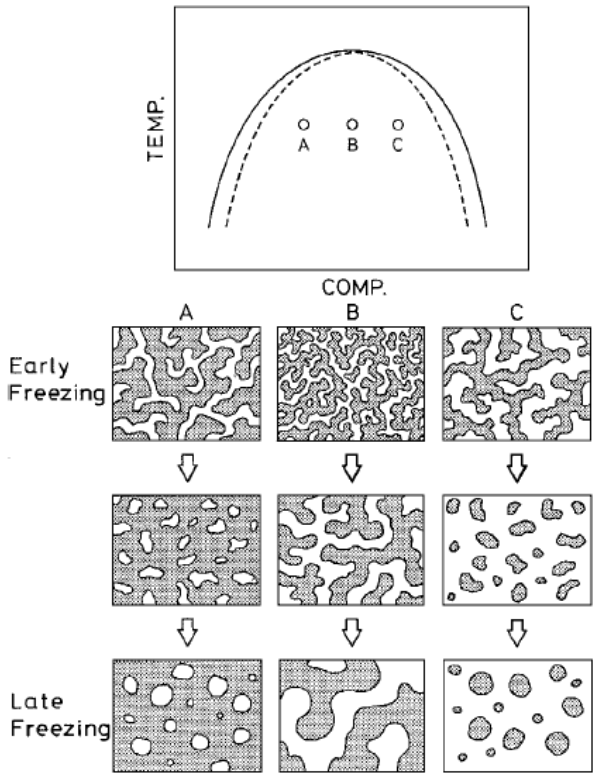

Figure 3.3. The onset and time evolution of coarsening of phase separating domains which occurs at various locations in the unstable region.

As mentioned earlier, the required phase separation between the silica phase and the liquid phase can be induced by either an entropic or an enthalpic mechanism. The difference between these depends on the hydrogen-bonding ability of the employed polymer.[24] If the polymer has relatively weak interactions with hydrolyzed silica oligomers, the phase separation takes place into a silica-solvent phase and a polymer-solvent phase (Figure 3.4a). The phase separation in this system is driven by the entropy loss due to the polymerization of silica and thus depends on the mutual molecular weight of the constituents.[40,41] In the case that the polymer has strong

interactions with silica (e.g. a hydrogen bond), one of the conjugate phases becomes rich in silica and polymer while in the other the solvent together with silica becomes the major constituents (Figure 3.4b). In this enthalpy driven system the phase separation is mainly induced by the increase in repulsive interactions between silica oligomers adsorbed by incorporated polymer and the solvent mixture. In order to induce the phase separation at the same time as the polymerization of hydrolyzed alkoxysilane, the hydrogen bonds between polymer molecules and silanols must not be too strong as to completely prevent the polycondesation reaction between the polymers. Polymers fulfilling this requirement include poly(ethylene oxide) (or PEO), poly(vinylpyrrolidone) and poly(acrylamide).[24,42]

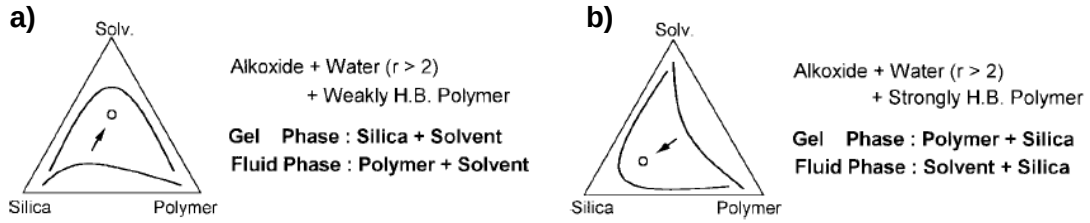

Figure 3.4. The phase behavior of a) entropic and b) enthalpic driven systems.

For the enthalpy driven systems, like the PEO system, there are several parameters that can be used to control the structural evolution of the macropores in the monoliths, including the molecular weight of the polymer, the synthesis temperature, the amount of polymer, and the solvent to Si ratio.[24] The phase separation tendency increases with the molecular weight of PEO, because the heat of solution of PEO into water also increases, or in other words it becomes less exothermic. Typically molecular weights above 10,000 g/mol are used to induce the phase separation. Furthermore, when increasing the reaction temperature, the system is affected in two ways; namely accelerating the gel formation and delaying the onset of phase separation. As a result of this, the domain size is decreased. The size range interconnected domains also contracts with an increase of temperature. By varying the PEO/Si ratio the domain size (gel skeleton + macropores) can be controlled. At low additions of PEO the phase separation tendency is the highest, which results in a late freezing of the structure (as seen in Figure 3.3.). Large domain sizes or even macroscopic phase separation can be observed here. However, when the PEO concentration is increased, the onset of phase separation is gradually delayed and smaller domains are observed (early freezing). A

great advantage of the PEO system compared to the weakly hydrogen bonding systems is that it is possible to adjust the ratio between the macropores and macropore walls (gel skeleton) almost independently of the domain size by altering the ratio between the two phases (Figure 3.3.). From low (A) to high (C) silica concentrations the resulting macropores structure changes from particle aggregates to isolated pores. In between (B) there exists a region where the two phases are about the same size, which leads to an interconnected (bicontinuous) pore structure.

Moreover, it is widely known that the preparation of monoliths under acidic conditions leads to a microporous structure.[55] These monoliths can further be modified in the aging step by Ostwald ripening processes in either strong acids or ammonia. The principle was more thoroughly explained in Chapter 2.2.

3.1.2. Surfactant Templated Mesopores

The discovery that surfactant assemblies can template the synthesis of highly ordered mesoporous silicates and produce a family of materials collectively known as M41S is one of the most significant recent developments in the chemistry of mesoporous silica.[2,3] Simultaneously with this breakthrough, the group of Kuroda succeeded in preparing materials with similar structures, so called folded sheet materials (FSM), by intercalation of kanemite (a sheet silicate) with cationic surfactants.

One of the most studied M41S materials, Mobil Composition of Matter–41 (MCM–41) contains regular arrangements of hexagonal pores in a honeycomb arrangement. However, by adjusting the synthesis parameters several other types of structures can be tailored as well. Amphiphilic organic molecules, also known as surfactants, may cooperatively organize into a variety of structures in aqueous solutions. Generally, an isotropic solution phase forms at low surfactant concentrations, while transitions into hexagonal, cubic and lamellar liquid crystal mesophases separated by the two corresponding two-phase regions may be observed with increasing surfactant concentration (Figure 3.5.). By carefully selecting the charge and geometry (the packing parameter) properties of the used surfactant, it is possible to influence the resulting structure of the silica material. When preparing MCM–41, typically a cationic alkyltrimethylammonium halide surfactant is used to create the 2-D hexagonal (*p6m*) pore structure. Nonetheless, MCM–41 may be

synthesized at low surfactant concentrations where only spherical micelles are present in binary surfactant-water solutions. This indicates that the presence of preformed rod-like micelles is not a prerequisite for the formation of MCM–41. Under alkaline conditions, which are normally used for MCM–41 synthesis, anionic silicate species, I^-, and cationic surfactant molecules, S^+, cooperatively organize to form S^+I^- interfaces between the silicate species and the surfactant. The strong adsorption of silica species to the micellar interface may be expected to favor a transition to rod like structures.[56] At yet higher surfactant concentrations transitions to cubic (*Ia*3*d*) or lamellar structures can be observed as well, denoted MCM–48 and MCM–50 by the Mobil Oil group, respectively (Figure 3.5.).[57]

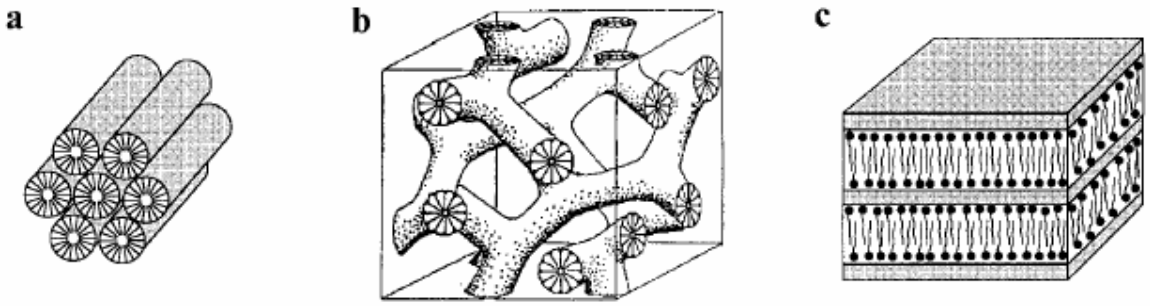

Figure 3.5. Three structure types observed for silica-surfactant mesophases: (a) hexagonal; (b) cubic bicontinuous, *Ia*3*d*; and (c) lamellar.[58]

In the pseudomorphic synthesis pathway, the MCM–41 and MCM–48 structures can also be induced into silica gel spheres by treating them in highly alkaline solutions in the presence of surfactants.[59,60] Due to the dissolution and re-precipitation of Si–O–Si bonds in this pH range, the silica gel grains transform into an ordered hexagonal structure with time. Thus, the technique can be used to prepare MCM–41 materials with controlled morphology. An exciting aspect of the M41S materials is that the pore size can be tailored in the range of 15–100 Å by choosing suitable synthesis conditions. A direct relationship in these materials exists between the alkyl chain length of the surfactant template molecule and the pore size of the final product.[3,61] Furthermore, solubilization of organic molecules, like 1,3,5–trimethylbenzene (TMB), inside the hydrophobic hydrocarbon moieties of the surfactant micelles can also be employed to swell the size of the pores.[62–65] The group of Stucky showed that

silica materials with hexagonal mesostructures may also be synthesized under extremely acidic conditions where the silicate species are positively charged.[63,66] The formation of a triple layer, $S^+X^-I^+$, where the halide anions (X^- = Cl^- or Br^-), in the electrical double layer around the micelles serve as charge mediators and coordinate electrostatically to the protonated silanols, is suggested to account for the formation of the mesophase. These materials are labeled Santa Barbara Amorphous−3 (SBA−3). Later on, the same group proved that also non-ionic surfactants (S^0) can be used to create ordered mesostructures.[67,68] The most important structures are made from triblock poly(ethylene oxide)-poly(propylene oxide)-poly(ethylene oxide) copolymers, including the large pore sized 2−D *p6mm* hexagonal structure of SBA−15 and the cubic *Im*3*m* cage-structure of SBA−16. The mechanism of formation is suggested to take place by a hydrogen bonding (S^0H^+)(X^-I^+) pathway in acidic media. An important dissimilarity from the previously discussed M41S materials is that the block copolymer synthesized materials are typically microporous as a result of the removal of poly(ethylene oxide) chains that have been infiltrated into the silica walls.

3.2. Template removal

In order to obtain a porous medium in the previously described systems, template removal is a necessary processing step.[69] The most common method to date is calcination (thermal decomposition), which is achieved by heating the silica/template composites at elevated temperatures resulting in the combustion of the organic template. However, during the heating of the samples other unfavorable reactions might occur as well, such as the removal of surface hydroxyl groups (important for further functionalization steps), further condensation, and shrinkage, to name a few. Moreover, calcination generates a high amount of organic residue (typically 45−55 wt % of the as-made MCM−41) and it is not a cost-effective method. To avoid these problems other template removal methods have been developed, including microwave digestion,[70] supercritical fluid extraction,[71] as well as plasma and ozone treatments.[72] One of the most prominent methods is to remove the organic molecules by solvent extraction techniques. The efficiency of the extraction depends in particular on the strength of the interaction between organic molecules and the framework. For

MCM–41 materials prepared using the $S^+X^-I^+$ or S^0I^0 pathways, the weak interactions between organic and inorganic phases make that surfactant molecules can be removed from the mesopores by a simple ethanol extraction.[66,73] The extracted surfactant molecules can be regenerated later. In contrast, this method cannot be applied to MCM–41 materials prepared in basic media, in which strong electrostatic interactions between surfactant micelles and the inorganic network exist. For Al–MCM–41 materials with low Al contents, treatments with alcoholic solutions of K^+, Na^+, or $NH4^+$ cations have been shown to partially extract template molecules.[74] A more harsh method to remove surfactants is to "chemically" leach out the surfactant templates. Yang *et al.* have developed a method to empty the micro/mesoporous pore system in SBA–15 step by step.[75,76] The mesoporous channels are first vacated by decomposition of the triblock copolymer template via ether cleavage with sulphuric acid. In a second step, the occluded EO chains in the pore walls, which are not accessible to the acid, can be thermally decomposed at ~ 200 °C to generate the microporosity. This method is advantageous for the design of advanced nanomaterials since it allows the surface of mesopores and micropores of SBA–15 to be modified with different functionalities.

4. Nanocasting

The use of the word nanocasting is sometimes quite confusing, because in some contexts it could also include the use of molecular templates as in the case of surfactant templates for preparing ordered mesopores discussed in the previous chapter. However, in that case the "replica" structure is not necessarily an exact negative copy of the soft, liquid-containing surfactant aggregates. In a similar fashion are the macropores in the silica monoliths formed by phase separated liquid, which can also be considered soft templating. On the contrary, when using a rigid scaffold, a so-called hard template, the replicated structure is a direct *negative* replica of the original structure. Thus, in the following, only techniques using rigid scaffolds as templates (or molds) will be regarded as nanocasting techniques. Porous or non-porous silica materials, carbon materials, and polymeric beads are just a few examples of materials which can be used as hard templates in nanocasting processes. The different steps in the nanocasting process are illustrated in Figure 4.1.

Similarly as in the classical bronze casting technique, which can be considered macroscopic casting, the porous (or non-porous) mold is impregnated (or covered) with the replica precursor, which could be a liquid containing polymerizable monomers or a colloidal suspension. A prerequisite to obtain a good replication of the original structure is that the template and the precursor molecules are mutually compatible, which is particularly important in the nanocasting process due to the large surface area to volume ratio in mesoporous materials.[77] Moreover, the precursor molecules or particles need to be small enough to be able to enter the porosities or the texture on the surface. Polymerization of the monomer solution is one way to "freeze" (or stiffen) the structure in the subsequent step. The polymerization can typically be initiated by the addition of a catalyst, by heating or by evaporation of the solvent, all depending on which precursor has been used. The polymerization reactions should be carefully controlled to obtain as precise replica structure as possible. A problem related to the capillary pressure inside the mesopores is that the evaporation of the solvent during drying might expel the precursor molecules from the pores. Further processing, like carbonization or crystallization, might still be needed to obtain a rigid scaffold that can withstand the final template removal step. During this heating step, it is important that the phase transitions do not alter the template in any way and one has

to keep in mind that the reactions taking place inside confined spaces are different from reactions in the bulk. In classical casting processes the mold can easily be removed either by mechanical or thermal means. In nanocasting processes, however, thermal combustion and chemical leaching are the most common methods used to eliminate the templates. A crucial requirement in both methods is that the desired replica structure should not be affected by the treatment. Furthermore, the pore structure of the template should be arranged in an interconnected 3–D network in order to obtain a replica with the same macroscopic morphology after the template has been removed.

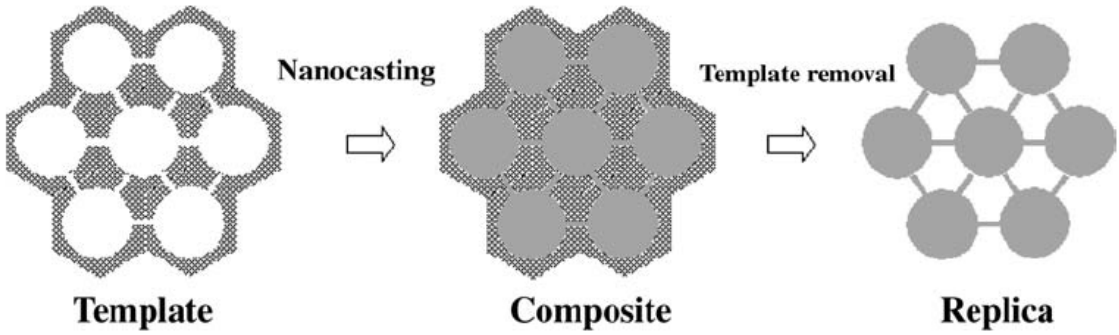

Figure 4.1. A schematic description of the nanocasting process.[78]

4.1. Preparation of Nanocast Carbon Materials

Since the first nanocasting process using mesoporous silica materials as hard templates, which was described by the group of R. Ryoo in 1999, various types of templates have been used in the preparation of carbon replica structures. However, the chemical composition of the templates has solely been limited to pure silica or aluminosilicates, which is understandable due to the wide variety of already existing mesoporous materials. Moreover, it is also possible to eliminate the silica and aluminosilicate part in the composite by selective leaching. The majority of the previously described ordered silica structures have successfully been replicated, including the cubic MCM–48[9,79,80] and hexagonal SBA–15[10,81] structures. These carbon materials are designated as CMK–1 (Carbon Mesostructure from Korea Advanced Institute of Science and Technology) and CMK–3, respectively. One requirement is that the pore channels should form an interconnected 3–D network in

order to avoid a collapse of the replica structure upon removal of the template, which is why it is impossible to obtain an ordered carbon structure when using the two-dimensionally hexagonal MCM−41 pore structure as template. The reason why the CMK−3 structure does not collapse when using the SBA−15 type silica as template is because of the hexagonal pore channels here are connected through micropores, which forms the essential 3−D interconnected pore network. Thus, the most efficient way to control the pore size and the pore geometry of the carbon replica is to vary the structure of the starting silica template. Different degrees of infiltration (loading) can also be utilized to obtain various replica structures.[82,83] When preparing the carbon material CMK−5 the walls of SBA−15 are only coated with carbon instead of completely filled as in the case of CMK−3, leading to *tube-like* structures instead of *rod-like* after the silica template has been removed, which is schematically illustrated in Figure 4.2.

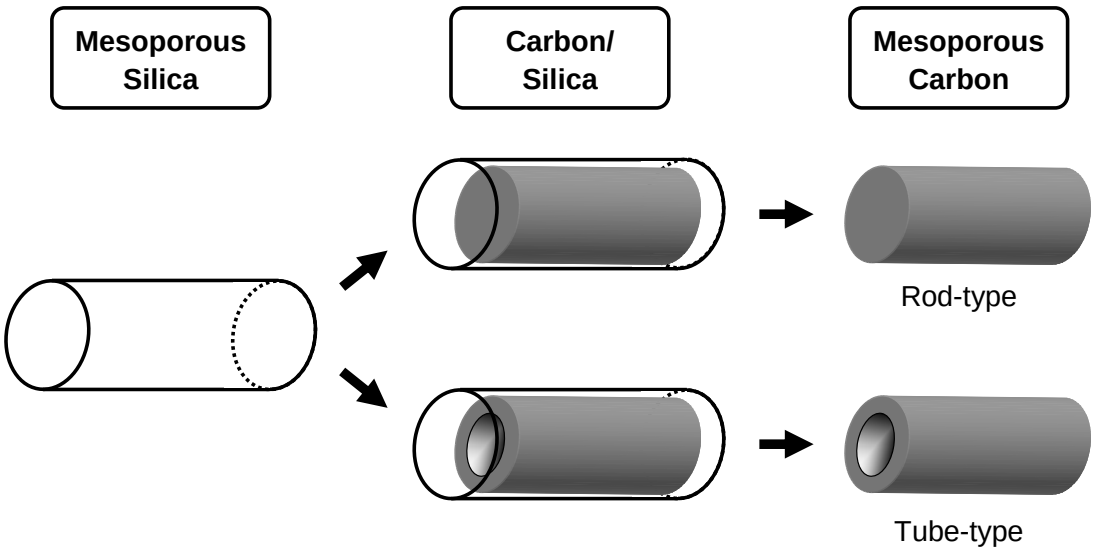

Figure 4.2. Different degrees of infiltration of the carbon precursor lead to different types of carbon structures.

Several different organic molecules can be used as carbon precursors in the nanocasting process and depending on the carbon source there is a choice of infiltration techniques available to fill the pores with the precursor. Solid precursors, like sucrose, are typically dissolved in a solvent and can be impregnated in the same

way as liquid precursor molecules, such as furfuryl alcohol. The chemical vapor deposition (CVD) process can be used to infiltrate gaseous monomers, including acetylene or propylene, which subsequently can be pyrolytically decomposed inside the pores. In the following step the carbon precursors have to be polymerized.

There are two common forms of polymerization of organic monomers: *addition polymerization* and *condensation polymerization*.[84] The addition polymerization process can be divided into three distinct stages. During the *initiation* step, an active center (free radical) is formed by a reaction between an initiator (or catalyst) and a monomer. This active center causes a chain reaction that attaches more and more monomer units to form a linear macromolecule during the *propagation* step. Finally, the reaction eventually comes to *termination* when two active end groups link together to form a non-reactive molecule. Typical polymers that can be prepared by addition polymerization are conventional plastics, such as polyethylene, polypropylene, and polystyrene. The second type, condensation polymerization (or *polycondensation*), is the formation of polymers by stepwise intermolecular chemical reactions between two monomer species where a small molecular weight by-product (like water) is eliminated. Polycondensation of organic species is analogous to the condensation reactions associated with silicon alkoxides discussed in the preceding chapters. A great advantage of condensation polymerization is that the reaction rates are generally slower than in addition polymerization, but more importantly that polycondensation can form cross-linked and network polymers. Polyesters, phenol-formaldehyde, nylon, polycarbonates are typical examples of polymers prepared through polycondensation. The most commonly used carbon precursors in nanocasting processes, such as sucrose, phenol-resin monomers, furfuryl alcohol, and acetylene or propylene gas (CVD), all undergo condensation type polymerization. Since furfuryl alcohol has single-handedly been used as the carbon source in this work a more thorough description of its polymerization chemistry will be presented here. Furfuryl alcohol (FA) is the most important furanic derivate on the market. All resins derived from FA are acid catalyzed which promotes a complex poly-condensation process leading to black cross-linked materials.[85] Parameters that affect the condensation reaction kinetics include the type and strength of acid, the presence of water, and the temperature. It is generally believed that the resinification of FA can take place trough two different mechanisms.[86] The more common mechanism consists of the condensation of the OH group with the mobile hydrogen atom of the

heterocycle at C5 to give structure (1) shown in Scheme 4.1. An alternative mechanism would be OH−OH condensation to give occasional CH_2OCH_2 linkages as in structure (2). Structure (1) is generally the end product here as well in consequence of acid-catalyzed loss of formaldehyde according to Scheme 4.1.

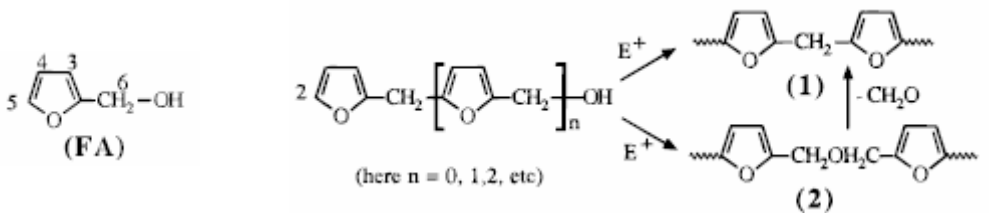

Scheme 4.1. General polycondensation mechanisms of furfuryl alcohol.

However, these two reaction pathways both result in linear chains and thus cannot be used to explain the progressive coloration and the branching of the polymer. Choura *et al.* have suggested the following mechanistic pathways to explain this feature. The color formation is believed to be caused by oligomers that undergo hydride-ion exchanges with the protonated chains of growing species, while the branching occurs through the interaction of terminal CH_2OH or disubstituted furan rings with non-furanic unsaturations. Curing of a polymer at elevated temperatures can alternatively be performed to further polymerize unreacted bonds prior to the pyrolytic decomposition to carbon (analogous to aging of silicates).

The finalizing of the chemical structure of the resulting carbon material takes place during the carbonization (pyrolysis) step, which is usually accomplished by heating the polymer/silica composite at elevated temperatures in the absence of oxygen or any other oxidizing reagents. During the carbonization step, organic material is pyrolyzed to an all-carbon material. The production of charcoal through the pyrolysis of wood has been widely used since early history. Depending on the carbon precursor and the experimental conditions different results are obtained, including the carbon yield and the graphitization degree.[87] The use of furfuryl alcohol typically gives a low crystallinity,[88] while pitch and aromatic polymers result in a carbon structure composed of highly ordered graphite layers.[87,89,90] An important issue when preparing carbon materials through nanocasting is that the pyrolysis should be restricted to the inside of the template pores. An effective method for the restriction of carbonization

is to place a suitable catalyst inside the pores, such as sulfuric acid for the decomposition of carbohydrates. Alternatively, the silica frameworks can be made acidic through incorporation of alumina. These acid catalysts catalyze the polymerization exclusively inside the region where the catalysts are located, so that subsequent carbonization results in the formation of nanostructured carbon inside the pores. Moreover, it is important that the silica template does not collapse during the carbonization heat treatment.

Finally, the silica template can be removed by leaching in concentrated hydrofluoric acid (HF) or hydroxide solutions (KOH or NaOH), in which the solubility of amorphous silica is high. Here, the HF treatment is the more effective method, but is at the same time also more hazardous. The carbon phase is nearly unaffected under these treatments. Potential application areas for the nanocast carbon replicas include electrode materials,[91–93] and hydrogen storage,[94,95] because of their high thermal stability, corrosion resistance, and high electronic conductivity (especially carbon with a graphitic skeleton).

4.2. Preparation of Nanocast Metal Oxide Materials

A wide variety of mesoporous metal oxide materials have been prepared by employing the same basic principal idea as for preparing nanocast carbon materials. Most of the silica templates that have been used for preparing carbon replicas can be used as molds here as well, including MCM–48 and SBA–15.[11–14] In addition, carbon materials, such as activated carbon[96,97] and nanocast carbon,[15–18] have also been used as metal oxide templates. Furthermore, Stein *et al.* have shown that it is possible to prepare a variety of metal oxides with macroporous (inverse opal) structures by using colloidal beads as templates.[98] The most commonly used metal oxide precursors are various salts of the desired metal, typically metal nitrates. However, the usage of metal alkoxides[15] and metal oxide colloids[46,47] has also been reported.

The precursor salts are typically dissolved in water or alcohol and the solution is infiltrated into the porous template by wet impregnation. The techniques differ depending on which type of precursor is used, since the precursor solution should be compatible with the template. Thus, when using a hydrophobic template like carbon a

more hydrophobic precursor should be employed, which is the case of the metal alkoxides.

When using salt solutions as precursors, the formation of the solid structure (freezing of the structure) is initiated by nucleation caused by the evaporation of the solvent during drying of the impregnated sample, followed by growth of the nuclei. It is important that the drying is not so rapid that the precursor molecules diffuse out of the mesopores together with the solvent. If the nuclei are located outside the mesopores, they can grow large in the same way as in bulk solutions. However, nucleation reactions often occur at surface defects and for mesoporous materials this is likely to occur inside the pores. Due to the confinement inside the mesopores, the salt crystals are not able to grow large. On the other hand, when using metal alkoxides or metal oxide colloids as precursors, sol-gel reactions take place in the same way as discussed for silicate species in the preceding chapters. However, one has to keep in mind that non-siliceous alkoxides (especially the transition metals) are much more reactive than silicon alkoxides and, thus, more difficult to control. Furthermore, nucleation and growth as well as sol-gel reactions behave differently inside confined spaces.

In the case of alkoxide precursors, the sol-gel reactions already produce the metal oxide to some extent, but also stable hydroxides or unreacted hydroxyl groups might still be present in the matrix. By heating the sample at elevated temperatures, these reactions will go to completion. Heating is also used to decompose the salts to oxides of the desired metal. Metal nitrates are preferred since they normally decompose at low temperatures, but also other types of salts, like chlorides, have successfully been used.[13,17] Simultaneous control of the temperature and the oxygen content in the oven makes it possible to control the oxidation state of the metal to some extent. Strongly reducing atmospheres may even reduce the oxide to pure metal. Moreover, increasing the temperature often modifies the initial amorphous structure to a more dense crystal structure. High temperatures are normally related to sintering of bulk oxides, meaning that initially small metal oxide crystals are fused together, resulting in a decrease of the specific surface area. However, sintering is normally not a problem in nanocasting processes, because the growth of the crystals is limited to the size of the mesopores of the template. Nonetheless, there are a few limitations at high temperatures associated with the different types of templates. Normally, mesoporous silicas are calcined at temperatures at around 550 °C and consequently deformations in the silica/metal

oxide composite might occur if higher temperatures are used in the heat treatments. On the other hand, silica is very redox stable and will not have an effect on the oxidation state of the metal. Then again, when using carbon materials as hard templates it is important that high temperature treatments of the composite should be carried out in an inert atmosphere to avoid decomposition of the carbon structure. After having finalized the structure of the metal oxide, the carbon template can be removed by combustion in oxygen. However, oxidation of carbon might also lead to unwanted reduction of the metal oxide. Similar as in the preparation of carbon replicas, the silica template can be removed by selective leaching of the silica phase. This indicates that that only mesoporous materials of metal oxides that are insoluble (or have low solubility) in either NaOH or hydrofluoric acid can be prepared by using silica as a template. However, there are still a lot of different oxides that fulfill this criterion, including Co_3O_4, SnO_2, MnO_x, Cr_2O_3, In_2O_3, CeO_2, NiO, and Fe_2O_3.

There are several potential application areas available for the metal oxide replicas. Replicas of metal oxides that are chemically resistant at high pH are good candidates to be used as stationary phases for reversed-phase liquid chromatography.[99] Catalytically active oxides, might be used as catalysts or catalyst supports, either in a pure oxide form or as mixtures of oxides. Furthermore, oxides that have semiconductor properties can among other things be used as gas sensor material. In all these applications, the nanocast oxides are superior to conventional oxide materials due to their comparatively large surface areas.

5. Aim of the Study

The aim of the study was to prepare monoliths of different chemical compositions with pores arranged in a hierarchical fashion with rationally controllable pore diameters, macroscopic size and shape. Sol-gel chemistry has previously been successfully applied for synthesizing silica monoliths with a hierarchical meso-macroporous structure. Here, the size and the shape of the monoliths are controlled by casting a homogeneous sol prepared from silicon alkoxides in a mold of desired shape. Furthermore, by adding a hydrogen bonding polymer, poly(ethylene glycol), to the starting sol, a phase separation close to the sol-gel transition can be induced. By proper adjustment of the polymer amount, the timing of the onset of the phase separation relative to the sol-gel transition can be controlled and, thus, also the size of macropores can be adjusted. Moreover, the macropore walls (gel skeleton) also contain textural pores between silica particles, which size can be expanded by solvent exchange post treatments in ammonia solutions as a result of the Ostwald ripening mechanism. In the present work, this approach was extended to the use of mixed surfactant-polymer templates in the synthesis, which resulted in silica monoliths exhibiting a three-modal, fully interconnected porosity; small mesopores (diameter 2–4 nm) templated by supramolecular surfactant aggregates, larger textural mesopores (10–20 nm), and macropores (0.5–30 μm) are arranged in a hierarchical fashion. The diameter of all modes of pores can be controlled independently.

It is difficult to generalize this synthesis approach to also cover the synthesis of other (transition) metal oxides. Thus another aim of the study was to investigate the applicability of the nanocasting technique for the preparation of such monoliths. Using the silica monoliths as the mold, carbon and different non-siliceous metal oxide monoliths were successfully prepared. In this case, the control of the replica structure is different depending on the length-scale. The monolithic replicas are positive replicas of the starting silica monoliths on the micrometer length-scale, meaning that the macroscopic shape and the macropore structure of the replicas can be controlled by altering the silica monoliths. On the other hand, other means are needed to change the structure on the nanometer level. The carbon or metal oxide structure is a negative replica of the silica monolith, meaning that the pore walls of the silica mesopores become mesopores in the replica monolith and vice versa. The monoliths have been

thoroughly characterized at different stages of the synthesis in order to give a description of the reaction steps responsible for the development of these interesting structures.

6. Experimental

Two distinct synthesis approaches have been used to prepare hierarchically porous monoliths. The first method describes how silica monoliths containing both macropores and mesopores can directly be prepared from a one-batch synthesis strategy. Depending on the used structure directing agents, either silica monoliths with bimodal or trimodal pore structures can be prepared.

The second method describes how these silica monoliths can further be used as hard templates in the preparation of nanocast carbon and non-siliceous metal oxide replicas. Here, variations in either the starting silica template or the synthesis parameters can be used to control the final replica structure.

Finally, the most important characterization techniques will be described in detail.

6.1. Direct Synthesis of Hierarchically Porous Silica Monoliths

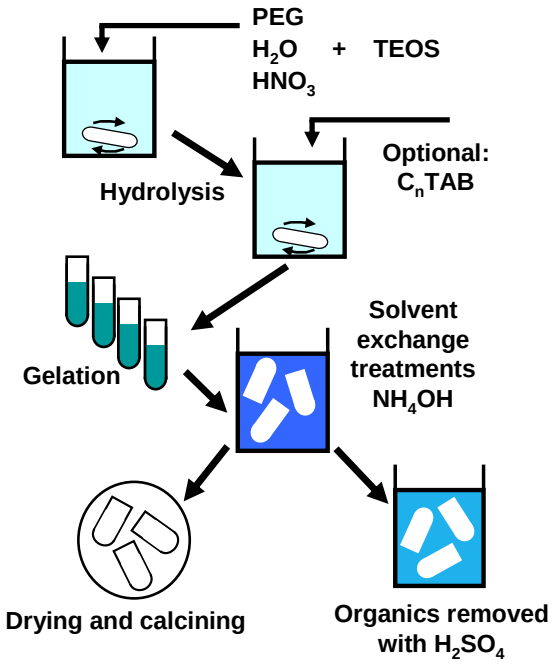

Scheme 6.1. Synthesis description for the preparation of silica monoliths with either bimodal or trimodal pore structures.

Table 6.1. Starting molar compositions and post treatment parameters of the different samples.

Comp	TEOS	H_2O	HNO_3	PEG	$C_{14}TAB$	$C_{16}TAB$	$C_{18}TAB$	Solvent Exchange	Publ	Sample name
S1	1.00	14.69	0.25	$6.86 \cdot 10^{-4}$				1.0 M NH_4OH	I	P-54
S2	1.00	14.69	0.25	$7.31 \cdot 10^{-4}$				1.0 M NH_4OH	I	P-58
S3	1.00	14.69	0.25	$7.77 \cdot 10^{-4}$				1.0 M NH_4OH	I	P-62
S4	1.00	14.69	0.25	$8.23 \cdot 10^{-4}$				1.0 M NH_4OH	I	P-65
S5	1.00	14.69	0.25	$8.69 \cdot 10^{-4}$				1.0 M NH_4OH	I	P-69
S6	1.00	14.69	0.25	$6.86 \cdot 10^{-4}$		0.000		1.0 M NH_4OH	I	S-00
S7	1.00	14.69	0.25	$6.86 \cdot 10^{-4}$		0.004		1.0 M NH_4OH	I	S-04
S8	1.00	14.69	0.25	$6.86 \cdot 10^{-4}$		0.007		1.0 M NH_4OH	I	S-07
S9	1.00	14.69	0.25	$6.86 \cdot 10^{-4}$		0.011		1.0 M NH_4OH	I	S-11
S10	1.00	14.69	0.25	$6.86 \cdot 10^{-4}$		0.014		1.0 M NH_4OH	I	S-14
S11	1.00	14.69	0.25	$6.86 \cdot 10^{-4}$		0.018		1.0 M NH_4OH	I	S-18
S12	1.00	14.69	0.25	$6.86 \cdot 10^{-4}$		0.021		1.0 M NH_4OH	I	S-21
S13	1.00	14.69	0.25	$6.86 \cdot 10^{-4}$		0.029		1.0 M NH_4OH	I	S-29
S14	1.00	14.69	0.25	$6.86 \cdot 10^{-4}$		0.044		1.0 M NH_4OH	I	S-44
S15	1.00	14.69	0.25	$6.86 \cdot 10^{-4}$		0.059		1.0 M NH_4OH	I	S-59
S16	1.00	14.69	0.25	$6.86 \cdot 10^{-4}$		0.074		1.0 M NH_4OH	I	S-74
S17	1.00	14.69	0.25	$6.86 \cdot 10^{-4}$		0.090		1.0 M NH_4OH	I	S-90
S18	1.00	14.69	0.25	$4.33 \cdot 10^{-4}$		0.137		1.0 M NH_4OH	I	PS-34/137
S19	1.00	14.69	0.25	$3.24 \cdot 10^{-4}$		0.187		1.0 M NH_4OH	I	PS-26/187
S20	1.00	14.69	0.25	$5.01 \cdot 10^{-4}$	0.105			1.0 M NH_4OH	I	CL-14
S21	1.00	14.69	0.25	$5.01 \cdot 10^{-4}$	0.052	0.052		1.0 M NH_4OH	I	CL-14/16
S22	1.00	14.69	0.25	$5.01 \cdot 10^{-4}$		0.105		1.0 M NH_4OH	I	CL-16
S23	1.00	14.69	0.25	$5.01 \cdot 10^{-4}$		0.052	0.052	1.0 M NH_4OH	I	CL-16/18
S24	1.00	14.69	0.25	$5.01 \cdot 10^{-4}$			0.105	1.0 M NH_4OH	I	CL-18
S25	1.00	14.69	0.25	$8.23 \cdot 10^{-4}$				Various	II	Sample A-G
S26	1.00	14.69	0.25	$7.77 \cdot 10^{-4}$				1.0 M NH_4OH	III	[a]SM-40
S27	1.00	14.69	0.25	$7.77 \cdot 10^{-4}$				0.1 M NH_4OH	III	[b]SM-40
S28	1.00	14.69	0.25	$7.77 \cdot 10^{-4}$				0.01 M NH_4OH	III	[c]SM-40
S29	1.00	15.77	0.28	$7.77 \cdot 10^{-4}$				1.0 M NH_4OH	IV	SiO_2
S30	1.00	14.69	0.25	$4.33 \cdot 10^{-4}$		0.137		1.0 M NH_4OH	V	SM
S31	1.00	14.69	0.25	$6.86 \cdot 10^{-4}$				1.0 M NH_4OH/ 60% H_2SO_4/H_2O_2	VI	SiO_2
S32	1.00	15.77	0.28	$7.77 \cdot 10^{-4}$				1.0 M NH_4OH	VII	SiO_2
S33	1.00	14.69	0.25	$4.33 \cdot 10^{-4}$		0.137		1.0 M NH_4OH	VII	CTAB-SiO_2

6.1.1. Silica Monoliths with Polyethylene Glycol as Pore Structure Directing Agent

By using a similar approach as described by Nakanishi *et al.* silica monoliths with a bimodal hierarchical macro- and mesoporous structure could be prepared (see scheme 6.1.). These silica monoliths were synthesized by adding tetraethoxysilane, TEOS, to a mixture of polyethylene glycol (PEG, with an average molecular weight of 35,000 g/mol) in aqueous nitric acid solution. Depending on the amount of added PEG the size of the macropores could easily be controlled (*compositions S1–S5*). The sols were subsequently stirred at room temperature until homogeneous, clear solutions were obtained. The sols were cast into molds (microtiter plates) and were left to gel at 40 °C, which took place within 6–10 h. After the gelation point the monoliths were aged for at least 48 h at 40 °C in their mother liquids.

In order to prevent the monoliths from cracking or shrinking too much during the drying step, solvent exchange post treatments were carried out to increase the degree of condensation, and thus the stability, of the silica gels.[100] Simultaneously, the size of the textural mesopores is enlarged by the Ostwald ripening process. An efficient procedure to obtain mechanically stable monoliths with large textural mesopores was to keep the monoliths in 1 M NH_4OH solution (10 times the volume of the monoliths) for at least 9 h at 90 °C. The size of the textural pores was also varied by altering the NH_4OH concentration (*compositions S26–S28*). The monoliths were dried for 3 days at 60 °C in open beakers. Typically, the organic matter was removed by calcination at 550 °C for 5 h in air with a heating ramp of 1 K/min. Alternatively, the PEG molecules could be chemically removed by a second post treatment step in sulfuric acid solution at 95 °C prior to the drying step. From TG/DTA analysis (Figure 6.1.) it is clear that a treatment in 48 wt % H_2SO_4 (after the NH_4OH treatment) is sufficient to remove the remaining PEG, which is evident from the disappearance of the exothermic peak at ~ 210 °C.

To compare the amount of surface silanol groups for samples prepared with the two different removal methods, surface functionalization with two functional silanes with different chain lengths, trimethylchlorosilane (TMCS) and octadecyldimethyl-chlorosilane (ODMCS), was performed. Prior to surface functionalization, both monoliths were dried in vacuum at 250 °C for 12 h. They were then immersed in a toluene solution of the functional silane.

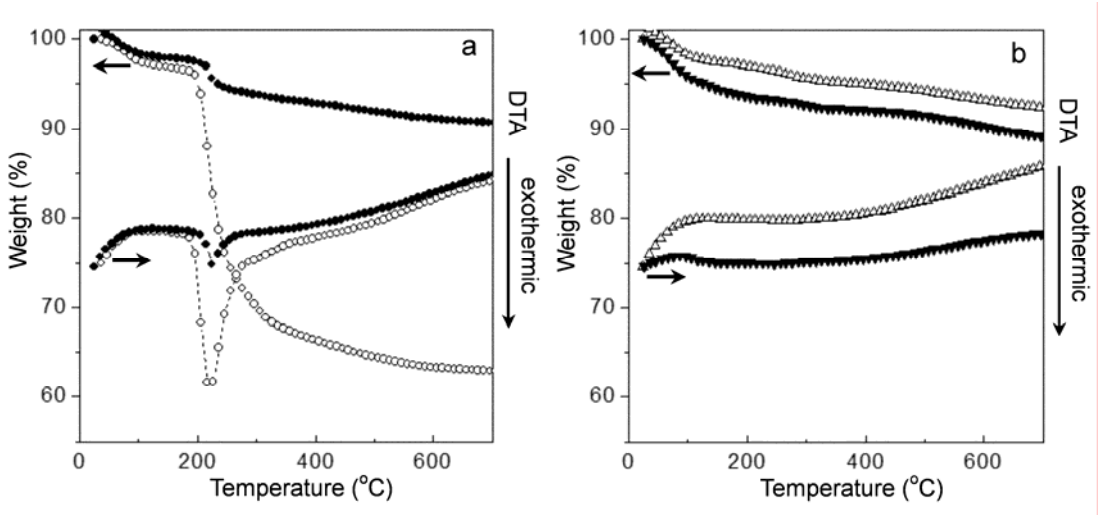

Figure 6.1. TG/DTA analysis of the as-prepared monoliths (○), monoliths treated with NH_4OH (●), monoliths treated with NH_4OH and subsequently with 48 wt % H_2SO_4 (△), and monoliths treated with 48 wt % H_2SO_4 together with 10 wt % H_2O_2 (▼).

6.1.2. Silica Monoliths with Polyethylene Glycol and Cetyltrimethylammonium Bromides as Pore Structure Directing Agents

The synthesis pathway of silica monoliths with a trimodal pore structure resembles to a large extent the earlier described method in chapter 6.1.1. However, in this case, an additional structure directing agent, cetyltrimethylammonium bromide, C_nTAB (n = 16), was added after complete hydrolysis of TEOS to create small surfactant templated mesopores of about 4 nm in diameter (*compositions S6–S19*). At this stage, enough ethanol molecules have been released to easily dissolve the surfactant. Moreover, the use of C_nTAB with different hydrocarbon chain lengths (n = 14–18) were studied to alter the size of the mesopores (*compositions S20–S24*). Solvent exchange post-treatments in ammonia were also applied for these monoliths as well as the drying and calcination steps described in the previous chapter.

6.2. Nanocasting

6.2.1. Hierarchically Porous Carbon Monoliths Prepared through Nanocasting

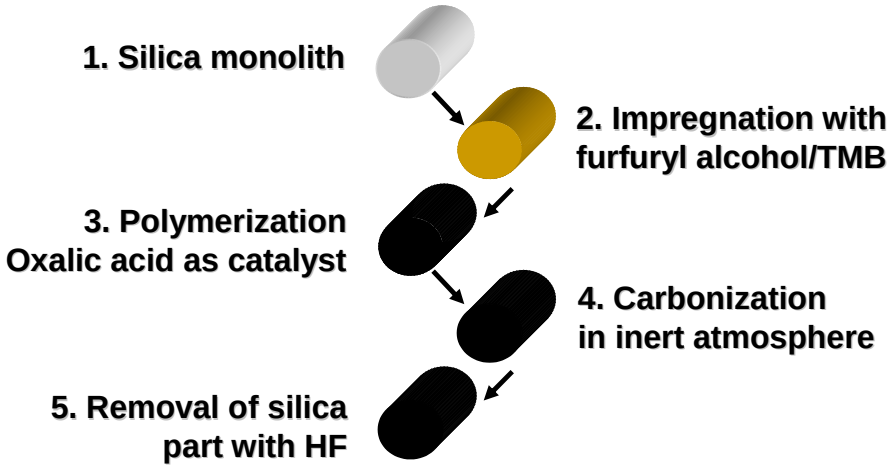

Scheme 6.2. The preparation of carbon monoliths by the nanocasting procedure.

Mechanically stable macroporous/mesoporous carbon monoliths could be obtained by using the nanocasting procedures described in Scheme 6.2. and Table 6.2. The silica monoliths which were used as molds (or hard templates) in the nanocasting process were prepared according to the earlier described methods in chapters 6.1.1. and 6.1.2 (*compositions S26–S30*). The carbon precursor (furfuryl alcohol, FA) was introduced together with a catalyst (oxalic acid, OxA) in the pore system of the SiO_2 monoliths by impregnation (n_{FA}/n_{OxA} = 200–300). Complete impregnation was confirmed when the monoliths had become fully transparent. Alternatively, the furfuryl alcohol was dissolved in 1,3,5-trimethylbenzene, TMB, in order to dilute the carbon precursor (0–90 vol % TMB). The polymerization of FA was carried out at low temperatures (see Table 6.2. (a) for details). If no catalyst was used the impregnation and polymerization step had to be repeated in order to obtain a rigid monolith (method M1). The silica polymer composite was then cured to increase the cross-linking of the molecules and subsequently the polymer was carbonized at elevated temperatures under an inert atmosphere. Finally, to obtain the carbon replica, the silica portion of the composite was removed by etching in aqueous hydrofluoric acid solution. **Note! Since HF is a very hazardous substance it was handled with caution.**

Table 6.2. Synthesis parameters for the different carbon monoliths.

a) Synthesis methods

Method	Starting Silica Monoliths	Impregnation Technique	Catalyst	Number of Impregnations
M1	S29	Incipient wetness	-	2
M2	S26-S28, S30	Impregnation	Oxalic acid	1

Method	Polymerization	Curing	Carbonization	Template Removal	Publ.
M1	90°C for 15 h	-	800 °C (5 h, N_2)	9% HF	IV
M2	60 °C (24 h) / 80 °C (24 h)	150/300 °C in Ar	850 °C (4 h, Ar)	20-40% HF	III, V

b) Samples prepared by using method M2

SiO_2/carbon Composite	Carbon Replica	Starting SiO_2	FA [vol %]	TMB [vol %]	Publ.	Sample Names Composite	Sample Names Replica
SC1	**C1**	S26	40	60	III	[a]SCM40	[a]CM40
SC2	**C2**	S27	40	60	III	[b]SCM40	[b]CM40
SC3	**C3**	S28	40	60	III	[c]SCM40	[c]CM40
SC4	**C4**	S26	20	80	III	SCM20	CM20
SC5	**C5**	S26	30	70	III	SCM30	CM30
SC6	**C6**	S26	40	60	III	SCM40	CM40
SC7	**C7**	S26	60	40	III	SCM60	CM60
SC8	**C8**	S26	80	20	III	SCM80	CM80
SC9	**C9**	S26	100	0	III	SCM100	CM100
-	**C10**	S26	40	60	-	-	-
-	**C11**	S14	40	60	-	-	-
-	**C12**	S16	40	60	-	-	-
-	**C13**	S22	40	60	-	-	-
-	**C14**	S18	40	60	-	-	-
-	**C15**	S19	40	60	-	-	-
SC16	-	S30	10	90	V	SCM-10	-
SC17	**C17**	S30	20	80	V	SCM-20	CM-20
SC18	**C18**	S30	30	70	V	SCM-30	CM-30
SC19	**C19**	S30	40	60	V	SCM-40	CM-40
SC20	**C20**	S30	60	40	V	SCM-60	CM-60

6.2.2. Hierarchically Porous Metal Oxide Monoliths Prepared through Nanocasting

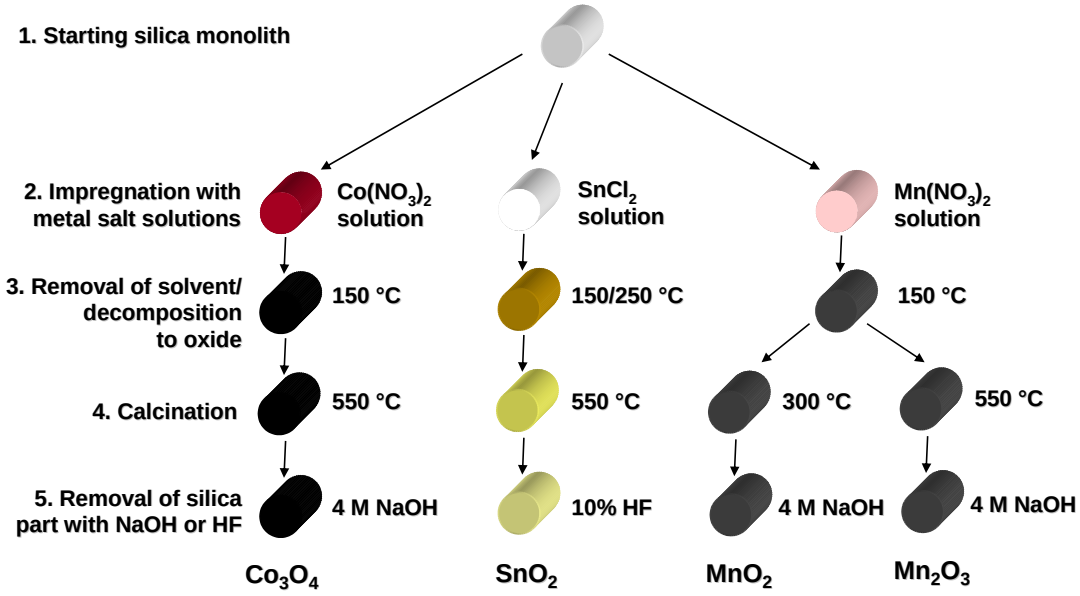

Scheme 6.3. Synthesis pathways to obtain different metal oxide monoliths through the nanocasting procedure.

A similar synthesis strategy as the one described for the carbon monoliths was utilized to prepare hierarchically porous metal oxide monoliths according to Scheme 6.3. and Table 6.3. Also here, the silica monoliths described in chapter 6.1.1. or 6.1.2. were used as molds (*compositions S31–S33*). $Co(NO_3)_2 \cdot 6H_2O$, $SnCl_2 \cdot 2H_2O$, and $Mn(NO_3)_2 \cdot 4H_2O$ were used as cobalt, tin and manganese oxide precursors, respectively. The outgassed silica monoliths were impregnated with aqueous solutions of the metal salts by incipient wetness. The wet, fully transparent monoliths were placed on crucibles and heated directly at either 150 °C for 10 h (for the cobalt and manganese nitrate solutions) or 150 °C for 4 h and then 250 °C for 4 h (for the stannous chloride solution). Depending on which salt was used, the impregnation and heating steps were repeated 2–4 times to ensure a rigid metal oxide structure. Subsequently, the composites were calcined in air at 550 °C (or 300 °C to obtain MnO_2) for 6 h with a heating ramp of 1 K/min to ensure a complete conversion to the metal oxides as well as to obtain fully crystalline structures. Finally, the silica part was removed by dissolution in either 4 M NaOH (at 90 °C, 2 × 24 h) or 10% HF (at room temperature, 24 h).

Table 6.3. Synthesis parameters for the different metal oxide monoliths.

Silica/Metal Oxide Composite	Metal Oxide Precursor	Salt Concentration [wt %]	[M]	No. Impr.	% Mass Increase
SiO_2/Co_3O_4	$Co(NO_3)_2 \cdot 6\ H_2O$	78.6	5.34	3	293.5
SiO_2/SnO_2	$SnCl_2 \cdot 2\ H_2O$	66.7	6.72	3	516.0
SiO_2/MnO_2	$Mn(NO_3)_2 \cdot 4\ H_2O$	50.0	3.10	5	323.7
SiO_2/Mn_2O_3	$Mn(NO_3)_2 \cdot 4\ H_2O$	50.0	3.10	5	296.3
CTAB-SiO_2/SnO_2	$SnCl_2 \cdot 2\ H_2O$	66.7	6.72	3	625.1

6.3. Characterization Methods

Due to the hierarchical structure of the monoliths several characterization techniques are needed to allow for a full characterization. However, only the most significant techniques will be described here in detail. Other used techniques will be shortly described in Chapter 7 (the results and discussion part).

6.3.1. Scanning and Transmission Electron Microscopy

Scanning electron microscopy (SEM) is an excellent technique to study monoliths on the micrometer scale, including macropore size as well as macropore wall thickness and roughness. With a scanning electron microscope it is possible to magnify an object more than with a common optical microscope.[101] Since an SEM irradiates a sample with electrons, one can say that electrons in an SEM function similar to the light in optical microscopes. The electrons are generated by a tungsten-filament and are accelerated through a column towards the sample in the sample chamber. The acceleration is driven by a potential difference (normally 10–20 kV) that exists between the filament and the sample. Therefore, the electrons will have energies of about 10–20 keV when they hit the sample. Newer instruments based on Field Emission SEM use much lower voltages which allows a higher resolution in the images. In order for the electrons to hit the sample, both the column and the sample chamber must be kept under vacuum. To produce an image of the sample surface, the electron beam scans over the sample, which can be done by using an electromagnetic lens. Primary electrons, which are electrons coming directly from the electron beam, can enter the sample and refract around one or several atom nuclei, exiting the sample

with nearly unchanged energy. These are called *backscattered electrons*, and are easily detected. Since heavier nuclei refract more electrons than lighter nuclei, the method can be used to show the atomic number contrast in the sample. When primary electrons from the electron beam collide with nuclei in the sample, also *secondary electrons* are emitted from the sample. Secondary electrons have low energy compared to the primary electrons (about 20 eV and 15000 eV, respectively). Since the secondary electrons have such a low energy, only those electrons excited at the surface manage to leave the sample. The scattering of electrons is received from a small area at a time and an image with high resolution and magnification is achieved. Since the sample is irradiated with electrons, the sample has to be conductive to be able to lead away the excess electrons. The excess electrons cause a deceleration and a bending of the electron beam, which deteriorate both image and analysis quality. If the sample is not conductive by itself, it has to be coated with a conductive layer of carbon or gold. Often an X-ray detector is attached to the SEM, which makes elemental analysis of the sample possible (energy dispersive spectroscopy, EDS).

For even higher resolution images a transmission electron microscope (TEM) can be used. Here, the detector is placed on the opposite side of the sample and only electrons that can pass through the sample are detected. Thus, the thickness of the sample should be as thin as possible so that the electron beam can penetrate the sample. The following SEM instruments have been used in this study: LEO 1560, LEO type stereoscan 360, Hitachi S–3500N. A Hitachi HF 2000 instrument was used for TEM studies and an Oxford Inca EDS system was used for the EDS determinations.

6.3.2. Nitrogen Physisorption

Nitrogen physisorption is a widely used analysis technique for studying structures on the nanometer scale.[102] It gives insights in the specific surface area, the pore volume and the pore size distribution of the material. First, an adsorption/desorption isotherm has to be recorded, which is done by calculating the amount of adsorbed N_2 as a function of the relative pressure P/P_0 at a constant temperature (77 K). Further analysis of the isotherms yields information about the surface characteristics of the material. There are six main types of physical adsorption isotherms according to the

IUPAC classification (see Figure 6.2.).[103] The shape of these isotherms is mainly determined by two factors, namely the strength of the adsorbent-adsorbate interactions and the type of porosity (or porosities) the sample contains.

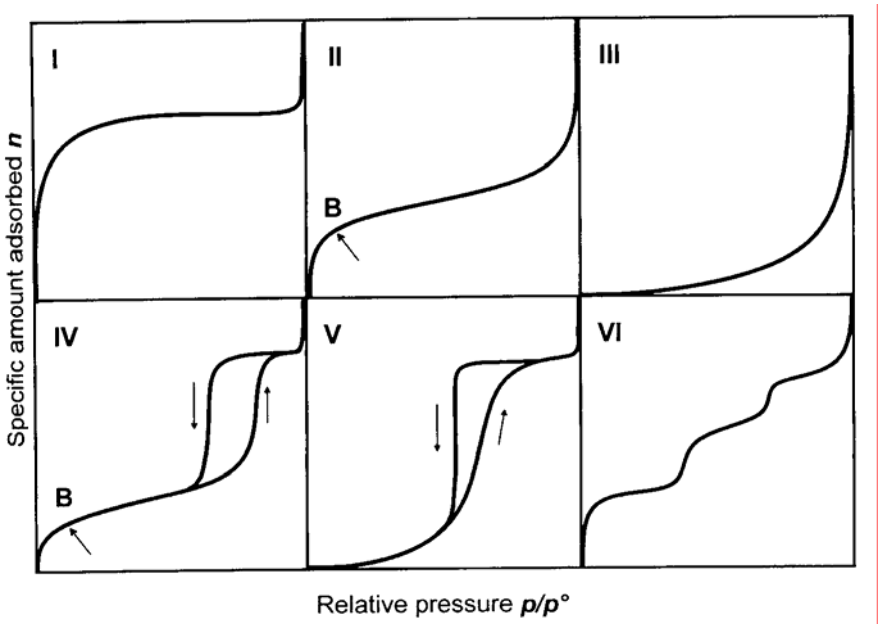

Figure 6.2. The six main types of physisorption isotherms.[103]

The *Type I* isotherm which is characteristic for its steep nitrogen uptake at low P/P_0 is associated with microporosity. *Type II* and *Type III* are both typical for non-porous or macroporous samples, however the difference between them are due to either strong or weak adsorbent-adsorbate interactions, respectively. The same reason is responsible for the difference between the *Type IV* and *Type V* isotherms. Here, the nitrogen uptake at higher P/P_0 is related to capillary condensation inside mesopores, which also leads to the characteristic hysteresis effect of the adsorption and desorption branch. The shape of the hysteresis loop can also be employed to receive information about the pore structure. The *Type VI* isotherm is relatively rare and is associated with layer-by-layer adsorption on a highly uniform surface.[104] The samples studied in our work are mainly of *Type IV* and to some extent also combined with *Type I* isotherms. The *specific surface area* can be determined by the BET method (Brunauer, Emmett and Teller) from the physisorption isotherm data. First, it is necessary to construct the BET plot and from that derive the value of the monolayer capacity, n_m.

$$\frac{P/P_0}{n(1-P/P_0)} = \frac{1}{n_m C} + \frac{C-1}{n_m C} \cdot \frac{P}{P_0} \qquad (6.1.)$$

The *C* constant is related to the sharpness of the point *B* indicated in Figure 6.2. and the value is sensitive both to surface polarity and to the presence of microporosity. To obtain a reliable result the C value normally should lie between 50 and 200. If this criteria is fulfilled, the specific surface area, *A*(BET), can be calculated. This calculation requires the knowledge of the average area, a_m, occupied by each molecule in the completed monolayer (a_m for N_2 at 77 K is normally taken to be 0.162 nm^2). Furthermore, it is customary to take the total *specific pore volume*, v_p, of an adsorbent as the liquid volume adsorbed at the end of the pore filling. However, this procedure is not always satisfactory, because the adsorption capacity (when P/P_0 approaches 1) is dependent on the magnitude of the external area and also the upper limit of the pore distribution. If the isotherm does not reach a plateau at high relative pressures the v_p is usually obtained at a predetermined P/P_0 close to 1. Determination of the *pore diameter* (or *pore width*) of mesopores is based on the concept of capillary condensation and the application of the Kelvin equation:

$$\ln\frac{P}{P_0} = -\frac{2\gamma V_m}{r_K RT} \qquad (6.2.)$$

where γ is the surface tension and V_m the molar volume of the liquid. The Kelvin equation gives the dependence between P/P_0 and the mean radius of the meniscus r_K. By adding the thickness of the adsorbed multilayer (t) to r_K, the radius of the cylindrical pore (r_P) is obtained. There are several different models for calculating the pore size distribution of which the Barrett-Joyner-Halenda (BJH)[105] is the most applied method. However, the BJH method which is based on the Kelvin-Cohan equation, is inaccurate for pores even as large as 20 nm[106] and, more specifically, it underestimates the pore size by ~ 1 nm in the 2–4 nm pore size range.[107] Even if the BJH model is inaccurate in determining the absolute pore size it is useful for comparing pore sizes of different materials. An alternative and more accurate way to determine the pore size distribution is to use *density functional theory* (DFT).[106,107] Based on statistical mechanics, DFT is used to create equilibrium density profiles for

all locations inside the pore, which are obtained by minimizing the free-energy functional. This free-energy potential also includes attractive and repulsive contributions of the fluid-fluid and fluid-wall interactions, which can be obtained by the *non-local density functional theory* (NLDFT). The final step is to compare the experimental isotherm with "single pore" isotherms determined by NLDFT to obtain the pore size distribution. Comparison between pore sizes determined by the BJH model and NLDFT is presented in Figure 6.3 and as can be seen the deviation is most noticeable for small pore sizes. Nonetheless, both models start from the assumption that pores are rigid and of well-defined shape but in reality the pores could be of irregular shape or composed of complex interconnected voids of various sizes. Also the choice of branch used in the calculations affects the extracted pore size.

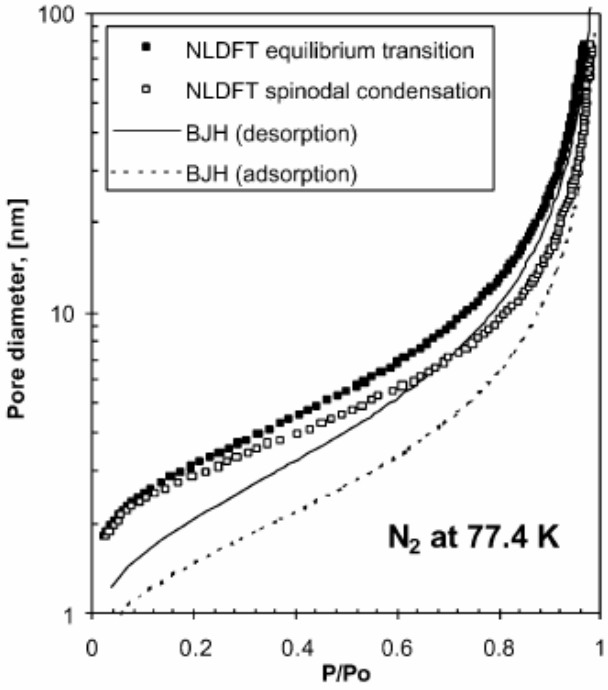

Figure 6.3. Capillary hysteresis of nitrogen in cylindrical pores at 77.4 K. Equilibrium desorption (■) and spinodal condensation (□) pressures predicted by the NLDFT in comparison with the results of the KC equations (BJH method) for hemispherical (–) and cylindrical (---) menisci.

A useful tool to determine the micropore area and micropore volume of materials exhibiting *Type I* isotherms is to construct a *t*-plot, i.e. the multilayer thickness versus P/P_0, for nitrogen adsorption at 77 K. The thickness, *t*, of an adsorbed multilayer is usually calculated using the Harkins and Jura equation. The external surface area of

the sample can be derived from the slope of the *t*-plot. The micropore area can then be established by subtracting the external surface area from the total surface area (A_{BET}). More importantly, the micropore volume can be calculated directly from the *t*-plot y-axis intercept.

All nitrogen sorption measurements in this work were performed on ASAP 2010 instruments (Micromeritics) at 77 K. The DFT calculations were performed on the Autosorb 1 for Windows 1.25 software (Quantachrome Instruments).

6.3.3. Mercury Porosimetry

Contrary to nitrogen physisorption, mercury porosimetry is not limited only to small pore sizes. The technique allows determination of the accessible *total pore volume*, *sample densities* (bulk and skeletal), and *porosity* directly from the measurement, while by applying the Laplace equation (6.3) the *pore size distribution* and the *pore area* in the meso- and macropore range can be deduced.[108,109] The analysis technique is based on the intrusion of mercury into a porous structure under stringently controlled pressures. From the pressure versus intrusion data, the porosimeter generates volume and size distributions using the Laplace equation (in some cases also called the Washburn equation):

$$d = -4\gamma \cos\theta / P \qquad (6.3.)$$

Here, γ is the surface tension and θ is the contact angle in the liquid/solid interface. Since mercury does not wet most substances and will not spontaneously penetrate most pores by capillary action, it must be forced into the pores by the application of external pressure, *P*. The required pressure is inversely proportional to the diameter of the pores, *d*. Only a slight pressure is required to intrude mercury into large macropores, whereas much greater pressures are required to force mercury into mesopores. A plot of these data is called the intrusion curve. When the pressure is reduced, mercury leaves (or extrudes) the pores. This exit process of mercury is monitored and plotted as the extrusion curve. The low-pressure analysis, which proceeds from 690 Pa upward to any pressure between ambient and 345 kPa, provides data for characterization of macropores in the range 360 μm to 3.6 μm. If mesopores

are to be characterized, or if total porosity or skeletal density is to be determined, a high-pressure analysis is also required. For this analysis, the penetrometer is moved to the high-pressure stations where data are collected at pressures between ambient and as high as 400 MPa. Using these high pressures, an intrusion/extrusion plot for diameters in the range of 6 µm to 0.003 µm can be determined. The penetrometer is both a sample holder and a volume measuring transducer. If high pressures are applied sample compression could occur. Sample compression is one reason why data obtained in the smaller size range by mercury porosimetry may differ from data obtained in the same range by nitrogen sorption. Since Hg-porosimetry and N_2-adsorption are not based on the same principle, differences in measurements might also be observed when comparing the two methods. In this work all mercury porosimeter measurements were carried out on an AutoPore III mercury porosimeter (Micromeritics) and a contact angle of 130° as well as a surface tension value of 0.485 N/m was assumed in the pore size calculations.

7. Results and Discussion

7.1. Hierarchically Porous Silica Monoliths

By direct observations and by electron microscopy it was found out that the prepared silica monoliths were hierarchically porous, i.e. exhibited porosity on several length scales arranged in a structure-within-structure fashion (Figure 7.1.). Additionally, it was also possible to control the size of each specific pore size range by simple adjustments, for instance by changing the starting chemical composition. A more detailed description of the pore size control will follow in the subsequent chapters and in Papers I and II.

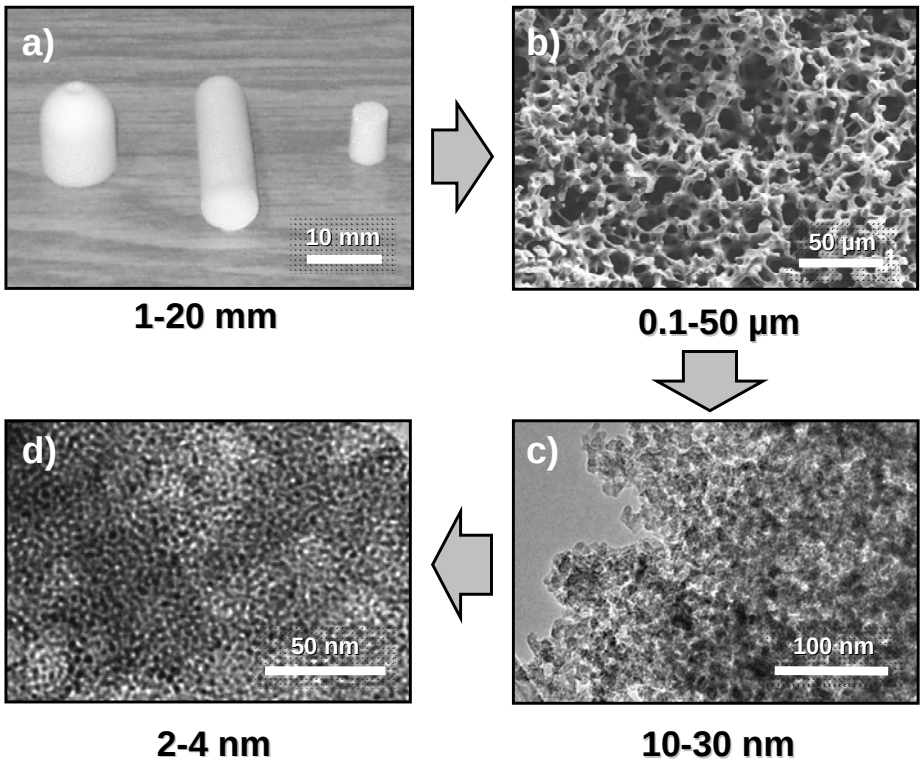

Figure 7.1. Hierarchical structure of the silica monoliths and in which ranges these can be altered: a) The macroscopic shape of the monoliths, b) the macropore structure, c) the interparticle voids (textural mesopores), and d) the surfactant templated mesopores.

7.1.1. Control of the Macroscopic Shape of the Monoliths

The macroscopic size and shape of the silica monoliths are easily controlled by allowing the sols to gel in vessels of desired shape as exemplified in Figure 7.1a. Virtually any shape and size is possible to prepare. However, when the size is increased the post-treatment and drying steps become more challenging, as a result of diffusion problems and capillary pressure gradients. After the gelation point the monoliths shrink to a small extent caused by syneresis effects. Then liquid is expulsed from the pores due to ongoing condensation reactions, which on the other hand makes it easier to remove the gels from the synthesis vessels. The shrinkage at this stage is significantly dependent on the starting composition of the sol and lies in the range of 15–25% of the monolith diameter. The addition of CTAB reduces the shrinkage, probably because of blocking of reactive –OH groups. Also macroscopic phase separation induced by a too small amount of PEG leads to settling of the silica scaffold, which then again gives rise to shorter monoliths. Further macroscopic shrinkage often occurs during the drying and during the calcination steps due to the capillary pressure inside the mesopores. To a large extent this can be prohibited by utilizing various chemical post-treatments. This has been studied in Paper II by visually determining the shrinkage of as-synthesized monoliths treated with various solutions according to Scheme 7.1. The shrinkage of the diameter of cylindrical monoliths is listed in Table 7.1.

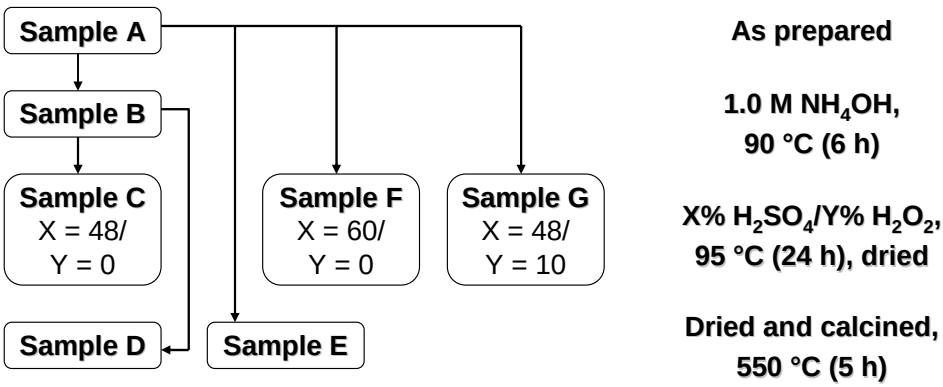

Scheme 7.1. The different solvent exchange post-treatment properties for samples A–G.

Table 7.1. The shrinkage of the diameter of the monoliths with respect to the as-synthesized sample (A) in Scheme 7.1.

Sample	A	B	C	D	E	F	G
Shrinkage	Standard	3.6%	3.6%	5.7%	27.6%	6.2%	6.2%

Monoliths that have been dried and calcined without any post-treatment display the largest shrinkage of 27.6% (Sample E). However, by treating the monoliths in ammonia solutions the shrinkage can be remarkably reduced due to a dissolution and re-precipitation process that strengthens the silica scaffold (Ostwald ripening). Simultaneously, the mesopore size is also increased leading to a reduction of the capillary pressures inside the pores and further shrinkage is inhibited. These effects can be distinguished for the dried samples B and C and even for the calcined sample D, which has not shrunk more than 5.7%. The same effect can also be observed for monoliths treated in H_2SO_4 (samples F and G). However, here the shrinkage is slightly more pronounced than for the monoliths treated in NH_4OH, due to the lower solubility of silica under this treatment. As we shall see, the solvent exchange post-treatments also have a significant effect on the textural mesopores, the surface area and the surface chemistry of the silica monoliths.

7.1.2. Structure Control of the Macropores

As previously described by Nakanishi *et al.* it is possible to create a silica gel with a macroporous structure by adding a hydrogen bonding polymer like PEG to the starting sol (Figure 7.1b). Since the system is sensitive to changes in the synthesis parameters (composition of the starting sol, temperature, etc.), a reproduction of the experiment was carried out in Paper I in order to "calibrate" the system. Simply by adjusting the amount of PEG (with an average molecular weight of 35,000 g/mol) in the starting sol it was possible to alter the size of the macropores. Here, it has been shifted from 12 μm to 0.3 μm by increasing the PEG/Si molar ratio from $6.86 \cdot 10^{-4}$ to $8.69 \cdot 10^{-4}$. Further increase of PEG lead to a non-macroporous structure, while lower amounts resulted in a macroscopic phase separated structure. It is important to know how the basic system works in order to optimize the macropore size before further alterations are carried out, for instance by adding CTAB to the system.

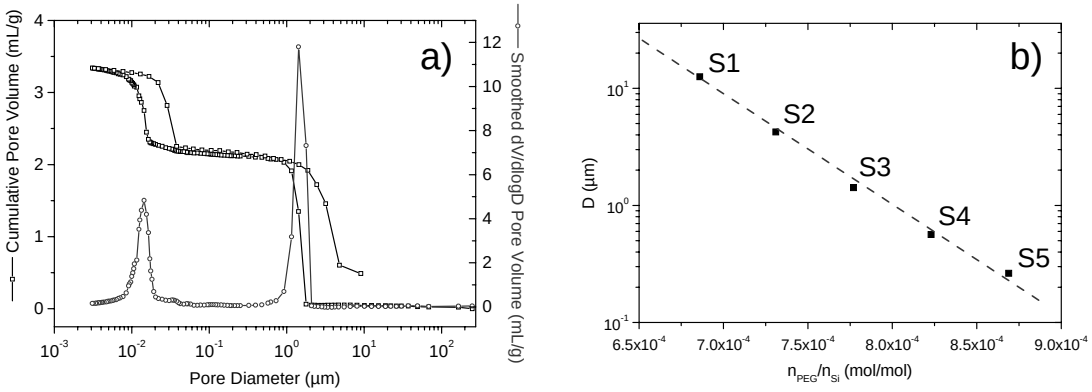

Figure 7.2. a) Pore size distribution of sample S3 determined by mercury porosimetry. The open squares (□) denote the cumulative pore volume plot (intrusion and extrusion branch), while the open circles (○) denote the smoothed d*V*/(d log *D*) pore volume plot (intrusion branch). b) Evolution of the macropore diameter as a function of the PEG/Si ratio for compositions S1−S5.

By adding a second structure directing agent, C_nTAB, to the starting sol, surfactant templated mesopores with pore diameters of about 4 nm were created and these effects will be more thoroughly discussed later. However, the addition of C_nTAB to the sol also had a large effect on the phase separation behavior and thus also the macropore structure, which could be identified by mercury porosimetry (Figure 7.3.). Starting from monoliths containing no CTAB the macropore size first increased at low addition up to a certain concentration and then started to slowly decrease at higher CTAB concentrations. The concentration that resulted in the maximum pore size was found out to coincide with the *critical micelle concentration* (cmc) for CTAB in a water/ethanol/nitric acid solution corresponding to the complete hydrolysis of TEOS in the sols. We believe that below this cmc the ionic surfactant act as a simple salt because similar effects could be observed when NaBr was added to the starting sols (causing the zeta potential to slightly increase). Then again at concentrations above the cmc we believe that CTAB start to form micelles on the silica surface that have a stabilizing effect on the system.[26,110] This effect is also influenced by the hydrophobic chain length of the surfactant in a similar way as the cmc is affected. Since $C_{14}TAB$ have a higher cmc value than $C_{18}TAB$, monoliths prepared with $C_{14}TAB$ have larger macropores compared to $C_{18}TAB$ when the same concentrations have been used. In order to not lose the macroporous structure at high CTAB

concentration the PEG amount has to be decreased, which has been done for samples S18 and S19. In this way the macropore diameter can be changed independently of the CTAB concentration.

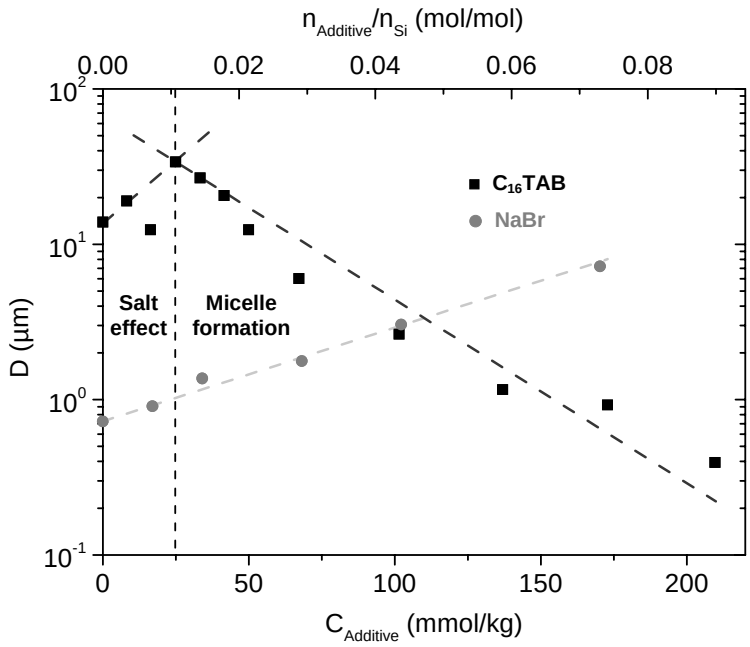

Figure 7.3. Slope of the plot of the CTAB/Si molar ratio versus ln *D* of the macropores (*compositions S6–S17*). To demonstrate the salt effect, a similar series containing NaBr instead of CTAB was added. Note: The PEG/Si ratio was increased to $8.69 \cdot 10^{-4}$ to avoid obtaining excessively large pores at high NaBr concentrations.

7.1.3. Structure Control of the Textural Mesopores

As described earlier, solvent exchange treatments in ammonia solutions has been performed in order to strengthen the gel structure to avoid excessive shrinkage or crack formation. On the other hand, this also have a remarkable effect on the structure on the nanometer scale due to the Ostwald ripening mechanism. This has been demonstrated by varying the NH_4OH concentration of the post-treatment solutions between 1.0 M and 0.01 M (Figure 7.4. and Table 7.2.). Together with the increase in size of the textural mesopores, the surface area is decreased when the ammonia concentration is increased, which suggests a coarser structure. However, a comparison of mesopore volumes can not be applied in this case, given that the measurement is

not accurate for large mesopores of ~ 20 nm (only part of the volume has been accounted for of samples S26 and S27). Moreover, changing the PEG concentration had a small effect on the textural mesopore size.

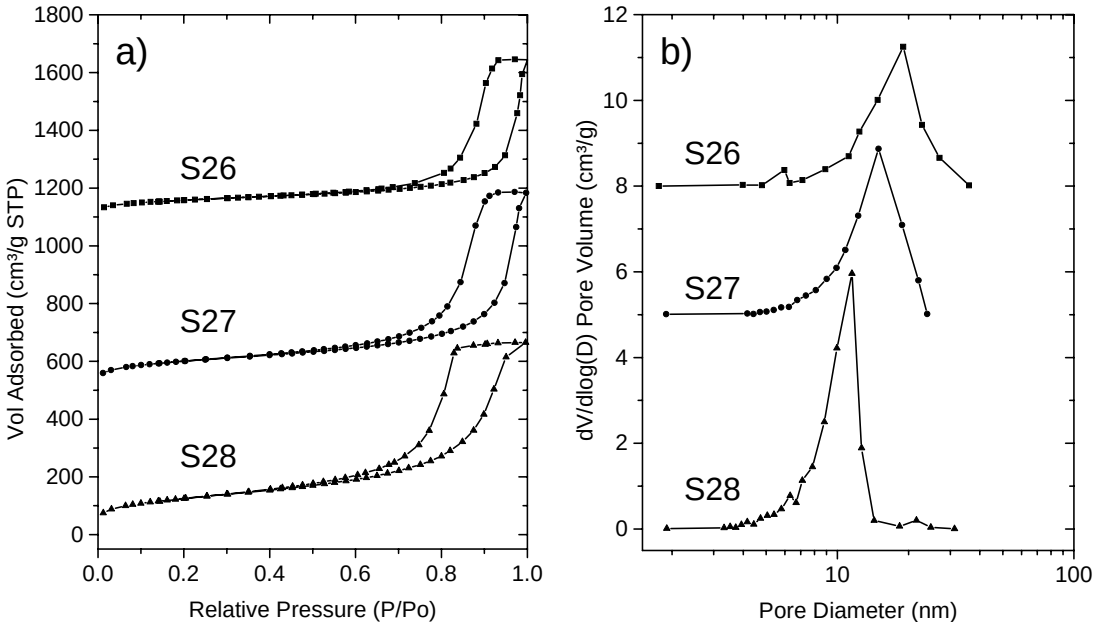

Figure 7.4. a) Nitrogen physisorption isotherms measured for SiO_2 monoliths post-treated in 1.0 M NH_4OH (S26, offset: 1100 cm^3/g), 0.1 M NH_4OH (S27, offset: 500 cm^3/g), 0.01 M NH_4OH (S28). b) Corresponding pore diameter distribution curves calculated according to the BJH desorption algorithm (offsets: S26: 8 cm^3/g and S27: 5 cm^3/g).

Table 7.2. Textural properties of silica monoliths treated with different NH_4OH concentrations determined from the N_2 sorption isotherms.

Sample	NH_4OH conc. [mol/L]	BET area [m^2/g]	Micropore area [m^2/g]	Mesopore Volume [cm^3/g]	Textural pore diameter (BJH_{des}) [nm]	Textural pore diameter (DFT_{eq}) [nm]
S26	1.0	212	23.3	0.56	17.9	~ 22
S27	0.1	350	59.6	0.87	14.7	17.0
S28	0.01	450	73.5	1.03	10.5	12.7

7.1.4. Structure Control of the Surfactant Templated Mesopores

As mentioned earlier, the addition of a cationic surfactant, C_nTAB, to the starting sol resulted in the formation of supramolecularly templated mesopores in the nanometer range as seen in the TEM image in Figure 7.1d, which could be further examined by nitrogen physisorption (Figure 7.5a.).

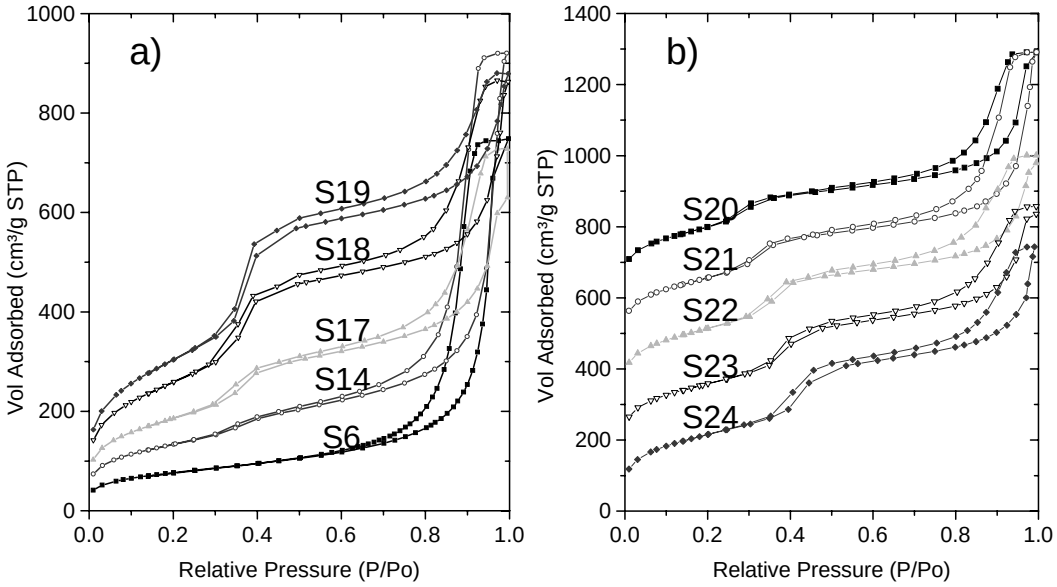

Figure 7.5. a) N2 physisorption isotherms of samples S6 (no $C_{16}TAB$), S14 (44 mmol $C_{16}TAB$), S17 (90 mmol $C_{16}TAB$), S18 (137 mmol $C_{16}TAB$), and S19 (187 mmol $C_{16}TAB$). b) $C_{14}TAB$–$C_{18}TAB$. N2 physisorption isotherms of silica monoliths synthesized in the presence of C_nTABr (n = 14, 16, 18) and 1:1 mixtures of these. The sorption isotherms are offset by 150 cm^3/g for clarity.

When increasing the CTAB concentration a steep nitrogen adsorption is observed between the relative pressures 0.3 and 0.4, implying pores of about 3 nm in diameter (determined from BJH_{des}) or about 4 nm (determined from DFT_{eq}) as indicated in Table 7.3. At the same time, the BET surface area is increased dramatically to above 1100 m^2/g for the highest CTAB concentration. The volume of the surfactant templated pores increases on the expense of the textural pore volume, but the total mesopore volume remains virtually constant. The size of the textural pores is also slightly increased and the size distribution is broadened, due to the formation of larger silica particles. Furthermore, by varying the hydrophobic chain length of the

surfactant between C_{14}TAB and C_{18}TAB the nitrogen uptake is shifted from relative pressures of about 0.25 to 0.45 P/P_0, which is illustrated in Figure 7.5b. Calculations based on the DFT method specifies that the pore size is swelled from 3.6 nm to 4.6 nm, which suggests that this pore size region is actually a result of supramolecular templating (Table 7.3). Due to a lower cmc value for surfactants with longer hydrophobic chain lengths, the C_{18}TAB has the highest V_{surf} and the lowest V_{text} similar to an increase of the CTAB concentration. Furthermore, the C_{18}TAB micelles give rise to the largest pore diameter, which also contributes to the increase of V_{surf}. No long-range order of the mesopores was detected by XRD in any of the prepared monoliths. However, recent studies claim that long-range ordering is possible by using block copolymers as structure directing agents[43,111,112] or by using glycol-modified silanes as silica source[113] in the synthesis of similar hierarchically porous monoliths.

Table 7.3. Properties of silica monoliths containing different C_nTAB amounts and chain lengths determined from the N_2 sorption isotherms.

Sample	C_nTAB/ Si	n	BET area [m^2/g]	V_{text}[1] [cm^3/g]	V_{surf}[2] [cm^3/g]	D_{macro}[3] [µm]	D_{text}[3] [nm]	D_{surf}[4] [nm]	D_{surf}[5] [nm]
S6	0	16	276	1.40	0.18	13.9	14.5	-	-
S14	0.044	16	484	1.13	0.34	2.64	14.4	2.83	4.03
S17	0.090	16	672	0.99	0.50	0.394	18.3	2.91	4.05
S18	0.137	16	939	0.78	0.73	3.31	17.8	2.92	4.01
S19	0.187	16	1106	0.57	0.91	0.344	N.A.	2.95	4.11
S20	0.105	14	723	1.15	0.49	24.1	16.4	2.55	3.59
S21	0.105*	14/16	749	1.09	0.55	18.8	17.2	2.74	3.81
S22	0.105	16	776	0.79	0.59	7.13	20.2	2.89	4.04
S23	0.105*	16/18	756	0.86	0.60	2.21	19.8	3.03	4.29
S24	0.105	18	782	0.72	0.65	0.708	20.0	3.21	4.55

* 1:1 molar amount of C_{14}TAB/C_{16}TAB and C_{16}TAB/C_{18}TAB.
[1] Determined from the cumulative mercury intrusion plot (d < 50 nm).
[2] Determined from the nitrogen adsorption isotherm (P/Po < 0.6).
[3] Approximately determined from the mercury intrusion plot.
[4] Approximately determined from the BJH_{des} plot.
[5] Approximately determined from the DFT equilibrium model.

7.1.5. Comments on the Formation of the Surfactant Templated Pores

In Paper I it was not clearly stated if the surfactant templated mesopores are formed at the instant of the sol-gel transition or if they are formed at a later stage in the process. However, preparing new monoliths containing a high concentration of CTAB (the same composition as sample S18), but using different solvent exchange treatments sheds new light on the formation mechanism. After normal drying and calcining procedures of the monoliths, nitrogen physisorption isotherms were measured and plotted together with the calculated DFT pore size distributions in Figure 7.6.

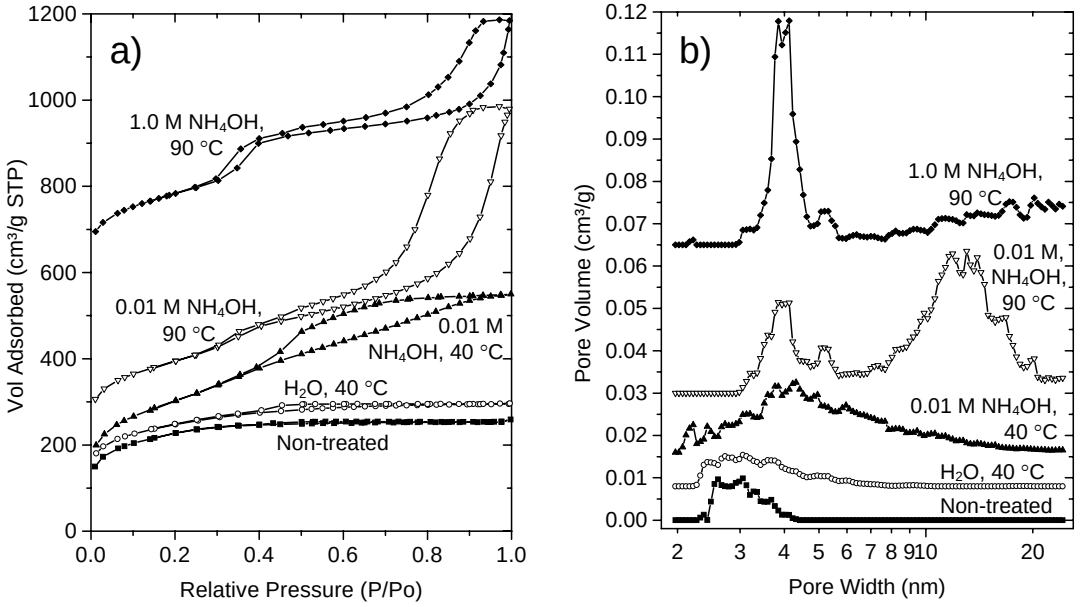

Figure 7.6. Effect of the post treatments on the surfactant templated mesopores: a) Nitrogen sorption isotherms: (■) Non-treated; (○) H_2O, 40 °C (offset: 50 cm^3/g)); (▲) 0.01 M NH_4OH, 40 °C (offset: 50 cm^3/g); (▽) 0.01 M NH_4OH, 90 °C (offset: 190 cm^3/g); (◆) 1.0 M NH_4OH, 90 °C (offset: 580 cm^3/g). b) DFT calculations of the pore size distribution: Offsets: (■) -, (○) 0.008 cm^3/g, (▲) 0.016 cm^3/g, (▽) 0.030 cm^3/g, and (◆) 0.065 cm^3/g.

The non-treated monoliths exhibit only small mesopores and micropores, which can be ascribed to a combination of textural porosity between silica particles and surfactant templated pores. One has to keep in mind that these monoliths have been dried and calcined before the nitrogen sorption isotherms were detected, leading to

differences in the shrinkage of the monoliths that also affects the results. As the solvent exchange treatments get more severe, the mesopore volume is increased and shifted towards larger sizes. Simultaneously, the surfactant templated pore region (at approximately 4 nm in diameter) becomes separated from the textural pore region at more harsh treatment conditions than 0.01 M NH_4OH at 40 °C. Thus, the new experiments prove that solvent exchange treatments in ammonia are required to produce the mesoporous structure. A plausible explanation would be that the surfactant micelles are initially "trapped" in the silica gel after the sol-gel transition. Then, by increasing the solubility of the gel by adjusting the pH and the temperature, dissolution and re-precipitation reactions lead to rearrangement of the micelles into an interconnected pore structure. Further increase of the solubility of silica by post-treatments in NaOH solutions (pH > 12) resulted in an ordered hexagonal pore structure similar as reported by Martin *et al*. However, this severe treatment also lead to the collapse of the macroscopic structure of the monolith. Then again, adding CTAB only to the solvent exchange solution was not sufficient to prepare similar structures, but lead to the formation of a mesoporous outer layer of the monolith, while the core was still free of surfactant templated pores.

7.1.6. Surface Chemistry of the Silica Monoliths

As pointed out earlier, the organic portion of the synthesized monoliths could be fully removed either thermally by calcination or chemically by sulfuric acid treatments (Paper II). To determine the difference these treatments have on the silica surfaces, the monoliths C' (H_2SO_4 treatment) and D' (calcination) have both been grafted with trimethylchlorosilane (TMCS) and octadecyldimethylchlorosilane (ODMCS). The degree of functionalization has been detected by ^{29}Si MAS NMR and FT-IR (visualized in Figures 7.7. and 7.8.). The appearance of a new line centered at about 13.0 ppm (M) in the ^{29}Si NMR spectra indicates the anchored trimethylsilyl (TMS) species. The intensities of the M groups are about 4% and 2% of those of the Q^n lines for C'-TM and D'-TM, respectively. Furthermore, FT-IR suggests that C'-OMD has a larger amount of anchored ODMS groups than D'-OMD. Also these results indicate that treatments in H_2SO_4 lead to a larger amount of surface silanol groups than the calcined monoliths, which is beneficial for further surface functionalization.

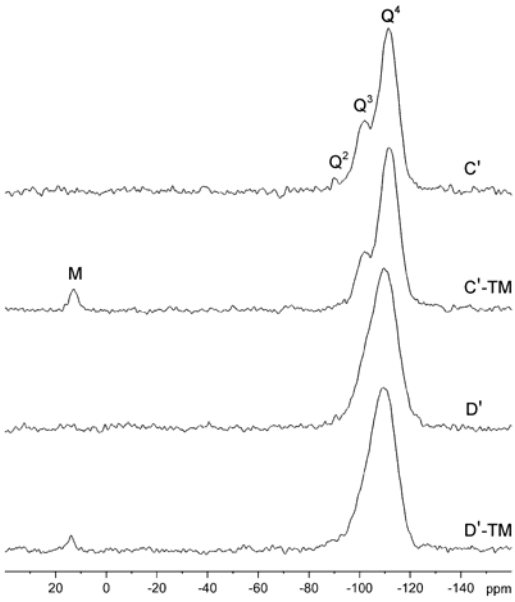

Figure 7.7. ^{29}Si MAS NMR spectra of silica monoliths C' and D' before and after functionalization with TMCS.

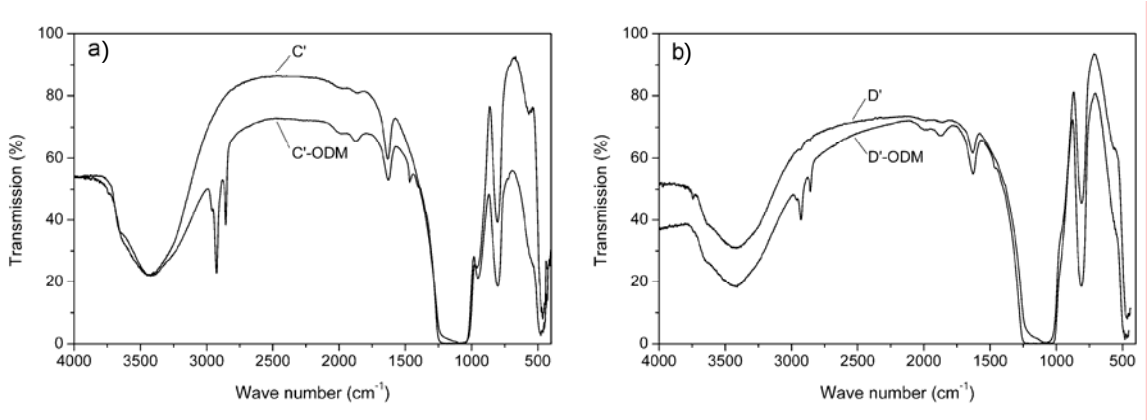

Figure 7.8. FT-IR spectra of a) C' and b) D' before and after functionalization with ODMCS.

7.2. Hierarchically Porous Carbon Monoliths through Nanocasting

As can be seen in Figure 7.9, by using hierarchically porous silica monoliths as molds it has been possible to prepare carbon monoliths with similar hierarchically porous structures by nanocasting techniques (Papers III–V). Depending on the studied length scale the carbon replica is either a positive or a negative of the original silica monolith. It is also possible to alter the carbon structure on each different length scales either by changing the silica mold or by diluting the carbon precursor, which will be discussed in more details in the following chapters. Furthermore, it was also found out that some of the carbon monoliths contained micropores.

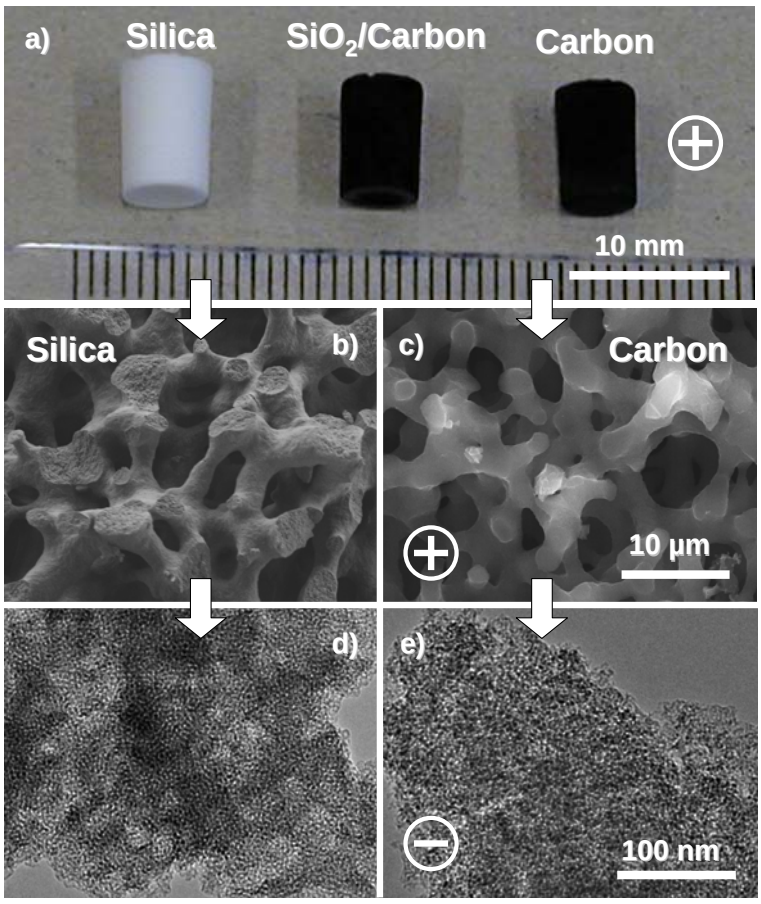

Figure 7.9. Comparison of the starting silica monolith and the carbon replica on different length scales. a) Photograph of the macroscopic morphology, b) SEM images of the silica and c) the carbon macropores, d) TEM images of the silica and e) the carbon mesopores. (+) indicates that the carbon structure is a positive replica on a particular length scale, while (–) indicates a negative replica.

7.2.1. Replication of the Macroscopic Morphology

As illustrated in Figure 7.9a. the silica/carbon composite and the carbon replica keeps the same size and shape as the starting silica mold. However, a slight shrinkage of the diameter can be observed for the silica/carbon composite and the carbon replica compared to the starting silica monolith due to some sintering of the silica framework during the carbonization step. Nonetheless, it is easy to control the macroscopic structure of the carbon monoliths simply by adjusting the size and shape of the silica mold. One can say that it is a positive replica of the silica structure on this particular length scale.

7.2.2. Replication of the Macropore Structure

The carbon structure is also a positive replica of the silica monoliths on the micrometer length-scale, which is apparent from the comparison of Figures 7.9b. and 7.9c. Since the carbon macropores retain approximately the same size, the macropores are easy to adjust simply by changing the pore size of the starting silica monoliths as discussed in the preceding chapters. The reason why the macropores are not filled must be a result of the low polymerization degree in the macropores and preferential loading of the mesopores. In experiments where no oxalic acid had been used as catalyst, the low degree of polymerization in the macropores resulted in the evaporation of unreacted polymers during the carbonization step, which could be detected as a greater mass loss than expected. Generally, lower polymerization temperatures are needed in confined spaces, which would explain the greater polymerization degree inside the mesopores. On the other hand, if oxalic acid was used as a catalyst, another way to restrict the loading is by changing the furfuryl alcohol (FA) concentration by dilution with TMB. At lower concentrations the carbon macropores are for the most part empty, while at higher concentration a more considerable portion of the pores are filled with carbon (Figure 7.10.). The same effect can be observed from the mercury porosimetry measurements in Figure 7.11. Here, the peak between 1 and 2 μm clearly decreases upon increasing the FA concentration from 40 to 100 vol %. However, some of the reduction can also be attributed to the total mass gain of the monoliths upon loading with carbon. Only a small shift in the pore diameter can be observed for some of the samples, however not

as much as would be expected if the carbon would be homogeneously distributed along the side of the walls of the silica macropores.

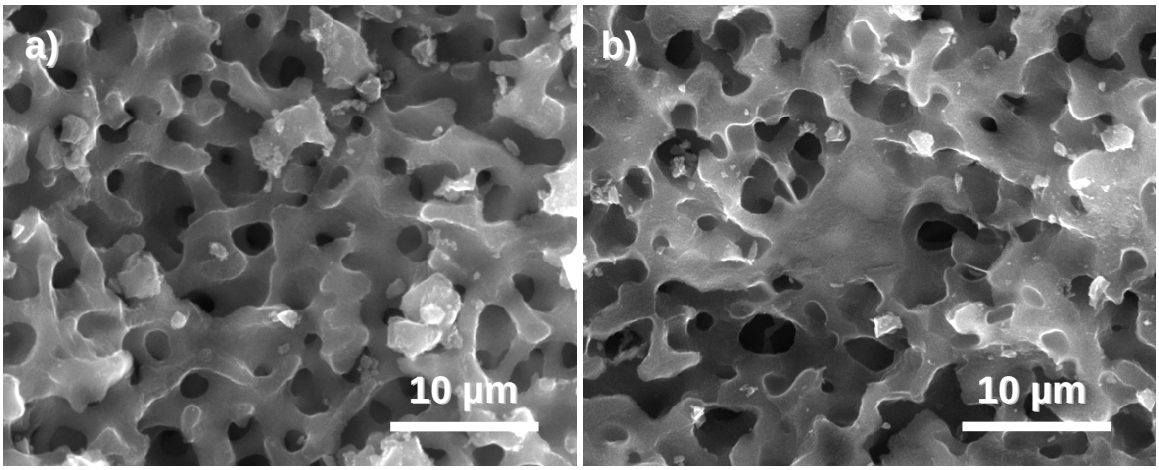

Figure 7.10. SEM images of a) C6 (40 vol % FA) and b) C9 monoliths (100 vol % FA).

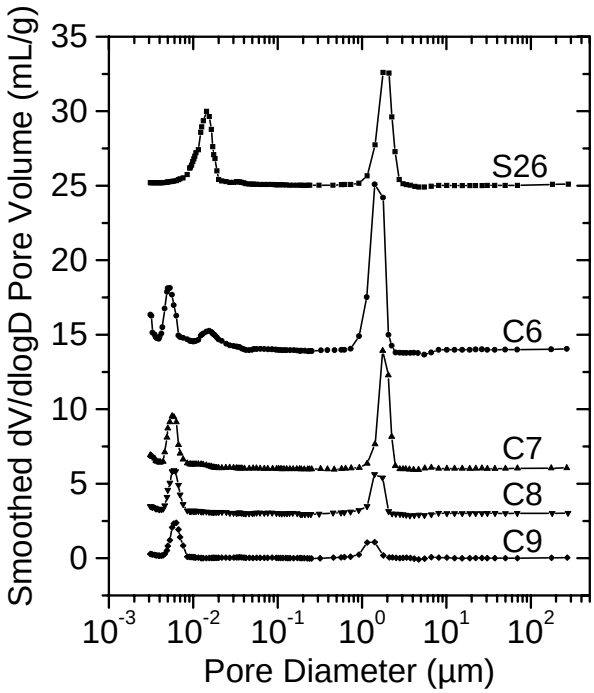

Figure 7.11. Differential pore diameter distribution of SiO_2 and carbon monoliths as determined by mercury porosimetry (intrusion) measurements. Offsets: S26: 25 cm^3/g, C6: 14 cm^3/g, C7: 6 cm^3/g, C8: 3 cm^3/g.

7.2.3. Replication of the Mesopore Structure

In the nanometer range the carbon replica is a negative replica of the silica monoliths (Figure 7.9e.). There are several ways to tailor the structure on this level, which are schematically illustrated in Figure 7.12. The most straightforward way to alter the pore size is to use silica monoliths with different mesopore structures, e.g. by altering the post-treatment conditions (a) or by increasing the CTAB concentration in the sol (c). In addition, dilution of the carbon precursor results in interesting bimodal mesopore structures (b and d).

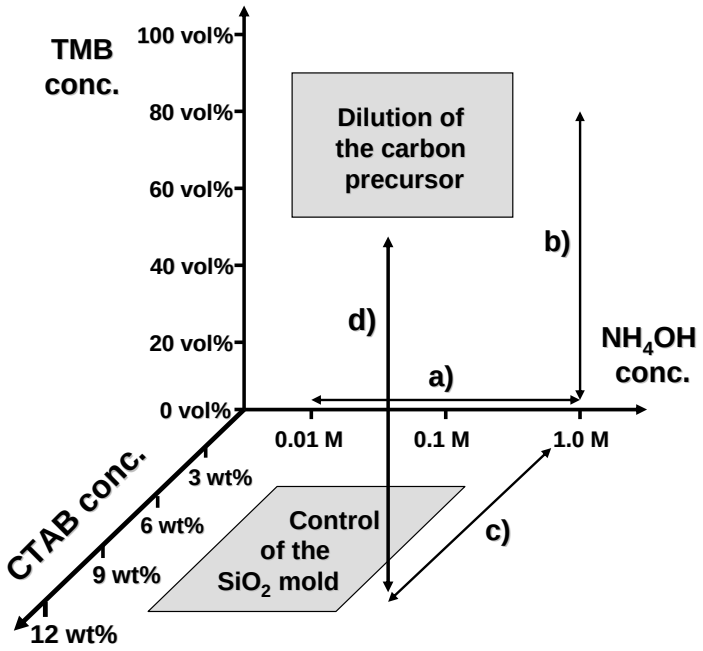

Figure 7.12. Structure control of the carbon mesopores by altering the starting silica mold either by solvent exchange treatments (a) or adding CTAB to the sol (c). Further modifications can be done by dilution of the carbon precursor with TMB (b) and (d).

Table 7.4. Nitrogen sorption properties for the silica/carbon composites and the carbon replicas (for synthesis details refer to Table 6.2.).

Sample	FA [vol %]	Surface Area: BET [m^2/g]	Surface Area: μ pore [m^2/g]	Mesopore Volume [cm^3/g]	Micropore Volume [cm^3/g]	Pore Sizes [nm]: Silica templated	Pore Sizes [nm]: Textural pores
SC1	40	332	199	0.35	0.092	-	16.1 [a]
SC2	40	363	210	0.45	0.097	-	12.6 [a]
SC3	40	419	236	0.39	0.109	-	7.6 [a]
SC4	20	267	136	0.36	0.063	-	16.5 [a]
SC5	30	301	171	0.36	0.079	-	16.8 [a]
SC6	40	337	184	0.35	0.085	-	16.1 [a]
SC7	60	351	199	0.29	0.092	-	-
SC8	80	327	211	0.26	0.098	-	-
SC9	100	342	246	0.20	0.114	-	-
SC16	10	596	337	0.42	0.153	-	15.3 [a]
SC17	20	417	295	0.39	0.170	-	15.9 [a]
SC18	30	346	240	0.28	0.111	-	-
SC19	40	361	248	0.24	0.115	-	-
SC20	60	291	196	0.19	0.091	-	-
C1	40	1332	424	2.71	0.191	7.4 [a]	17.5 [a]
C2	40	1045	282	1.64	0.125	5.2	12.2 [a]
C3	40	1510	249	2.21	0.104	4.1	8.0 [a]
C4	20	1456	316	4.25	0.138	7.4 [a]	18.6 [a]
C5	30	1362	379	2.64	0.170	7.4 [a]	17.2 [a]
C6	40	1493	460	2.71	0.208	7.4 [a]	17.5 [a]
C7	60	978	376	1.40	0.172	7.7 [a]	-
C8	80	994	432	1.36	0.198	7.6 [a]	-
C9	100	604	335	0.67	0.155	8.3 [a]	-
C10	40	1493	460	2.71	0.208	14.3 [b]	17.5 [a]
C11	40	1015	205	1.41	0.088	7.6 [b]	-
C12	40	766	195	0.82	0.086	6.0 [b]	-
C13	40	831	122	0.82	0.049	4.2 [b]	-
C14	40	1297	43	1.19	0.007	2.9 [b]	-
C15	40	1123	0	0.74	0.000	2.4 [b]	-
C17	20	1854	48	1.54	0.000	2.7 [b]	16.7 [a]
C18	30	1723	16	1.48	0.000	2.7 [b]	16.7 [a]
C19	40	1297	43	1.19	0.007	2.9 [b]	-
C20	60	846	58	0.69	0.019	2.9 [b]	-

[a] Approximately determined from the BJH_{des} plot.
[b] Approximately determined from the BJH_{ads} plot.

a) Using Silica Monoliths with Different Textural Mesopore Sizes as Molds (C1–C3)

As previously described, it is possible to modify the textural mesopore size of the starting silica monoliths by applying post-treatments with different ammonia concentrations. When these monoliths are to be used in the nanocasting process different carbon structures are obtained (Paper III). Nitrogen physisorption isotherms of these replicas are represented in Figure 7.13. Here, the carbon sample C1 has been nanocast from silica monoliths treated with 1.0 M NH_4OH (the standard post-treatment method) and exhibits a sharp two-step nitrogen uptake in the relative pressure ranges between 0.8 and 0.9 P/P_0 and between 0.9 and 1.0 P/P_0. This further indicates that the monolith has a bimodal mesopore size distribution. When the pore size of the silica is decreased also the two pore size regions of the carbon replica are decreased as can be seen for samples C2 and C3. The closing of the hysteresis loop at ~ 0.42 P/P_0 is caused by the collapse of the meniscus and does not indicate the presence of a third pore size region.

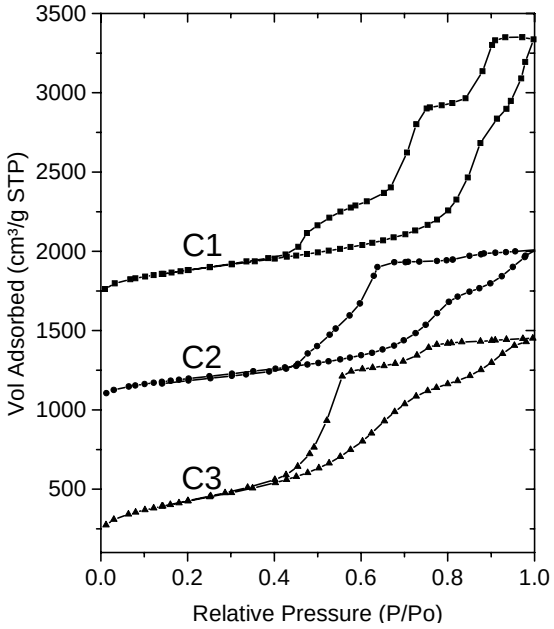

Figure 7.13. Nitrogen physisorption isotherms measured for carbon monoliths prepared from precursor solutions containing 40 vol % FA. SiO_2 monoliths post treated in 1 M NH_4OH (C1, offset: 1500 cm^3/g), 0.1 M NH_4OH (C2, offset: 900 cm^3/g), and 0.01 M NH_4OH (C3) were used as scaffolds.

b) Using Silica Monoliths with a Bimodal Pore System as Molds and Varying the FA Concentration (C4–C9)

In Paper III, nitrogen physisorption has been utilized to determine how the FA concentration affects the replica structure when silica monoliths with a single mesopore size region are used as molds (Figure 7.14.). From the composite isotherms plotted in (a) a sharp nitrogen uptake at $P/P_0 \sim 0.9$ indicates that low FA concentrations (SC4–SC6) are not sufficient to completely fill the textural porosity of the silica monolith. However, by increasing the FA concentration the pores are gradually filled and simultaneously, very broad hystereses appear in the isotherms, which suggests that the pores are partially blocked by carbon. Furthermore, when the silica part has been removed (b) we can see that the remaining textural porosity from the composites is still left in the replicas. In addition, a second nitrogen uptake has appeared between 0.8 and 0.9 P/P_0, and since there is no visible shift of the pore size when the FA concentration is increased we believe that these pores are templated by the silica particles. Similar silica wall templated mesopores have also been reported by the group of Feng.[114] Thus, by varying the FA concentration it is possible to obtain either a monomodal or bimodal pore size distribution and to control the ratio between these. The results are confirmed by the mercury porosimetry results in Figure 7.11. Here, the textural porosity can only be detected for the silica monolith and sample C6, while silica templated pores are observed for all carbon samples. Moreover, exceptionally high mesopore volumes could be detected for the carbon replicas (4.25 cm^3/g for sample C4).

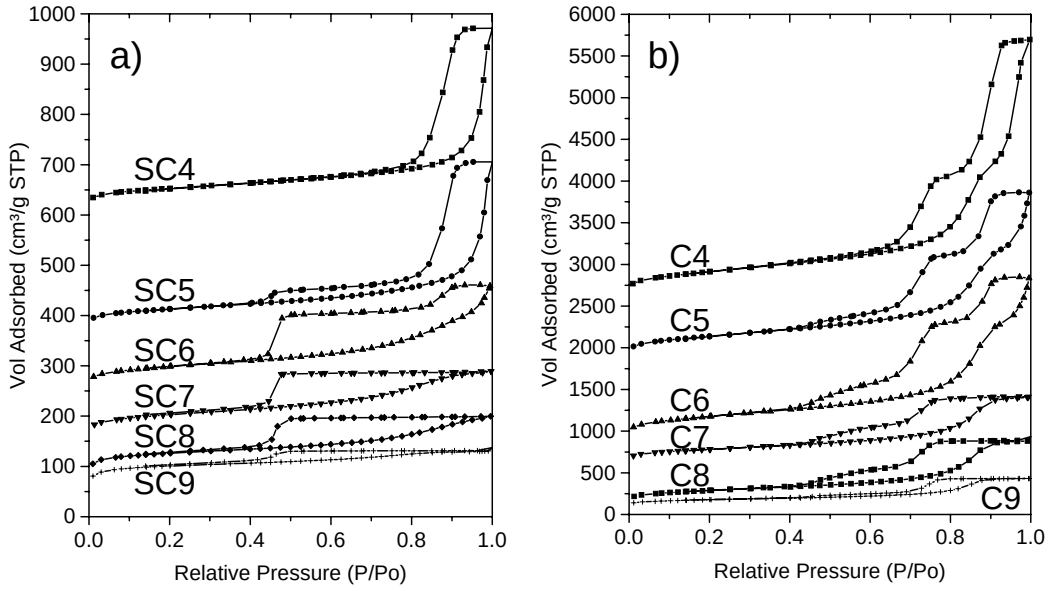

Figure 7.14. Nitrogen physisorption isotherms measured for a) SiO_2-carbon composite monoliths and b) carbon replicas prepared from precursor solutions with different FA/TMB ratios. Offsets; SC4: 575 cm^3/g, SC5: 325 cm^3/g, SC6: 200 cm^3/g, SC7: 100 cm^3/g, SC8: 30 cm^3/g, C4: 2500 cm^3/g, C5: 1750 cm^3/g, C6: 750 cm^3/g, and C7: 500 cm^3/g.

c) Using Silica Monoliths with Different CTAB Concentrations as Molds (C10–C15)

Another way of controlling the mesopore size of the replica is to use silica monoliths prepared from sols containing different CTAB concentrations as molds. Figure 7.15. demonstrates how the pore size depends on the amount of CTAB used in the synthesis of the SiO_2 monoliths, while the textural properties determined by nitrogen sorption measurements are summarized in Table 7.4. It is evident that the mesopore size can be decreased by increasing the amount of CTAB. However, at the same time the pore size distribution is somewhat broadened and the mesopore volume is decreased. As was stated earlier for the silica monoliths, adding more CTAB to the sol resulted in increasingly porous particles, meaning more volume to fill. Since the carbon monoliths are negative replicas of the silica structure at this length scale it is also obvious that the mesopore volume of the carbon replicas will decrease. Thus, this is also a straightforward means to determine the SiO_2 wall thickness.

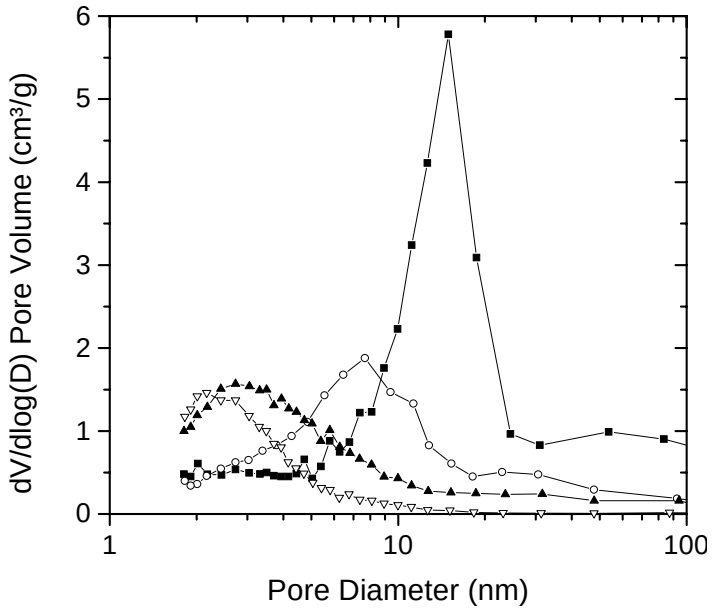

Figure 7.15. Pore size distribution determined by the BJH method (adsorption branch) for carbon monoliths prepared from silica monoliths containing different amounts of C_{16}TAB: (■) C10 (no CTAB), (○) C11 (3 wt % CTAB), (▲) C14 (9 wt % CTAB), and (▽) C15 (12 wt % CTAB).

d) Using Silica Monoliths with a Trimodal Pore System as Molds and Varying the FA Concentration (C16–C20)

Finally, the mesopore size of the carbon replica can be controlled by using silica monoliths with a bimodal mesopore system as templates and varying the FA concentration in a similar fashion as for the monomodal monoliths, which has been studied in Paper V. An immediate "filling" of the surfactant templated pores can be seen in Figure 7.16a. when going from the silica monolith (S30) to the composite prepared from the 10 vol % FA solution (SC16) (the disappearance of the N_2 uptake at ~ 0.35 P/P_0). After this also the textural pores (~ 0.95 P/P_0) are gradually getting filled and a pronounced hysteresis appears. From Table 7.4. one can notice that the increase in the FA concentration is also accompanied by a reduction of the surface area as well as the total mesopore volume due to the filling of the pores and the increase of the mass. From the isotherms of the replicas in Figure 7.16b. it is evident that the composites that contained textural porosity resulted in carbon replicas containing the same textural porosity. At a first glance these replicas do not seem to contain any

silica templated mesopores, since no sharp nitrogen uptake is visible. The composite and the carbon replica prepared from the 20 vol % FA solution have been plotted in the same chart in Figure 7.17. Here, the mass contribution for the silica part has been removed to allow an easier comparison of the two samples. Above the relative pressure ~ 0.6 P/P_0 the isotherms are almost identical, demonstrating that the textural porosity and the hysteresis are similar for both of the samples. On the other hand, for the replica a broad N_2 uptake range can be observed between 0.05 and 0.6 P/P_0, indicating the same broad pore size distribution around 2.7 nm as seen for sample C14 in Figure 7.15. In addition, a surprising observation is that the microporosity in the replica (< 0.05 P/P_0) has remarkably decreased as well after removing the silica part.

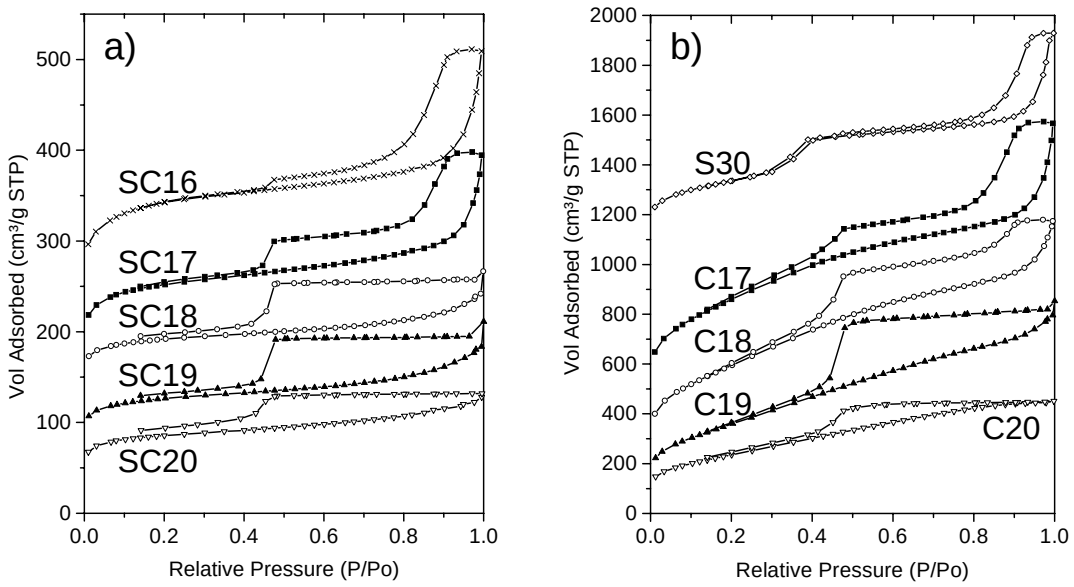

Figure 7.16. Nitrogen sorption isotherms measured a) for carbon-silica composite monoliths, impregnated with different amounts of furfuryl alcohol, after pyrolysis at 850 °C (SC16–20) b) for the parent silica monolith (S30) and nanocast carbon monoliths (C17–20) after removal of the silica scaffold. Offsets: SC16: 170 cm^3/g, SC17: 90 cm^3/g, SC18: 90 cm^3/g, SC19: 20 cm^3/g, S30: 1100 cm^3/g, C17: 350 cm^3/g, and C18: 120 cm^3/g.

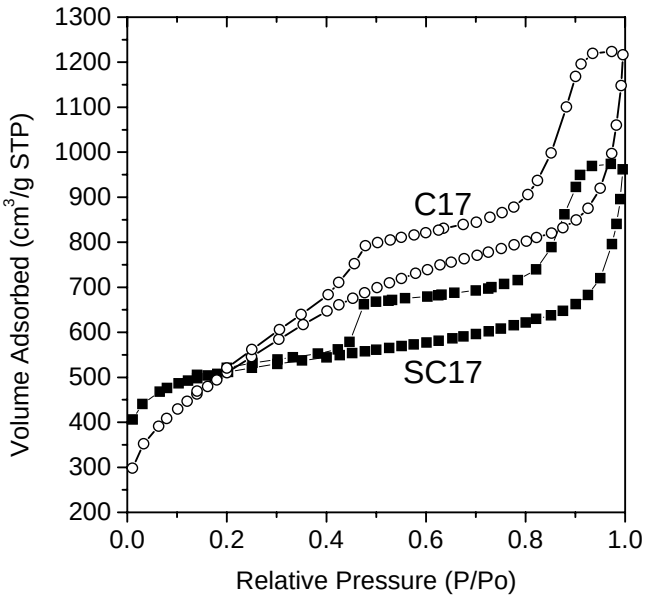

Figure 7.17. Comparison of the isotherms of the composite (■) SC17 and the replica (○) C17 (20 vol % FA), where the isotherm for SC17 has been adjusted for the different mass of the monoliths (mass ratio, $m_{CM}/m_{SCM} = 3.16$) for easier comparison.

e) Summary

By changing the pore size and/or the number of mesopore size regions in the starting silica monoliths, the mesopore size of the carbon replicas can be controlled. Since the carbon structure is a negative replica of the silica structure, the mesopore wall size and shape will determine the pore size and shape of the carbon monoliths. Moreover, an additional distinct mesopore size region can be induced in the carbon replica by dilution of the carbon precursor. An incomplete filling of the textural mesopores leads to a positive replica of this specific porosity. Thus, the ratio between the textural pore volume and the volume of the silica templated pores in the carbon monoliths can be adjusted by the carbon precursor concentration.

7.2.4. Microporosity

From Table 7.4. it is clear that some of the composites and the replicas contain substantial amounts of micropores, as determined from the nitrogen sorption *t-plots*. Depending on the type of silica monoliths used as molds different explanations are

required for the formation of this microporosity. Starting from monoliths containing only textural pores the micropore volume is dramatically increased at higher FA concentrations (SC4–SC9), especially if the total mass increase is taken into consideration. The carbon replicas still contain a large fraction of microporosity after the silica part has been removed (C4–C9). Our hypothesis is that the textural pores are large enough that the carbon structure formed inside the mesopores and also in the macropores is of an amorphous character, which normally is microporous.[115] The significant hysteresis at higher relative pressures suggests that the textural porosity is connected to the micropores. When silica monoliths having a bimodal mesoporosity are used in the nanocasting process, the micropore volume is very high already at low FA concentrations and slightly decreases upon further increase (SC16–SC20). The largest difference appears when the silica part is removed, where no microporosity can be detected for carbon replicas synthesized with low FA concentrations (C17–C18). However, there is a hint that the micropore volume is reappearing at higher FA concentrations (C19–C20). We believe in this case that the microporosity observed in the composites arises from incomplete filling of the surfactant templated mesopores which subsequently disappears upon the removal of the silica portion. The carbon structure inside these pores will also have a more dense structure due to the confinement, leading to almost nonexistent internal microporosity. When higher FA concentrations are used also the textural pores are starting to get filled and eventually also the macropores. The more amorphous (microporous) carbon structure can be observed as well. The microporosity of the replicas is clearly related to the amount of CTAB in the synthesis of the starting silica molds as seen for samples C10–C15. Hence, by altering the CTAB amount, the microporous portion of the carbon replicas can be controlled.

7.3. Hierarchically Porous Metal Oxide Monoliths through Nanocasting

A wide variety of metal oxide monoliths have successfully been prepared by the nanocasting route, including Co_3O_4, SnO_2, MnO_2, and Mn_2O_3 monoliths (Papers VI and VII). The structure of these metal oxide monoliths strongly resembles the hierarchical structures observed for the carbon monoliths discussed in the previous chapters as can be seen in Figure 7.18. However, the metal oxide replicas display very different textures of the macroporous walls (c) as compared to both silica and carbon and their smallest building blocks are crystalline particles of varying size depending on the oxide (e). Similar as for the carbon system it was found out to be a straightforward task to adjust the different pore size regions.

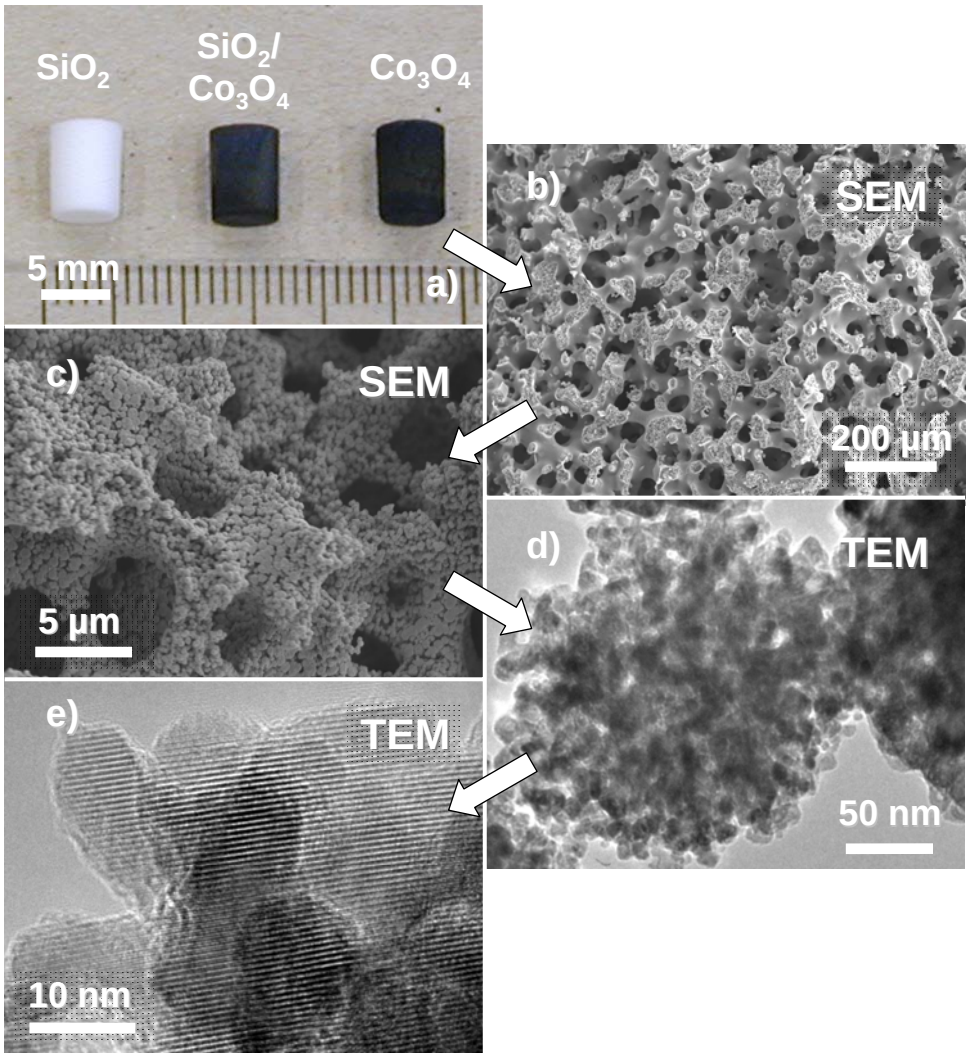

Figure 7.18. Hierarchical structure of the cobalt oxide replica.

7.3.1. Replication of the Macroscopic Morphology

Figure 7.19. gives examples of metal oxide monoliths replicated from silica and as can be seen almost no shrinkage can be detected. Unlike the carbonization at 850 °C when preparing the carbon monoliths, the metal oxides are only calcined at maximum 550 °C (where all metal salts have decomposed to oxides according to Figure 7.20.) and no further contraction of the silica scaffold should occur at this temperature. During the calcination of the composites the metal oxide structures grow rigid and can withstand the capillary pressures accompanying drying after the removal of the silica phase. However, this is not always the case. Due to the low concentration of the metal salts compared to the pure furfuryl alcohol liquid in the preparation of carbon replicas it is necessary to repeat the impregnation step 2–4 times depending on the used salt.

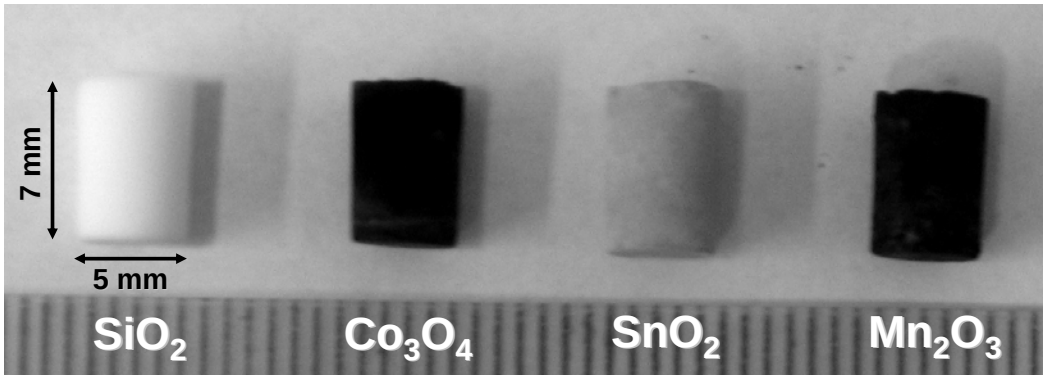

Figure 7.19. Photograph of the parent SiO_2 monolith together with the Co_3O_4, SnO_2 and Mn_2O_3 replicas (scale bar in millimeters).

Furthermore, the temperature treatments of the impregnated monoliths are of great importance for the final structure. All of the successfully prepared monoliths have been treated directly at 150 °C in order to remove the solvent from the impregnated silica monoliths. If lower temperatures (< 70 °C) have been used crack formation in the silica monoliths have often been observed, which is associated with the formation of large crystals in the mesopores. Drying at higher temperatures again lead to the diffusion of the salt molecules from the interior to the outer part of the monoliths, which after the removal of the silica part lead to unstable, hollow monoliths. 150 °C

was also sufficient to decompose most of the nitrate salts to oxides, while a temperature of 250 °C was needed to decompose the $SnCl_2$ salt. These temperatures are all related to the TG/DTA results seen in Figure 7.20. As will be discussed later, the final crystalline phases of the samples calcined at 550 °C are Co_3O_4, SnO_2 and Mn_2O_3, but when $Mn(NO_3)_2$ is calcined at only 300 °C the MnO_2 phase is formed. The phase conversion from MnO_2 to Mn_2O_3 can also be detected as a small mass loss in the TG plot at ~ 580 °C.

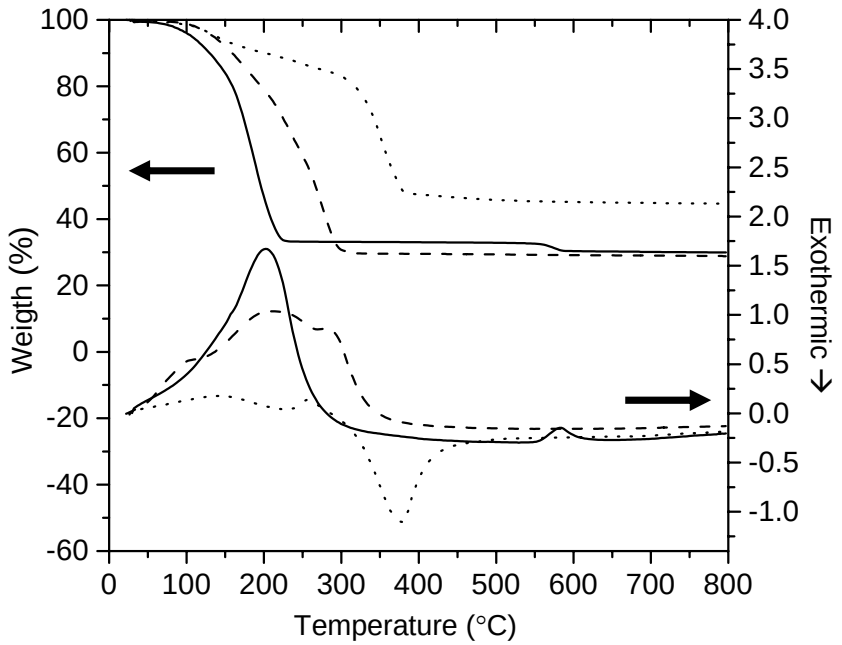

Figure 7.20. TGA and DTA of dried impregnated monoliths: $Co(NO_3)_2{\cdot}6H_2O$ (dashed), $SnCl_2{\cdot}2H_2O$ (dotted), and $Mn(NO_3)_2{\cdot}4H_2O$ (solid). Due to the different metal oxide loading amounts the weight contribution from the silica part has been removed.

7.3.2. Replication of the Macropore Structure

Similarly as for the carbon monoliths it is easy to control the macropore size of the metal oxide replicas simply by changing the pore size of the starting silica monoliths according to the methods described in Chapter 7.1. Figure 7.21. is an example where two silica samples with different macropore size have been used as molds for the preparation of tin oxide replicas. It is evident that most of the tin oxide was located in

the mesopores of the silica monoliths before the removal of the silica part and thus a positive replica of the macropore structure is formed.

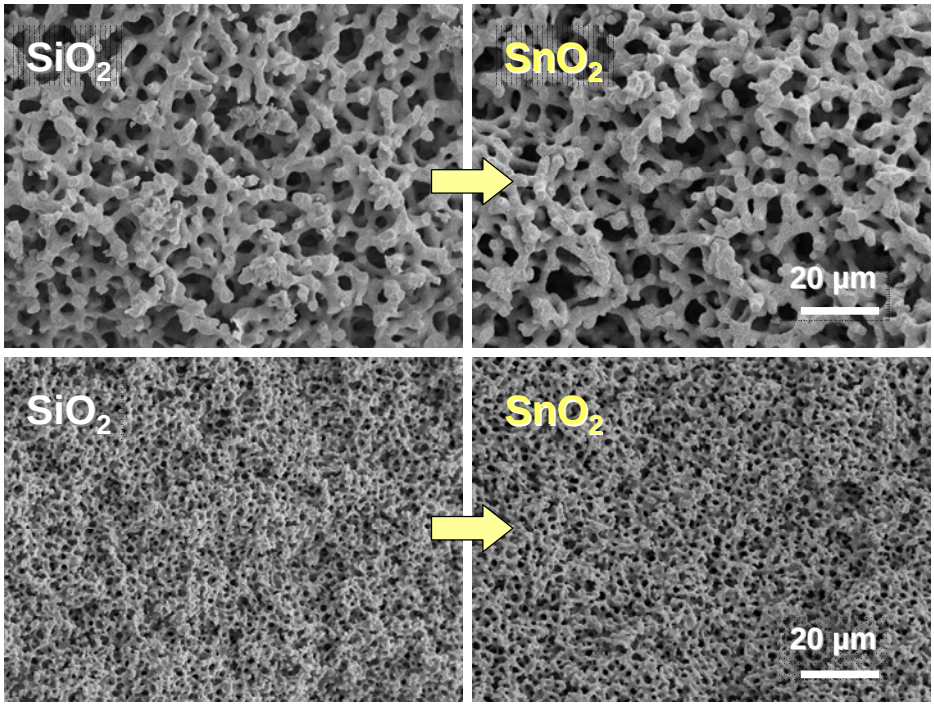

Figure 7.21. Replication of the macropore structure of two silica monoliths with different macropore sizes.

7.3.3. Replication of the Macropore Wall Structure

Even if the macropores are close to 1:1 replicas of the silica structure, the macropore wall structure is significantly different for each metal oxide as seen in Figure 7.22. The silica monoliths have relatively smooth walls, which can also be observed for the tin oxide monoliths (b). However, for the cobalt oxide (a) and manganese oxide (c) replicas a coarser macropore wall structure can be seen. The Co_3O_4 replica consists of large spherical aggregates of particles (~ 150 nm), while the Mn_2O_3 replica has slightly smaller aggregates. The size of these aggregates is controlled by several factors, including the respective relative nucleation and growth kinetics, the number of impregnation/decomposition cycles and the drying/decomposition temperature. Moreover, an additional crucial factor in the preparation of the manganese oxide replicas is the concentration of the metal salt solution. Figure 7.22. (c) shows an SEM

image of a sample prepared with a low $Mn(NO_3)_2$ concentration. The macropores are mainly free of material (flakes of "bulk" manganese oxide can be observed at the surface) and most of the metal oxide is located inside the macropore walls (positive replica). Then again, at high concentrations (d) the Mn_2O_3 crystals have grown too large to be able to enter the mesopores and are located in the macropores (denoted A), while (B) shows where the silica pore walls have been. These monoliths also have remarkably lower surface areas since no replication of the mesopores have occurred.

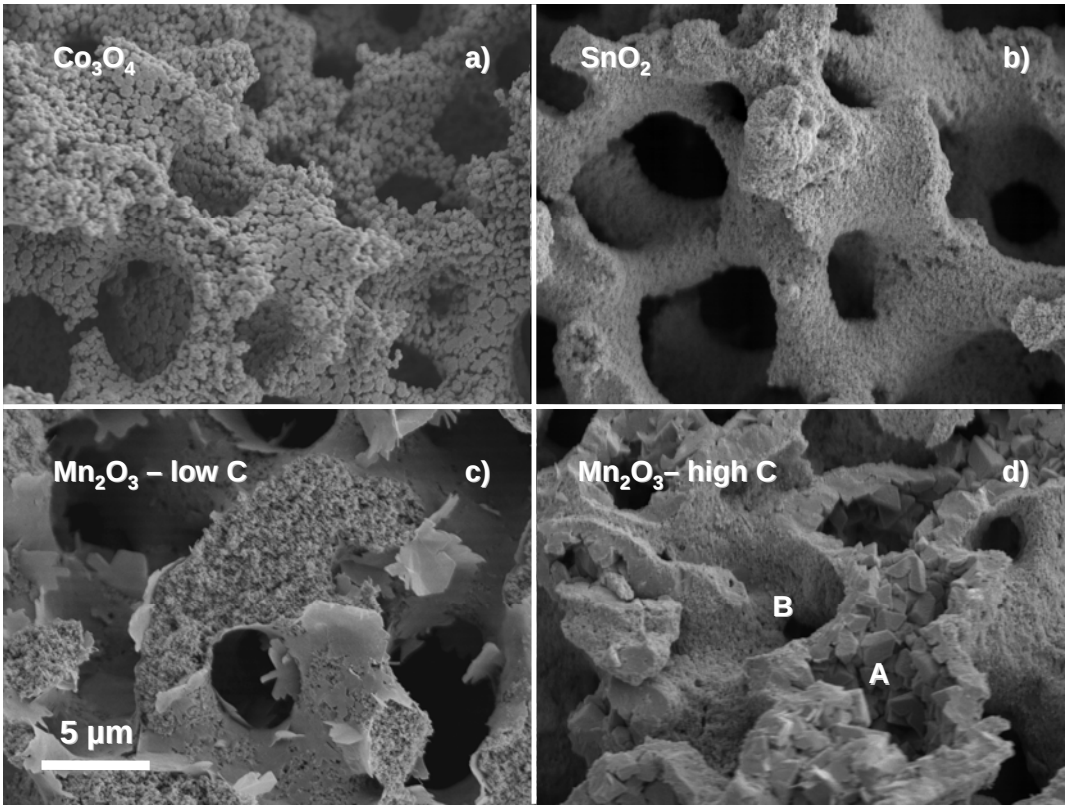

Figure 7.22. Comparison of the macropore wall structure of the different metal oxides.

7.3.4. Replication of the Mesopore Structure

Comparable trends in the change of mesopore structure as were seen for the nanocast carbon could also be observed for the metal oxide replicas (Figure 7.23). When silica monoliths with single mesopore size were used as molds, the N_2 uptake at 0.95 P/P_0 is coming down and the hysteresis slightly broadened related to the pore filling of the

respective metal oxide. The broadening of the hysteresis could be a result of partial pore blocking also seen as a decrease of the pore size in Table 7.5. However, no additional hysteresis like in the case of the carbon monoliths (Figure 7.14.) can be observed. From the nitrogen sorption *t-plots* also no increase of the microporosity could be detected. Upon removal of silica part the appearance of silica templated mesopores are obvious (most clear for the SnO_2 sample). However, depending on many factors, such as silica compatibility, nucleation and growth, etc, the silica structure is not as well replicated as in the carbon case.

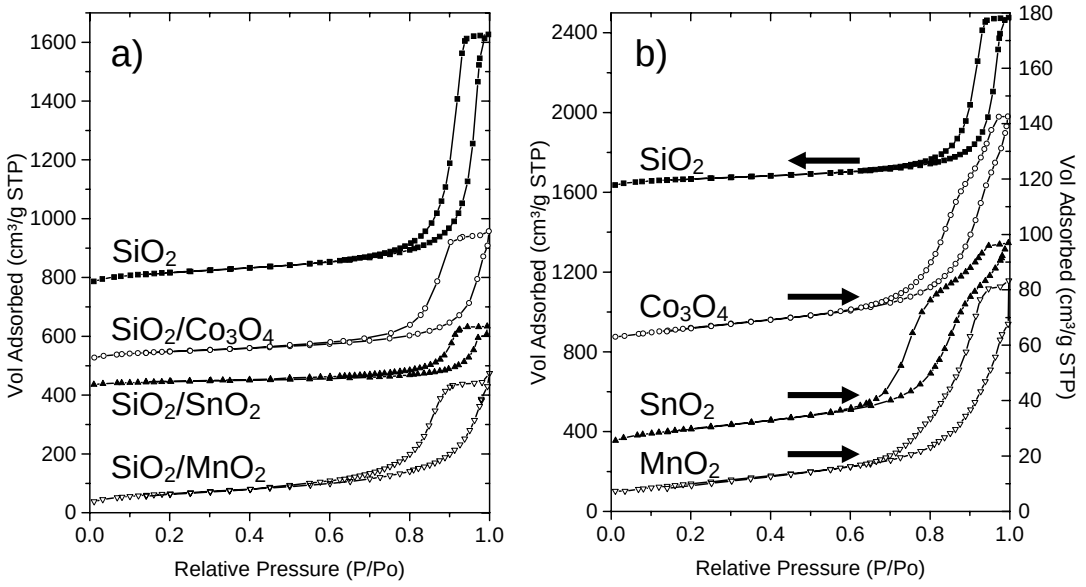

Figure 7.23. a) Nitrogen physisorption isotherms of the parent SiO_2 monolith (■, offset: 750 cm^3/g), as well as the SiO_2/Co_3O_4 composite (○, offset: 500 cm^3/g), the SiO_2/SnO_2 composite (▲, offset: 425 cm^3/g), and finally the SiO_2/MnO_2 composite (▽). Note! The composite isotherms have been corrected for the weight increase upon impregnation. b) Nitrogen physisorption isotherms of the parent SiO_2 monolith (■, left scale bar, offset: 600 cm^3/g), as well as the Co_3O_4 replica (○, right scale bar, offset: 55 cm^3/g), the SnO_2 replica (▲, right scale bar, offset: 20 cm^3/g), and the MnO_2 replica (▽, right scale bar).

Table 7.5. Nitrogen physisorption data for the silica/metal oxide composites and the metal oxide replicas.

Composite	BET Area [m^2/g]	Mesopore Volume [cm^3/g]	Mesopore Diameter [nm]	Replica	BET Area [m^2/g]	Mesopore Volume [cm^3/g]	Mesopore Diameter [nm]
SiO_2/Co_3O_4	44.8	0.137	15.1	**Co_3O_4**	40.4	0.119	12.3[c]
SiO_2/SnO_2	12.2	0.044	20.9	**SnO_2**	36.0	0.111	7.8[c]
SiO_2/MnO_2	55.2	0.142	13.5	**MnO_2**	35.9	0.098	5–30
SiO_2/Mn_2O_3	55.8	0.173	14.8	**Mn_2O_3**	29.8	0.075	10–35
CTAB-SiO_2/SnO_2	10.6	0.012	2.7/14.0	**CTAB-SnO_2**	70.4	0.108	2–100

Also when silica monoliths containing a bimodal mesopore structure were used as molds, similarities between carbon and the metal oxides could be seen. Nitrogen physisorption measurements of a SnO_2 replica revealed a broad N_2 uptake at lower relative pressures between 0.05–0.5 P/P_0 indicating a wide pore size distribution between 2 and 100 nm (results not shown). The broad distribution is not due to poor nanocasting, but a result of that the replicas consist of a rather well defined bimodal *particle* size distribution which is illustrated in Figure 7.24b. This is further evidence of that the metal oxide monoliths are negative replicas of the original silica structure on the nanometer scale. There are also other methods than TEM to determine the diameter (D) of the particles (or the *crystals*), such as calculations from the BET surface area (7.1.) or from the line broadening of the XRD peaks by using the Scherrer equation (7.2.).

$$D = 6/(A_{BET}\,\rho) \qquad (7.1.)$$

$$D = 0.9\lambda/(B\cos\theta_B) \qquad (7.2.)$$

Here, A_{BET} denotes the BET surface area, ρ the bulk density of the different oxides, λ the wave length, B the full-width at half maximum, and θ_B is the Bragg angle. The results are summarized in Table 7.6. It is clear from all methods that SnO_2 displays the smallest mean particle size, while Mn_2O_3 contains the largest. It is also obvious from TEM and XRD that sample CTAB-SnO_2 has got a bimodal particle size.

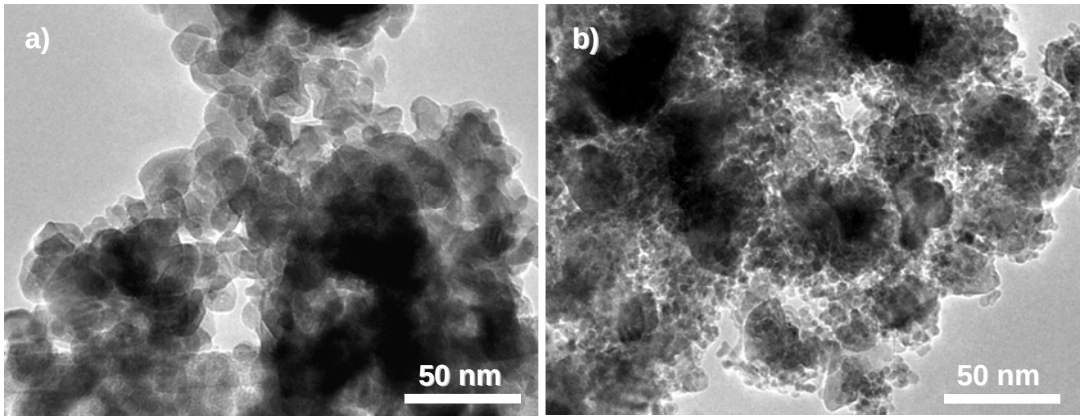

Figure 7.24. TEM images of SnO_2 replicas prepared a) from monomodal SiO_2 and b) from bimodal SiO_2.

Table 7.6. Particle (or crystal size) determined by TEM, nitrogen sorption and XRD.

	Particle Size Diameter (*D*)		
Sample	**TEM [nm]**	**N_2 [nm]**	**XRD [nm]**
Co_3O_4	10–20	24.4	20–30
SnO_2	7–15	24	15–20
MnO_2	Not Measured	33.2	Not Measured
Mn_2O_3	15–30	44.8	30–35
CTAB-SnO_2	3–7/15–35	12.3	Mean ~ 16

7.3.5. Crystallinity

When zooming in on the atomic level of the metal oxide structure, it is evident that the replicas consist of fully crystalline particles, as can be seen in the TEM image in Figure 7.18e. As already mentioned, XRD was used to determine which phases the metal oxide replicas consisted of and the diffractograms are plotted in Figure 7.25. The calcination at 550 °C resulted in the formation of the cubic Co_3O_4, the tetragonal SnO_2 (cassiterite), and the cubic Mn_2O_3 (bixbyite) crystal phases. However, if the $Mn(NO_3)_2{\cdot}4H_2O$ salt was calcined at only 300 °C, the tetragonal MnO_2 (pyrolusite) crystal structure was formed. The phases are very pure. However, there are some reflections in the manganese oxide diffractograms that we were not able to assign.

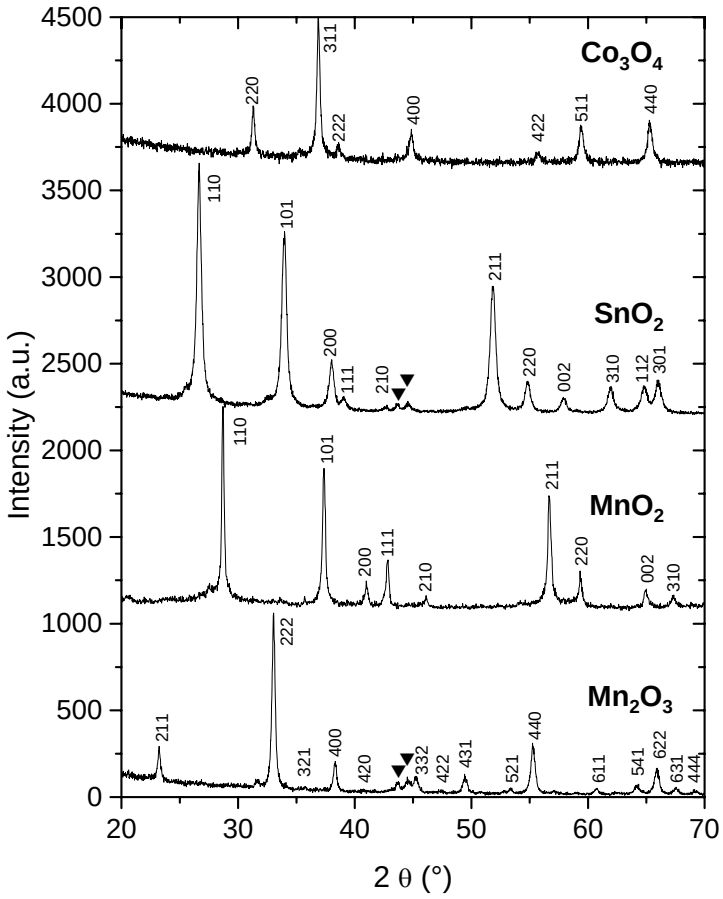

Figure 7.25. XRD indicates that the final metal oxide phases are Co_3O_4, SnO_2, MnO_2 and Mn_2O_3. ▼ indicates reflections associated to the sample holder.

8. Conclusion and Outlook

Silica monoliths containing a trimodal, hierarchical pore structure have successfully been prepared via sol-gel processing. By using PEG and CTAB as structure directing agents together with a careful control of the processing parameters it is possible to adjust the structure of the monoliths on four different length-scales simultaneously. The macroscopic size and shape can fully be controlled by adjusting the form of the synthesis vessel. Furthermore, by altering the PEG concentration in the starting silica sol the onset of the phase separation relative to the freezing of the structure by the sol-gel transition can be controlled and, thus, also the size of the macropores in the final monolithic structure. Solvent exchange post-treatments in ammonia can be applied to both strengthen the silica structure towards shrinkage or crack formation, and to control the textural mesopore size. Finally, by adding CTAB to the system it is possible to induce surfactant templated mesopores in the monoliths. By changing the hydrocarbon chain length of the surfactant it is possible to alter the size of these pores. Unfortunately, the addition of CTAB to the sol also affects the final macropore size. However, by simultaneously varying the amounts of added PEG and CTAB, it is still possible to maintain the desired macropore size. Different template removal techniques have also been studied for the silica monoliths. The conventional calcination method removes the organic templates by combustion, while chemical leaching of the templates can be carried out in sulfuric acid. The H_2SO_4 method resulted in silica monoliths having more silanol groups on the surface, which are of great importance for further surface functionalization steps.

In the second part it was shown that these silica monoliths could be used as hard templates in the preparation of carbon and non-siliceous monoliths through the nanocasting technique. Carbon replicas with up to four distinct pore size regions have been prepared. On the micrometer length-scale, the carbon monoliths are positive replicas of the starting silica monoliths. Thus, by changing the macroscopic shape and the macropore size of the silica monoliths used as hard templates, it was possible to alter the same properties of the carbon replica. Then again, on the nanometer scale, the carbon structure is a negative replica of the silica template, meaning that the mesopores in the silica monoliths become pore walls in the carbon replica and vice versa. The most straightforward way to alter the pore size is to use silica monoliths

with different mesopore structures, for instance monoliths prepared with different post-treatment conditions or with different CTAB concentrations. In addition, dilution of the carbon precursor results in interesting bimodal mesopore structures. Furthermore, depending on the silica template used it was also possible to control the amount of micropores in the carbon monoliths.

Finally, it was shown that it was possible to expand the nanocasting procedure to include non-siliceous metal oxides as well. Here, hierarchically porous monoliths of Co_3O_4, SnO_2, MnO_2, and Mn_2O_3 have successfully been prepared. The structure of these metal oxides can be controlled in a similar way as the carbon replicas. The macroscopic morphology and the macropore structure of the starting silica monoliths are accurately replicated, while the silica mesopore walls create pores in the metal oxide replicas. Unlike the carbon replica structure, the texture of the macropore walls of cobalt oxide and manganese oxide consists of large spherical aggregates. Moreover, the metal oxide monoliths are built up of small fully crystalline particles.

Future work concerning the silica monoliths includes phase separation studies with NMR and surface functionalization. On the other hand, the carbon monoliths have interesting electrical properties and could be used as superconductor materials. The tin oxide replica monoliths, which have a great chemical resistance at high pH values, will be tried out as reversed-phase HPLC columns. Furthermore, the catalytic activity will be studied on silica monoliths impregnated with metals or directly on metal oxide replicas. There are also possibilities to expand the number of chemical compositions of the monolithic replica structures depending on the requirements of a potential application area. Other metal oxides or mixtures of oxides could be prepared and also reduction of the metal oxides to pure metals could have interesting features.

9. Acknowledgements

First of all, I would like to gratefully thank Professor Jarl B. Rosenholm for letting me work at the Department of Physical Chemistry. With his cheerful manners and scientific brilliance, he has managed to create a relaxed working atmosphere in combination with a high scientific standard at the department.

Furthermore, I would like to thank my advisor, Assistant Professor Dr. Mika Lindén, to whom I will always be deeply thankful for taking me into his group and guiding me through all these years. He has always helped me find the self-confidence when I had already given up on things. Whether it is about discussing science, a few drinks at the pub or playing in a band, I have enjoyed this time very much.

I would also like to thank all the present and former colleagues at the department for creating a friendly working atmosphere. I would especially like to thank my friend Mikael "Micke" Järn for helping me through the years I've been studying in Turku. I will always be grateful for your support. I'm also appreciative to Stefan Backlund for helping me out with millions of experiments and for the fruitful discussions.

Professor Ferdi Schüth is gratefully acknowledged for welcoming me to work in his group for 14 months and the whole group at the Max-Planck-Institute für Kohlenforschung in Mülheim for making my stay extraordinary pleasant. I'm especially indebted to Dr. An-Hui Lu, Dr. Akira Taguchi, and Dr. Chia-Min Yang for letting me in on the Asian way of thinking and for sharing their ideas with me, and to Dr. Wolfgang Schmidt for valuable discussions.

I would also like to thank the co-authors, Dr. Stephan Schunk, Dr. Bodo Zibrowius, Mr. Bernd Spliethoff, and Dr. Claudia Weidenthaler, for their valuable contributions.

The financial support from the High Throughput Experimentation (HTE) Company, the Academy of Finland ("Porous Materials with Hierarchical Structures"), and the integrated EU project ("AIMs") is greatly acknowledged. GSMR is acknowledged for scientific support.

Finally, I would like to thank my family (mamma, Susanne & Conrad) and friends from outside of work for their love and support. Whether it is hard times or good times, you have always been there.

10. References

[1] Brinker, C. J.; Scherer, G.W. *Sol-Gel Science*, Academic Press, San Diego, **1990**.

[2] Kresge, C. T.; Leonowicz, M. E.; Roth, W. J.; Vartuli, J. C. *Nature* **1992**, *359*, 170.

[3] Beck, J. S.; Vartuli, J. C.; Roth, W. J.; Leonowicz, M. E.; Kresge, C. T.; Schmitt, K. D.; Chu, C. T.-W.; Olson, D. H.; Sheppard, E. W.; McCullen, S. B.; Higgins, J. B.; Schlenker, J. L. *J. Am. Chem. Soc.* **1992**, *114*, 10834.

[4] Yanagisawa, T.; Shimizu, T.; Kuroda, K.; Kato, C. *Bull. Chem. Soc. Jpn.* **1990**, *63*, 988.

[5] Web page: *http://portal.isiknowledge.com/*

[6] Breck, D. W. *Zeolite Molecular Sieves*, John Wiley and Sons, New York and London, **1974**.

[7] Dyer, A. *An Introduction to Zeolite Molecular Sieves*, John Wiley and Sons, New York and London, **1988**.

[8] Schüth, F. *Chem. Mater.* **2001**, *13*, 3184, and references therein.

[9] Ryoo, R.; Joo, S. H.; Jun, S. *J. Phys. Chem. B* **1999**, *103*, 7743.

[10] Jun, S.; Joo, S. H.; Ryoo, R.; Kruk, M.; Jaroniec, M.; Liu, Z.; Ohsuna, T.; Terasaki, O. *J. Am. Chem. Soc.* **2000**, *122*, 10712.

[11] Zhu, K.; Yue, B.; Zhou, W.; He, H. *Chem. Commun.* **2003**, *1*, 98.

[12] Yang, H.; Shi, Q.; Tian, B.; Lu, Q.; Gao, F.; Xie, S.; Fan, J.; Yu, Ch.; Tu, B.; Zhao, D. *J. Am. Chem. Soc.* **2003**, *125*, 4724.

[13] Laha, S. C.; Ryoo, R.; *Chem. Commun.* **2003**, *17*, 2138.

[14] Tian, B.; Liu, X.; Yang, H.; Xie, S.; Yu, Ch.; Tu, B.; Zhao, D. *Adv. Mater.* **2003**, *15*, 1370.

[15] Lu, A.-H.; Schmidt, W.; Taguchi, A.; Spliethoff, B.; Tesche, B.; Schüth, F. *Angew. Chem. Int. Ed. Engl.* **2002**, *41*, 3489.

[16] Kang, M.; Yi, S. H.; Lee, H. I.; Yie, J. E.; Kim, J. M. *Chem. Commun.* **2002**, 1944.

[17] Kang, M.; Kim, D.; Yi, S. H.; Han, J. U.; Yie, J. E.; Kim, J. M. *Catal. Today* **2004**, *93–95*, 695.

[18] Roggenbuck, J.; Tiemann, M. *J. Am. Chem. Soc.* **2005**, *127*, 1096.

[19] Nakamura, N.; Takahashi, R.; Sato, S.; Sodesawa, T.; Yoshida, S. *Phys. Chem. Chem. Phys.*, **2000**, *2*, 4983.

[20] Minakuchi, H.; Nakanishi, K.; Soga, N.; Ishizuka, N.; Tanaka, N. *Anal. Chem*. **1996**, *68*, 3498.

[21] Tanaka, N.; Kobayashi, H.; Nakanishi, K.; Minakuchi, H.; Ishizuka, N. *Anal. Chem.* **2001**, *73*, 420A.

[22] Fuchigami, T.; Toki, M.; Nakanishi, K. *J. Sol-Gel Sci. Tech.* **2000**, *19*, 337.

[23] Rajeshwar, K.; de Tacconi, N. R.; Chenthamarakshan, C. R. *Chem. Mater.* **2001,** *13,* 2765.

[24] Nakanishi, K. *J. Porous Mater.* **1997**, *4*, 67, and references therein.

[25] Fujita, K.; Konishi, J.; Nakanishi, K.; Hirao, K. *Appl. Phys. Lett.* **2004**, *85*, 5595.

[26] Iler, R. K. *The Chemistry of Silica*, Wiley-Interscience, New York, **1979**.

[27] Avnir, D.; Kaufman, V. R. *J. Non-Cryst. Solids* **1982**, *48*, 47.

[28] Voronkov, M. G.; Mileshkevich, V. P.; Yuzhelevski, Y. A. *The Siloxane Bond*, Consultants Bureau, New York, **1978**.

[29] Dent-Glasser, L. S.; Lachowski, E. E. *J. Chem. Soc. Dalton Trans* **1980**, *393*, 399.

[30] Assink, R. A.; Kay, B. D. *J. Non-Cryst. Solids* **1988**, *99*, 359.

[31] Vega, A. J.; Scherer, G. W. *J. Non-Cryst. Solids* **1989**, *111*, 153.

[32] Zerda, T. W.; Artaki, I.; Jonas, J. J. *J. Non-Cryst. Solids* **1986**, *81*, 365.

[33] Orcel G.; Hench, L. L.; Artaki, I.; Jonas, J.; Zerda, T. W. *J. Non-Cryst. Solids* **1988**, *105*, 223.

[34] Nakanishi, K.; Takahashi, R.; Nagakane, T.; Kitayama, K.; Koheiya, N.; Shikata, H.; Soga, N. *J. Sol-Gel Sci. Tech.* **2000**, *17*, 191.

[35] Takahashi, R.; Nakanishi, K.; Soga, N. *J. Sol-Gel Sci. Tech.* **2005**, *33*, 159.

[36] Sing, K. S. W.; Everett, D. H.; Haul, R. A. W.; Moscou, L.; Pierotti, R. A.; Rouquerol, J.; Siemieniewska, T. *Pure Appl. Chem.* **1985**, *57*, 603.

[37] Behrens, P. *Adv. Mater.* **1993**, *5*, 127.

[38] Gates, B.; Yin, Y.; Xia, Y. *Chem. Mater.* **1999**, *11*, 2827.

[39] Kaji, H.; Nakanishi, K.; Soga, N. *J. Non-Cryst. Solids* **1995**, *185*, 18.

[40] Nakanishi, K.; Soga, N. *J. Am. Chem. Soc.* **1991**, *74*, 2518.

[41] Nakanishi, K.; Soga, N. *J. Non-Cryst. Solids* **1992**, *139*, 1.

[42] Nakanishi, K.; Komura, H.; Takahashi, R.; Soga, N. *Bull. Chem. Soc. Jpn.* **1994**, *67*, 1327.

[43] Sato, Y.; Nakanishi, K.; Hirao, K.; Jinnai, H.; Shibayama, M.; Melnichenko, Y. B.; Wignall, G. D. *Colloids Surfaces A* **2001**, *187*, 117.

[44] Nakanishi K, Sato Y, Ruyat Y, Hirao K *J. Sol-Gel Sci. Tech.* **2003**, *26*, 567.

[45] Asnaghi, D.; Giglio, M.; Bossi, A.; Righetti, P. G. *J. Chem. Phys.* 1995, *102*, 9736.

[46] Fujita, K.; Konishi, J.; Nakanishi, K.; Hirao, K. *Appl. Phys. Lett.* **2004**, *85*, 5595.

[47] Konishi, J.; Fujita, K.; Nakanishi, K.; Hirao, K. *Chem. Mater.* **2006,** *18,* 864.

[48] Backlund, S.; Smått, J.-H.; Rosenholm, J. B.; Lindén, M. *J. Dispersion Sci. Technol.* In press.

[49] Kumon, S.; Nakanishi, K.; Hirao, K.; *J. Sol-Gel Sci. Tech.* **2000**, *19*, 553.

[50] Kajihara, K.; Nakanishi. K.; Tanaka, K.; Hirao, K.; Soga, N. *J. Am. Chem. Soc.* **1998**, *81*, 2670.

[51] *IUPAC Compendium of Chemical Terminology* **1994**, *66*, 591, (2nd Edition (1997)).

[52] Flory, P. J. *J. Chem. Phys.* **1942**, *10*, 51.

[53] Huggins, M. *J. Phys. Chem.* **1942**, *46*, 151.

[54] Huggins, M. *Am. Chem. Soc.* **1942**, *64*, 1712.

[55] Brinker, C. J.; Scherer G. W.; Editors: Hench, L. L.; Ulrich, D. R., *Ultrastructure Processing of Ceramics, Glasses, and Composites*, Wiley, New York, **1984**, pp. 43–59.

[56] M. Lindén, S. Schacht, F. Schüth, A. Steel, and K. K. Unger, *J. Porous Materials* **1998**, *5*, 177.

[57] Vartuli, J. C.; Schmitt, K. D.; Kresge, C. T.; Roth, W. J.; Leonowicz, M. E.; McCullen, S. B.; Hellring, S. D.; Beck, J. S.; Schlenker, J. L.; Olson, D. H.; Sheppardt E. W. *Chem. Mater.* **1994**, *6*, 2317.

[58] Raman, N. K.; Anderson, M. T.; Brinker, C. J. *Chem. Mater.* **1996**, *8*, 1682.

[59] Martin, T.; Galarneau, A.; Di Renzo, F; Fajula, F.; Plee, D. *Angew. Chem. Int. Ed.* **2002**, *41*, 2590.

[60] Petitto, C.; Galarneau, A.; Driole, M.-F., Chiche, B.; Alonso, B.; Di Renzo, F.; Fajula, F. *Chem. Mater.* **2005**, *17*, 2120.

[61] Ryoo, R.; Kim, J. M. *Chem. Commun.* **1996**, 561.

[62] Huo, Q.; Margolese, D. I.; Ciesla, U.; Demuth, D.; Feng, P.; Gier, T. E.; Sierger, P.; Firouzi, A.; Chmelka, B. F.; Schüth, F.; Stucky, G. D. *Chem. Mater.* **1994**, *6*, 1176.

[63] Huo, Q. S.; Margolese, D. I.; Stucky, G. D. *Chem. Mater.* **1996**, *8*,1147.

[64] DiRenzo, F.; Galarneau, A.; Desplantier-Giscard, D.; Mastrantuono, L.; Testa, F.; Fajula, F. *Chim. Ind.* **1999**, *81*, 587.

[65] Lefevre, B.; Galarneau, A.; Iapichella, J.; Petitto, C.; Di Renzo, F.; Fajula, F. *Chem. Mater.* **2005**, *17*, 601.

[66] Huo, Q.; Margolese, D. I.; Ciesla, U.; Feng, P.; Gier, T. E.; Sieger, P.; Leon, R.; Petroff, P. M.; Schüth, F.; Stucky, G. D. *Nature* **1994**, *368*, 317.

[67] Zhao, D.; Feng, J.; Huo, Q.; Melosh, N.; Fredrickson, G. H.; Chmelka,B. F.; Stucky, G. D. *Science* 1998, *279*, 548.

[68] Zhao, D.; Huo, Q.; Feng, J.; Chmelka, B. F.; Stucky, G. D. *J. Am. Chem. Soc.* 1998, *120,* 6024.

[69] Lang, N.; Tuel, A. *Chem. Mater.* **2004,** *16*, 1961.

[70] Tian, B.; Liu, X.; Yu, C.; Gao, F.; Luo, Q.; Xie, S.; Tu, B.; Zhao, D. *Chem. Commun.* **2002**, 1186.

[71] Kawi, S.; Lai, M. W. *Chem. Commun*. **1998**, 1047.

[72] Keene, M. T. J.; Denoyel, R.; Llewellyn, P. L. *Chem. Commun*. **1998**, 2203.

[73] Tanev, P. T.; Pinnavaia, T. J. *Chem. Mater.* **1996**, *8*, 2068.

[74] Hitz, S.; Prins, R. *J. Catal*. **1997**, *168*, 194.

[75] Yang, C. M.; Zibrowius, B.; Schmidt, W.; Schüth, F. *Chem.Mater.* **2003**, *15*, 3739.

[76] Yang, C. M.; Zibrowius, B.; Schmidt, W.; Schüth, F. *Chem. Mater.* **2004,** *16*, 2918.

[77] Polarz, S.; Antonietti, M. *Chem.Commun.* **2002**, 2593.

[78] Lu, A.-H.; Schüth, F. *C. R. Chimie* **2005**, *8*, 609.

[79] Kruk, M.; Jaroniec, M.; Ryoo R.; Joo, S. H. *J. Phys. Chem. B* **2000**, *104*, 7960.

[80] Joo, S. H.; Jun S.; Ryoo, R. *Microporous Mesoporous Mater.* **2001**, *44–45*, 153.

[81] Joo, S. H.; Ryoo, R.; Kruk, M.; Jaroniec, M.; *J. Phys. Chem. B* **2002**, *106,* 4640.

[82] Joo, S. H.; Choi, S. J.; Oh, I.; Kwak, J.; Liu, Z.; Terasaki, O.; Ryoo, R. *Nature* **2001**, *412*, 169.

[83] Che, S.; Lund, K.; Tatsumi, T.; Iijima, S.; Joo, S. H.; Ryoo, R.; Terasaki O. *Angew. Chem. Int. Ed.* **2003**, *42*, 2182.

[84] Callister, W.D. *Materials science and engineering : an introduction (6th edition)*, John Wiley, New York, **2003**.

[85] Choura, M.; Belgachem, N. M.; Gandini, A. *Macromolecules*, **1996**, *29*, 3839.

[86] Dunlop, A.P.; Peters, F.N. *The Furans*, Reinhold Publishing Co., New York, **1953**.

[87] Lebeau, B.; Parmentier, J.; Soulard, M.; Fowler, C.; Zana, R.; Vix-Guterl, C.; Patarin, J. *C. R. Chimie* **2005**, *8*, 597.

[88] Li, G.; Lu, Z.; Huang, B.; Wang, Z.; Huang, H.; Xue, R.; Chen, L. *Solid State Ionics* **1996**, *89*, 327.

[89] Kim, T. W.; Park, I. S.; Ryoo R. *Angew. Chem. Int. Ed.* **2003**, *42*, 4375.

[90] Kishore, N.; Sachan, S.; Rai, K. N.; Kumar, A. *Carbon* **2003**, *41*, 2961.

[91] Lee, J.; Yoon, S. Hyeon, T.; Oh, S. M.; Kim, K. B. *Chem. Commun.* **1999**, 2177.

[92] Vix-Guterl, C.; Saadallah, S.; Frackowiak, E.; Jurewicz, K.; Reda, M.; Parmentier, J.; Patarin, J.; Béguin, F. *Mater. Sci. Eng. B* **2004**, *108*, 148.

[93] Jurewicz, K.; Vix-Guterl, C.; Frackowiak, E.; Saadallah, S.; Reda, M.; Parmentier, J.; Patarin, J.; Béguin, F. *J. Phys. Chem. Solids* **2004**, *65*, 287.

[94] Dillon, A. C.; Jones, K. M.; Bekkedahl, T. A.; Kiang, C. H.; Bethune, D. S.; Heben, M. J. *Nature* **1997**, *386*, 377.

[95] Gadiou, R.; Saadallah, S.; Piquerot, T.; David, P.; Parmentier, J.; Vix-Guterl, C. *Microporous Mesoporous Mater.* **2005**, *79*, 121.

[96] Schwickardi, M.; Johann, T.; Schmidt, W.; Schüth, F. *Chem. Mater.* **2002**, *14*, 3913.

[97] Schwickardi, M.; Johann, T.; Schmidt, Busch, O.; W.; Schüth, F. *Stud. Surf. Sci. Catal.* **2002**, *143*, 93.

[98] Stein, A. *Microporous Mesoporous Mater.* **2001**, *44–45*, 227, and references therein.

[99] Shi, Z. G.; Feng, Y. Q.; Xu, L.; Zhang, M.; Da, S. L. *Talanta* **2004**, *63*, 593.

[100] Ishizuka, N.; Minakuchi, H.; Nakanishi, K.; Soga, N.; Tanaka, N. *J. Chromatography A*, **1998**, *797*, 133.

[101] Flegler, S. L.; Heckman, J. W.; Klomparens, K. L.; Scanning and Transmission Electron Microscopy, Oxford University Press, NewYork, **1993**.

[102] Rouquerol, J.; Avnir, D.; Fairbridge, C. W.; Everett, D. H.; Haynes, J. H.; Pernicone, N.; Ramsay, J. D. F.; Sing, K. S. W.; Unger, K. K. *Pure Appl. Chem.* **1994**, *66*, 1739.

[103] Sing, K. S. W.; Everett, D. H.; Haul, R. A. W.; Moscou, L.; Pierotti, R. A.; Rouquerol, J.; Siemieniewska, T. *Pure Appl. Chem.* **1985**, *57*, 603.

[104] Rouquerol, F.; Rouquerol, J.; Sing, K. *Adsorption by Powders and Porous Solids – Principles, Methodology and Applications*, Academic Press, San Diego, **1999**.

[105] Barrett, E. P.; Joyner, L. G.; Halenda, P. H. *J. Am. Chem. Soc.* **1951**, *73*, 373.

[106] Neimark, A.V.; Ravikovitch, P.I. *Microporous Mesoporous Mater.* **2001**, *44–45*, 697.

[107] Ravikovitch, P. I.; Wei, D.; Chung, W. T.; Haller, G. L.; Neimark, A. V. *J. Phys. Chem. B*, **1997**, *101*, 3671.

[108] León y León, C. A. *Adv. Colloid Interface Sci.* **1998**, *76–77*, 341.

[109] Webb, P. A.; *An Introduction to the Physical Characterization of Materials by Mercury Intrusion Porosimetry with Emphasis on Reduction and Presentation of Experimental Data*, Micromeritics Instrument Corp., Norcross, GA, **2001**.

[110] Fuerstenau, D.W. *J. Phys. Chem*, **1956**, *60*, 981.

[111] Shi, Z. G.; Feng, Y. Q.; Xu, L.; Da, S. L.; Ren, Y. Y. *Microporous Mesoporous Mater.* **2004**, *68*, 55.

[112] Amatani, T.; Nakanishi, K.; Hirao, K.; Kodaira, T. *Chem. Mater.* **2005**, *17*, 2114.

[113] Brandhuber, D.; Torma, V.; Raab, C.; Peterlik, H.; Kulak, A.; Hüsing, N. *Chem. Mater.* **2005**, *17*, 4262.

[114] Shi, Z. G.; Feng, Y. Q.; Xu, L. Da, S. L.; Zhang, M. *Carbon* **2003**, *41*, 2677.

[115] Khalili, N. R.; Pan, M.; Sandi, G. *Carbon* **2000**, *38*, 573.